Development of a-SiGe:H

from material characterization to multi-junction device

S.J. Roerink

Photovoltaic Materials and Devices Group,
ESE, EEMCS, TU Delft

Development of a-SiGe:H

from material characterization to multi-junction device

by

S.J. Roerink

to obtain the degree of Master of Science
at the Delft University of Technology,
to be defended publicly on Friday September 27, 2019 at 10:00 AM.

Student number:	4314751	
Project duration:	January 1, 2019 – September 27, 2019	
Msc Thesis Committee:	Prof. dr. ir. A.H.M. Smets	TU Delft, ESE - PVMD, Supervisor
	Dr. R.A.C.M.M. van Swaaij	TU Delft, ESE - PVMD, Associate Professor
	Dr. ir. M. Popov	TU Delft, ESE - IEPG, Associate Professor
	Ir. T. de Vrijer	TU Delft, ESE - PVMD, Daily supervisor

This thesis is confidential and cannot be made public until September 27, 2019.

Preface

This master thesis marks the end of my times as a student by finishing the studies in Sustainable Energy Technology (SET) at Delft University of Technology. When I started 6 years ago I never expected the current path, that I would graduate at the faculty of EWI. I started at the TBM faculty and my experiences in African countries did realise me to study Sustainable Energy Technology. I have not chosen the easy way, but I'm glad with the path I did chose. I am proud and happy with the way it went. I have learnt so much the past year about solar energy, research and many more things.

My sincere great- and thank fullness go to my daily supervisor Thierry de Vrijer. I could not have completed this thesis without the help of you. Therefore, I would like to thank you for your excellent supervision. You helped me with experiments, guided me when it was necessary and you were always available for a quick question. Moreover, you were always available for my late Whatsapp messages and problems with AMIGO and helped me with your excellent knowledge. Additionally, you went through my thesis with full commitment and precision. Thanks for the interesting discussions we had, sometimes in the office or lab. Furthermore, I would like to thank professor Arno Smets for his passion and enthusiasm that he expressed during my project. The meetings we had once every two weeks in the last months of the thesis helped me further improve the work. I also wanna thank all the staff from the PVMD group for helping me out when needed, you are all doing great things! Thanks for giving me small spaces and slots on AMIGO when I kept on stalking you on Whatsapp. Finally, I wanna thank Dr. van Swaaij and Dr.ir. Popov for their willingness to be part of my graduation committee.

Someone who I should mention is my friend Ashish Binani. We both started our thesis under supervision of Thierry. We went together to the lab in the weekends and you were always my right hand if I needed help to put some samples in AMIGO at hard and late moments. Without you my thesis would have been way harder. Moreover, I wanna thank you for the discussions we had, the experiences we shared, the food we had and for checking some of my paragraphs of the thesis. I can truly say that this thesis brought me a friend.

My gratitude also goes to the process engineers and technicians, Stefaan Heirman and Martijn Thijssen, who helped me to use the equipment and were always available if assistance was needed. Sorry for all the late night and weekend Whatsapp messages.

I can't and should not forget to my roommates Lucas and Kees. The last year many moments I have been away and busy with the thesis. We had many evenings when I came home and the food was ready. Moreover, thanks for being a listening ear and always supporting me through the long process. You made the process easier and funnier. Additionally, I wanna thank all my friends for being patient and interested in my progress (especially Jordi and Martijn). You are a true group of great friends. I also wanna thank my old house, the Raamstraat 47, this is the place which made me to the person I am now.

Last but not least I want to thank my family. Without their continuous love and support, I would not have reached this point. You have always supported me during my studies and life and I can't express in words how much that means for me. You were always the listening ears when I had troubles, but also the first ones to celebrate success. I am proud to say that I could not wish any better than I currently have.

Steven Roerink
Delft, August 2019

Abstract

Multi-junction solar cells with Si alloys have true potential for high conversion efficiency, because of the spectrum splitting capability. For optimal spectral utilization, a multi-junction silicon based device needs a silicon alloy with a bandgap between that of nc-Si (1.1 eV) and a-Si (1.8 eV). a-SiGe:H has a tunable bandgap between 1.4-1.6 eV by varying the GeH_4 flow rate in the layer.

An investigation of deposition parameters on PECVD processed a-SiGe:H films showed that variation of the GeH_4/SiH_4 flow rate is the most influential deposition parameter to achieve bandgap tuning. It influences the optical-, electrical- and material properties due to the fact that it directly changes the GeH_4 flow rate in the material.

Subsequently, a n-i-p substrate single junction a-SiGe:H solar cell is fabricated. This is the reversed p-i-n superstrate a-SiGe:H solar cell, fabricated by the PVMD group. It has a V_{oc} of 508 mV, a FF of 0.39, a J_{sc} of 9.9 mA/cm^2 and a final efficiency of 2.9%. Due to the low performance, manipulation techniques were introduced. The different proposed shapes consist of bandgap grading in the absorber through GeH_4 flow rate profiling. A study on buffer type and thickness, different profiling schemes, grading widths and total absorber thickness strongly improved the device performance.

The overall champion single junction a-SiGe:H solar cell has a 3.2 nm n/i i-a-Si buffer combined with a 5 nm n/i i-a-SiGe:H buffer, a V-shape GeH_4 peak flow rate of 2.4 sccm, a 134 nm n/i grading width, a 36 nm i/p grading width and a total absorber thickness of 170 nm. This cell generates a V_{oc} of 735 mV, a FF of 0.64, a J_{sc} of 13.23 mA/cm^2 and a final efficiency of 6.18%. This is a relative increase of 113.8% in efficiency.

The single junction solar cell fabrication is followed by demonstration of a two-junction device. The overall champion tandem solar cell consists of a 200 nm a-Si:H top cell and a 170 nm a-SiGe:H bottom cell with a V-shape GeH_4 peak flow rate of 5.3 sccm. This champion tandem solar cell generates a V_{oc} of 1395 mV, a FF of 0.69, a current limiting J_{sc} of 8.34 mA/cm^2 and a final efficiency of 7.99%. Finally, research proved that the change in top- and bottom cell thickness, the maximum GeH_4 flow rate and the U- and V-shape profiles are interesting manipulation techniques in a multi-junction device due to their flexibility to increase the current limiting J_{sc} and improve current matching.

Contents

List of Symbols

Abbreviations

:H	Hydrogenated
Asahi	Asahi-VU glass substrate
a-Si	Amorphous Silicon
a-SiGe	Amorphous Silicon Germanium
AM	Air Mass
AZO	Aluminium Zinc Oxide
c-Si	Crystalline Silicon
Corning glass	Corning Eagle XG glass
DOS	Density of States
EQE	External Quantum Efficiency
ITO	Indium Tin Oxide
LID	Light Induced Degradation
MPP	Maximum Power Point
nc-Si	Nanocrystalline Silicon
PECVD	Plasma Enhanced Chemical Vapour Deposition
PV	Photovoltaics
RF	Radio Frequency
SDS	Sustainable Development Scenario
SE	Spectroscopic Ellipsometry
SiOx	Silicon Oxide
SQL	Shockley Queisser Limit
STC	Standard Test Conditions
SWE	Staebler–Wronski Effect
TCO	Transparent Conductive Oxide
TF	Thin Films
TFSSC	Thin Film Silicon Solar Cells

Constants

c	Speed of light in Vacuum	$2.9979 \text{ x } 10^{-8}$	$m\ s^{-1}$
h	Planck’s constant	$6.6261 \text{ x } 10^{-34}$	$m^2\ kg\ s^{-1}$
k_B	Boltzmann constant	1.3806×10^{-23}	$m^2\ kg\ s^{-2}\ K^{-1}$
q	Elementary charge	1.6022×10^{-19}	C

Variables

A	Absorptance
A_{cell}	Cell area
d	Thickness of the layer
d_{gap}	Gap between contacts
E_{act}	Activation Energy
E_G	Bandgap Energy
E_{ph}	Photon Energy
E_{TAUC}	Tauc Bandgap
E_{opt}	Optical Energy bandgap
E_{04}	E04 Bandgap
FF	Fill Factor
I_{MPP}	Maximum Power Point Current
$I_{abs}(\lambda, d)$	Light Intensity inside the medium
$I_0(\lambda, d)$	Initial intensity at the surface
I_{sc}	Short Circuit Current
J_{sc}	Short Circuit Current Density
J_0	Saturation Current Density
l	Contact Length
n_{ideal}	Ideality Factor
n	Free electron concentration
p	Free hole concentration
P_{MPP}	Maximum Peak Power
R	Reflectance
R_s	Series Resistance
R_{sh}	Shunt Resistance
r	Nature of the transition
R_{TEMP}	Temperature-dependent Resistance
T	Transmittance
V_{MPP}	Maximum Power Point Voltage
V_{oc}	Open Circuit Voltage
X_C	Crystalline Fraction
$I_{a\text{-}Si}$	Amorphous Peak Area
$I_{c\text{-}Si}$	Crystalline Peak Area

$\alpha(\lambda)$	Absorption Coefficient
$\tilde{e}(\lambda)$	Complex electric permittivity
$\tilde{n}(\lambda)$	Complex refractive index
$\kappa(\lambda)$	Extinction coefficient
γ	Correction Factor
λ	Wavelength
Θ_{crit}	Critical Angle
Θ_i	Angle of incidence of light
Θ_t	Angle of refracted light
σ_{dark}	Dark Conductivity
σ_0	Pre-exponential factor

Units

Mtoe	Millions of tonnes of oil equivalent = 11.63 TWh
sccm	Standard cubic centimeters per minute
TWh	Terawatt Hour
W_P	Watt Peak

List of Figures

List of Tables

1

Introduction

In this chapter a theoretical background of solar cells working principles, history and motivation of this thesis is provided, leading up to the research questions.

1.1. Background

Electricity is not a common good for everyone in the world. Around 1 billion people still do not have access to electricity. These people mostly live in rural places of developing countries in Africa and Asia. Therefore, sufficient supply of energy is a challenge, which should be tackled.

In the last century we have seen a rapid increase in the total energy consumption, which is expected to keep rising over the coming years. The International Energy Agency mentioned that the global electricity demand rose by 4% in 2018, by 900 TWh, which is nearly twice as fast as the overall energy demand growth [1]. This phenomena is related to electrification and growth of world population. These factors are expected to continue to rise. Therefore, electricity generation and supply should be improved to meet those requirements and trends, indicated by Figure 1.1.

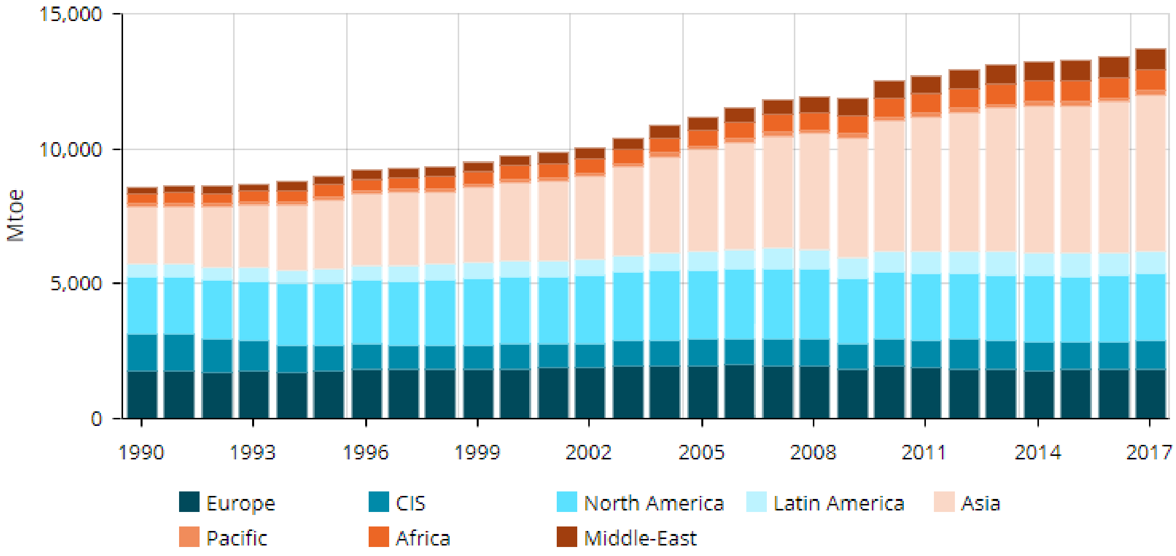

Figure 1.1: The total worldwide energy consumption from 1990 to 2017 [1].

Figure 1.1 displays that the total energy consumption has significantly increased over the past 20 years and will increase even further if this trend continues.

However, the crux of the current energy generation mix is that fossil based energy generation like coal and gas power plants, cover a significant amount of the total energy consumption. These sources generate a stable baseload of electricity for countries, but the combustion of fossil fuels pollute the environment. This has established a raise in CO_2 concentration in the air which is one of the causes of global warming.

The influence of humankind is the number one cause of global warming, especially the carbon pollution we cause by burning fossil fuels and the pollution-capturing we prevent by destroying forests. The so-called released greenhouse gasses contribute to pollution, which alters the earth's climate system, causing droughts, storms, floods etc, affecting humans. Moreover, fossil fuels are a finite resource, resulting in volatile energy prices and political conflicts over their control. For these reasons, an alternative to cover the world energy demand without using fossil fuels should be developed [13].

A shift towards an energy society based on renewable sources, rather than fossil fuels is required. A decarbonized energy system, increasingly fueled by renewable sources, is vital to the threat of climate change. Although we have seen an absolute growth in capacity of renewable energy generating sources, the International Renewable Energy Agency concluded that: if we want to meet our climate goals, renewable deployment must accelerate six times faster than today [14].

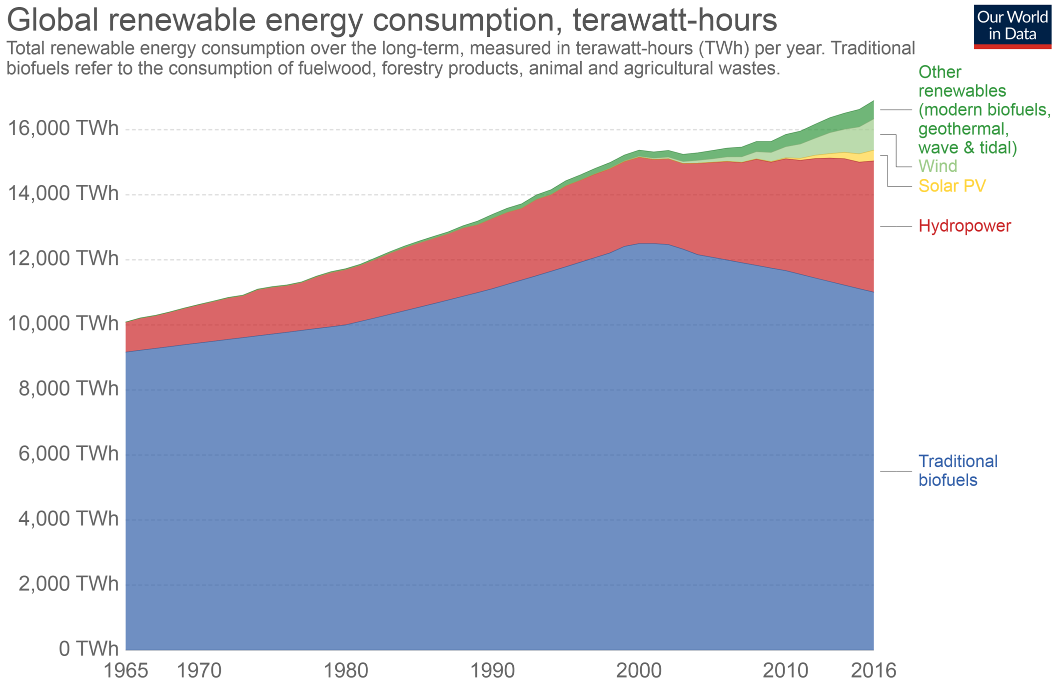

Figure 1.2: The total energy consumption of renewable energy sources over the past 50 years [2].

As can be seen, Figure 1.2 displays that the electricity generated by renewable energy sources is still low compared to the total energy consumption, Figure 1.1. Electricity generation from renewable energy sources is required to meet the requirements of the Paris agreement. The Paris agreement gained more attention around renewable energy sources, including wind, solar, biomass, hydro and geothermal power. This agreement was signed in order to combat climate change and to accelerate and intensify the actions and investments needed for a sustainable low carbon future. The Paris Agreement's central aim is: to strengthen the global response to the threat of climate change by keeping a global temperature rise this century well below 2°C above pre-industrial levels and to pursue efforts to limit the temperature increase even further to 1.5°C by low greenhouse gas emissions and climate-resilient development [15].

A varied portfolio of renewable energy sources is the key to a stable electricity grid. Especially solar power still has a low share of the total electricity generation, while it has a great development potential, due to the fact that the Sun is the largest free and most abundant potential renewable energy source on this planet. Solar energy can be converted into electricity using a thermodynamic or electronic conversion method [4]. These methods and all concepts behind solar energy will be explained in the coming paragraphs.

1.2. Solar energy

Solar photovoltaic power (PV) led the expansion in renewable power generation in 2017, as deployment boomed in China and prices continued to fall. Since 2010, prices have fallen by 70% for new solar PV large utility-scale systems. Moreover, an increase in efficiency of solar panels and the urgency for renewable energy sources have accelerated the growth in solar energy contribution to the total installed electricity generation capacity. Those developments, encouraged by ambitious climate policies in the European Union, the United States, China, India, Japan and Australia, enable developing countries to expand their renewable capacities [1].

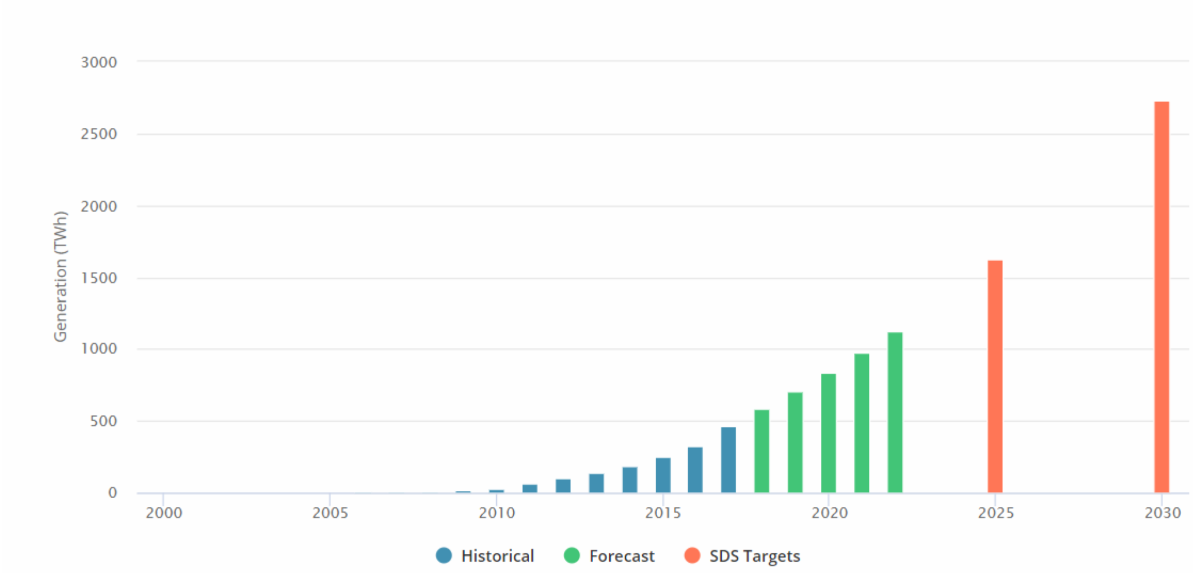

Figure 1.3: The historical development of solar PV power generation and its future SDS target [1].

Power generation from solar PV is estimated to have grown by over a third in 2017, up to 460 TWh, representing almost 2% of total world electricity generation as can be seen in Figure 1.3. Solar PV is well on track to reach the levels envisioned in the Sustainable Development Scenario (SDS) target, which will require annual capacity additions of 17% between 2019 and 2030 [1].

This thesis concerns photovoltaic (PV) technology, where the radiation of the sun is converted directly into electrical energy. The working principle of a solar cell is based on the photovoltaic effect, i.e. the generation of a potential difference at the junction of two different materials in response to electromagnetic radiation [4]. Before diving into the PV effect, the concept of radiation will be shortly discussed.

1.2.1. Concept of radiation

All objects with a temperature above the absolute zero, equal to 0°K or -273°C, emit electromagnetic radiation. The sun, 5778°K, emits solar radiation, which can be described as a wave or a particle. Light consists of energy quanta, which are called photons. Photons are generally expressed in units of energy, while waves are described by the wavelength. The energy of photons (E_{ph}), which defines the energy of the wave can be described by equation 1.1.

$$E_{\mathrm{ph}} = h \cdot v = \frac{h \cdot c}{\lambda} \tag{1.1}$$

where v is the frequency of light, c is the speed of light, h is the Planck's constant, and λ is the wavelength. The light spectrum consists of different wavelengths, given by both visible and invisible light. Solar radiation comes from both the visible and invisible light wavelength range. In more detail, roughly 9% the of the solar radiation comes from the ultraviolet region (150 nm - 400 nm), 40% of the solar radiation from the visible spectrum (400 nm - 700 nm) and lastly approximately 51% from the infrared region (700 nm - 1000 µm) [16]. Formula 1.1 indicates that the longer the wavelength λ the smaller the corresponding photon energy is. Figure 1.4 displays the total spectrum, whereas for PV application people are mostly interested in the spectrum from ultraviolet to infrared.

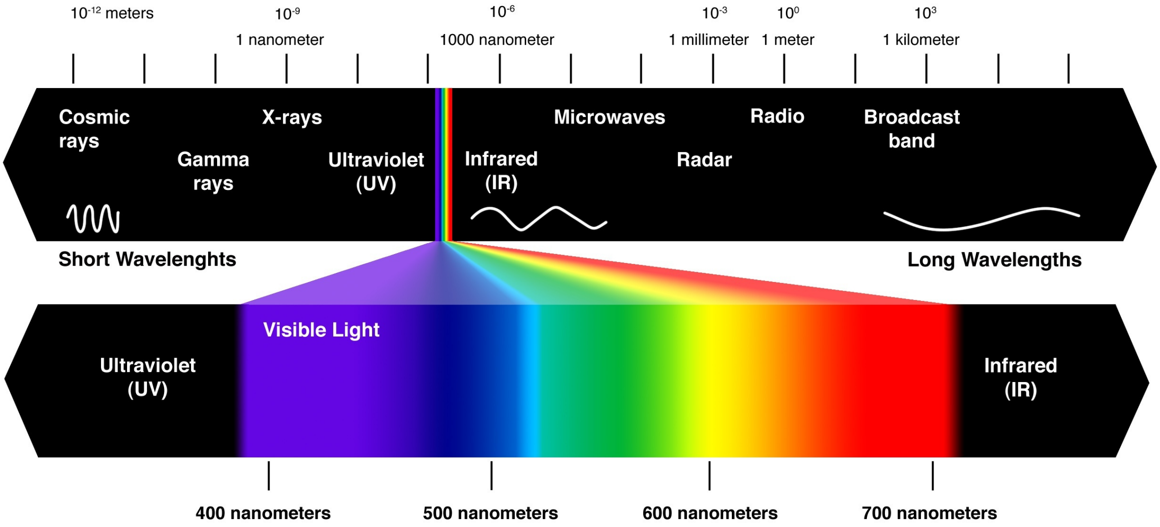

Figure 1.4: An overview of the total spectrum of light ranging from ultraviolet to infrared [3].

To compare the PV performance per location and time a standard reference spectrum is defined. The spectrum is defined based on Air Mass (=AM). AM determines how far light has to travel through the Earth's atmosphere compared to its shortest path [5]. The air mass coefficient is used to characterize the solar spectrum after solar radiation has traveled through the atmosphere. The AM0 spectrum is therefore defined as the spectrum in the space and has a total radiation of 1366 W/m^2, broadly known as the solar constant. However, it is important to mention that in this thesis the focus will be on the AM1.5 spectrum, which represents the irradiance when the beam of light, which reaches atmosphere is in between 45-50°, exactly 48.2°. The AM1.5 spectrum means that the beam passes through 1.5 times the mass of air, before the surface of Earth is reached, compared to light under normal incidence. By integrating the irradiance over the whole solar spectrum, the corresponding radiation equals 1000 W/m^2 [10].

1.2.2. Photovoltaic effect

PV technology uses the radiation from the sun to generate electrical energy. The electrical energy, which is a flow of charge carrying particles, is generated using the PV effect. The PV effect consists of three basic processes, namely (i) generation of charge carriers due to the absorption of photons in the materials that form a junction, followed by (ii) separation of the photo-generated charge carriers in the junction and (iii) collection of the photo-generated charge carriers at the terminals of the junction. These processes will be explained more in detail in the coming paragraph.

Generation of charge carriers due to the absorption of photons

Absorption of a photon in a material means that its energy is used to excite an electron from an initial energy level to a higher energy level. These energy levels are the so-called valence and conduction band, whereas the energy difference, called the bandgap E_G is defined as $E_G = E_C - E_V$, which equals the photon energy, given by equation 1.1.

A photon is only absorbed if the photon energy is equal or greater than the bandgap energy. In that case the energy is used to excite an electron from the valence to the conduction band. Therefore, the bandgap is the difference between the top of the valence band and the bottom of the conduction band, as displayed in Figure 1.5. Generation of an electron-hole pair occurs when a photon is absorbed, which means that the photon transfers its energy to an electron in the valence band. The electron is thereby excited to the conduction band, leaving a void with a positive charge behind in the valence band, called a hole. Electrons are negatively charged, so while exciting the negative charged particle, the positive hole remains behind.

Electrons in the valence band E_V are bound to an atom, while electrons in the conduction band E_C are free to move through the material (free charge carrier). This means that electrons in the conduction band are able to conduct electric current. However, in single crystal and pure crystalline materials between the conduction and valence bond no energy states exist, which could be populated by electrons. Therefore, the bandgap can be seen as forbidden energy state for electrons.

Besides the fact that E_{ph} can be equal to E_G, another possibility is that E_{ph} is bigger than E_G. In this case the energy difference between the photon energy and the bandgap energy is emitted as heat, also seen as thermalization loss, when the electron and hole relax to the bottom and top of their allowed energy states [13]. Finally, if a photon with an energy smaller than E_G reaches an ideal semiconductor, it will not be absorbed but will traverse the material without interaction and therefore no mobile charge carriers are generated. All those different options are displayed in Figure 1.5.

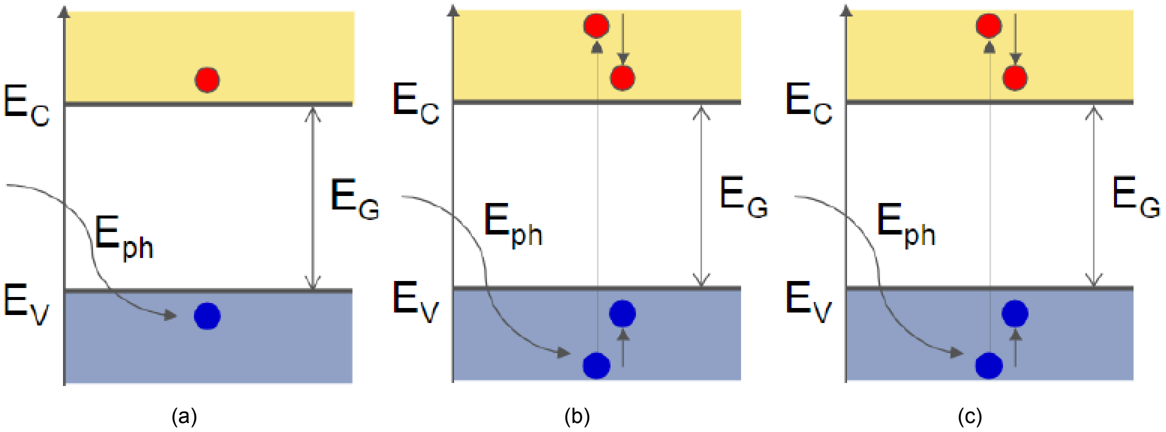

Figure 1.5: Generation of charge carriers with the following conditions: $E_{ph}=E_G$ **(a)**, $E_{ph}>E_G$ **(b)** and lastly $E_{ph}<E_G$ **(c)** [4].

All above described processes appeal to direct bandgap material, which means that the maximum of the valence band and the minimum of the conduction band occur at the same k-vector. Therefore, an electron can be excited from the valence to the conduction band without a change in the momentum. However, if the electron cannot be excited without changing this momentum, which means valence and conduction bands are not flat, it is called an indirect bandgap material. The electron can only change its momentum by momentum exchange with the crystal, i.e. by receiving momentum from or giving momentum to vibrations of the crystal lattice [4]. So, extra momentum is needed to excite an electron from valence to conduction band and therefore the absorption coefficient is lower compared to direct bandgap materials.

Separation of the photo-generated charge carriers in the junction

If no further processes happen, the excited electron will fall back into the valence band and it will recombine with a hole, releasing its excess energy as thermalization. To prevent this so-called recombination, the charge carriers need to be separated.

So, once the mobile charge carriers are generated, they diffuse to the selective contacts, where they are separated by means of an electric field in the so-called depletion region. Such electric fields are produced by creating junctions of either different materials (heterojunctions) or the same material with different doping atoms (homojunction), which will generate impurities in the lattice [13].

The electric field sends holes and electrons to opposite directions. After creation of a p-n junction electrons will diffuse from the high electron concentration n-type side to the low electron concentration p-type material, since holes are the majority charge carriers. However, holes will diffuse into the n-type material. Due to above reasons in the depletion region, also known as space charge region, n-type material becomes positively charged, while the p-type material becomes negatively charged, see Figure 1.6.

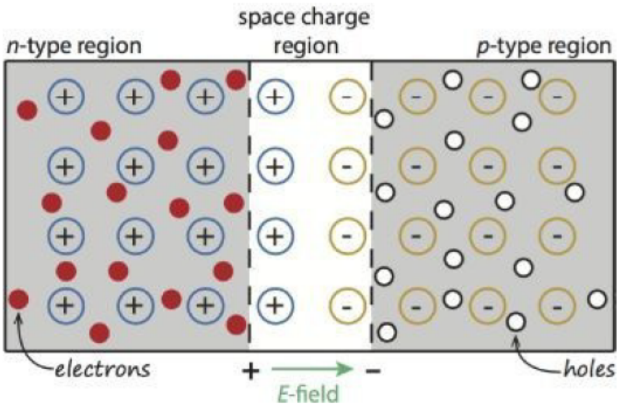

Figure 1.6: Formation of the space charge region with both n-type and p-type semiconductors to form a junction [4].

It is important to design a solar cell such that the electrons and holes can reach the membranes before they recombine. The membranes are used so holes can flow out through one membrane, while electrons can flow out through the other membrane, which is formed by n- and p-type materials. This means that the time it requires for charge carriers to reach the membranes must be shorter than their lifetime.

Collection of photo-generated charge carriers at the terminals of the junction

The last step of the PV effect is the collection of carriers at the terminals of the junction. The chemical energy of the electron-hole pairs is converted into electric energy. In the depletion region the internal electric field drifts the electrons to the n-type region, while holes will be drifted to the p-type region for collection.

Finally, the separated carriers are collected at the outer side of the doped layers by highly conductive metal contacts. The difference in majority charge carriers creates a potential difference between the top and bottom contact. Moreover, by applying an external circuit the electrons flow from the n-type material to the p-type material, due to the experienced concentration difference.

1.3. Solar cell history and current techniques

The photovoltaic effect was firstly demonstrated by Edmond Becquerel in 1839. Research in PV applications has gained since that time. All PV devices use the previous explained photovoltaic effect to generate electricity, however the configurations and compositions of those cells do vary. Many different solar cell technologies for different applications are developed the last century and will be discussed in the coming sections. A division is made into 1^{st}, 2^{nd} and 3^{rd} generation solar cells in this thesis. The 1^{st} generation solar cells are wafer based, 2^{nd} generation cells are made out of thin-film technology and 3^{rd} generation solar cells refer to new innovative PV technologies, that are either very cheap due to abundant materials, or cells who exceed the SQ limit for single junction solar cells and can establish very high efficiency, widely known as multi-junction solar cells.

Wafer Based Solar Cells

1^{st} generation solar cells include both single- and multi- crystal wafer based solar cells. This technique is the oldest and most common used technology, due to their high efficiency. There are generally two types of first generation solar cells, who differ by crystallization levels. If the whole wafer is only one crystal, it is called single/mono crystal solar cell, while if wafer consist of crystal grains, it is called multi crystal solar cell.

Mono crystal solar cells can achieve higher efficiency, while production of multi crystal solar cell is easier and cheaper. Current record efficiency reported by Martin Green consists of 26.7% fabricated by Kaneka with a n-type rear Interdigitated Back Contact crystalline cell [17]. A drawback of 1^{st} generation solar cells is their 200-250 μm thick wafers and therefore relatively high production costs compared to other techniques. This has increased further research and a new generation of solar cells were unfolded, namely thin film devices to decrease the production costs.

Thin Film Technology Based Solar Cells

Thin-film technologies include: amorphous / micro-crystalline silicon (a-/µc-Si:H), cadmium telluride (CdTe), and copper indium gallium diselenide (CIGS). Although the efficiency of thin-film solar cells is lower than of c-Si solar cells, it still has some important advantages: (i) it is a lightweight, (ii) flexible technology, (iii) easy fabrication and (iv) good model system to demonstrate new light-management concepts [10]. Although c-Si dominates the market with a 95 % market share, thin-film silicon solar cells can be used for specific applications, such as curved surfaces on buildings. However, due to the price decrease, high efficiency and stability of crystalline silicon the interest for Thin Film Silicon Solar Cells (TFSSC) has significantly dropped in the last decades.

Thin-film silicon solar cells make use of p-i-n junctions instead of p-n junctions. The intrinsic layer is sandwiched between a p- and an n-layer. This structure results in an electric field across the p-i-n junction [18]. The intrinsic (undoped) layer is less defective than the doped layers. Moreover, charge carriers in this type of material have a lower recombination rate. Photo-generated charge carriers are separated and collected under the influence of an internal electrical field and therefore thin film based solar cells are drift driven instead of diffusion driven solar cells, like wafer based devices.

As mentioned earlier TFSSC suffer from lower efficiency compared to wafer based solar cells. The reported stabilized record efficiency of thin-film technologies are: 10.2 % for a-Si based solar cells fabricated by AIST, while 11.9% for μ-Si also fabricated by AIST. However, cadmium telluride (CdTe) has a reported efficiency of 21.0% fabricated by First Solar, and copper indium gallium diselenide (CIGS) even reached an efficiency of 22.9% by Solar Frontier [17].

Innovative new PV technologies

Third generation PV technologies have two different focuses, namely very cheap PV with abundant materials or using innovative concepts to generate high efficiency. Third generation PV technologies challenge the Shockley–Queisser (SQ) limit.

The SQ limit refers to the maximum theoretical efficiency of a solar cell, using a single p-n junction, to collect power from the cell where the only loss mechanism is radiative recombination. Moreover, some important assumptions are made, namely (i) one electron–hole pair can be excited per incoming photon, (ii) excess energy is lost as heat, (iii) illumination happens with non-concentrated sunlight and (iv) the semiconductor is transparent to photons with energy below the bandgap energy.

Third generation PV technologies are relatively simple to manufacture, for example perovskites. Perovskites are still in early stage of research, but already reached a record efficiency of 20.9% fabricated by KRICT [17].

Another example is multi-junction devices, which can generate high efficiency solar cells. Multi-junctions challenge the assumption of a single junction. Multi-junctions cells are fabricated by using 3-5 multi-junction cells based on spectrum splitting capability of multiple bandgap material. The current world record efficiency multi-junction solar cell is fabricated by Soitec based on GaInP/GaAs/GaInAsP/GaInAs solar concentrator with an outstanding efficiency of 46% [17]. However, a typical Si based multi junction cell consists of a-Si/nc-Si/nc-Si cell with a record efficiency of 14% [17].

Multi-Junction Devices

In a single junction solar cell all photon energies higher than the bandgap energy generate charge carriers in the intrinsic layer. A multi-junction solar cell is formed by stacking several different solar cells and therefore the light of the solar spectrum is preferentially absorbed in various absorber layers. The top absorber layer will absorb the highly energetic photons in the blue region of the spectrum and is transparent to yellow/red light. In this case the yellow/red light is able to transmit through the cell and will be absorbed by the bottom absorber layer.

Multi-junction devices are mostly made of absorber materials with different bandgap energies to achieve better utilization of the solar spectrum than single junction solar cells. If the photon energy is much higher than the bandgap energy, a large fraction of the energy is lost as heat. The use of multi-junction devices strongly reduces the thermalization losses [4].

1.4. Motivation Amorphous Silicon Germanium

Multi-junction cells with Si alloys have true potential for high conversion efficiency, because of the spectrum splitting capability. Silicon is a useful material to have in a solar cell, due to its high efficiency, stable nature, economically attractiveness and it even has the biggest market share [4]. Thin film silicon multi-junctions are interesting for niche application that require a high voltage.

For optimal spectral utilization, a triple junction silicon based device needs a silicon alloy with a bandgap between that of nc-Si and a-Si, which are the most straightforward and successful thin film si alloys [19]. a-SiGe:H has this bandgap between nc-si and a-Si.

a-SiGe:H has a tunable bandgap by varying the Germanium fraction in the layer. Therefore, for multi-junction solar cells the availability of device grade materials like a-SiGe:H allows fine tuning of the response of the cell to the solar spectrum.

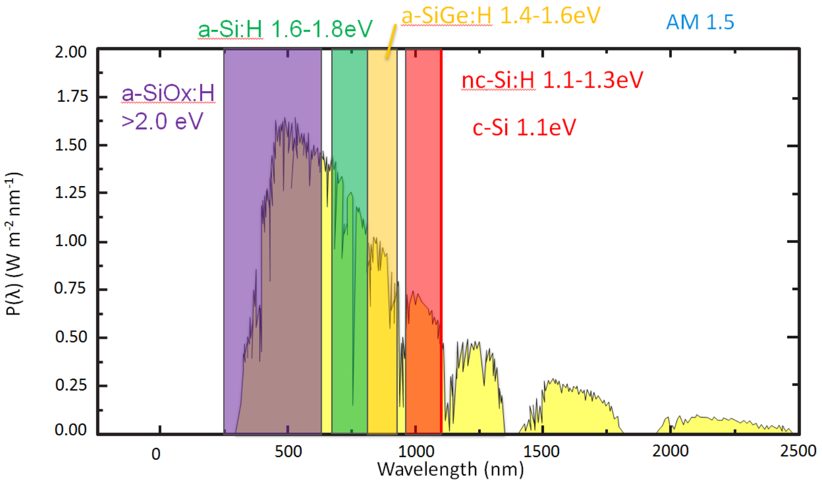

Figure 1.7: Bandgap ranges of various silicon alloys in the AM1.5G solar spectrum [5].

Figure 1.7 displays the opportunity of a-SiGe:H in a multi-junction device. Using a-SiGe:H as middle cell in between the a-Si:H top cell and nc-Si:H bottom cell can decrease thermalization losses and improves spectral utilization.

So due to previously mentioned opportunities a-SiGe:H will be used, which has a tunable bandgap between the previous mentioned nc-Si (1.1 eV) and a-Si (1.8 eV). However, the ranges of useful bandgaps are in between 1.4-1.6 eV, which still makes it an interesting building block.

1.5. Project Description and Outline

Summarizing, a-SiGe:H has a bandgap energy between that of nc-Si and a-Si. This makes it a very interesting material for silicon based multi-junction devices. In principle, a-SiGe:H can have a mobility bandgap energy ranging from close to that of germanium (1.0 eV) to a-Si:H (1.8 eV), depending on the germanium content. In practice the range of bandgap energies in efficient devices is much more limited (1.4-1.6 eV).

The overall goal of this project is to determine the range of device grade a-SiGe:H absorbers, that can flexibly be used in multi-junction devices. The research objectives include characterization on material- and device level. Firstly, the influence of the SiH_4/GeH_4 ratio, H_2 dilution, deposition pressure, deposition power and substrate temperature on the optical-, electrical- and material properties will be characterized. This should result in a range of device grade a-SiGe:H layers.

Secondly, the a-SiGe:H absorber is integrated in a single junction n-i-p substrate solar cell. The goal is to find a range of grading profiles, in terms of shape, width and thickness of device grade a-SiGe:H single junction devices. Another investigation focuses on if we can improve the device performance by introducing a buffer layer and what buffer layer type and thickness gives the greatest performance boost. This characterization will be done in terms of the V_{oc}, FF, J_{sc} and η.

Finally, a two-junction device will be processed to demonstrate the performance of the a-SiGe:H absorber.

The objective of this work, including the above mentioned milestones, can be summarized by the following statement:

”The characterization and determination of the range of device grade a-SiGe:H absorbers, that can flexibly be used in multi-junction devices, taking into account absorber bandgap, thickness, grading profile and buffer layers”.

This statement, related to the milestones, can be divided into the following research questions:

1. Which combination of deposition parameters can be used to process a range of device grade a-SiGe:H absorber layers?
2. Which bandgap grading profile in terms of shape, grading region width and absorber thickness should be used to process a range of device grade a-SiGe:H absorber single junction devices?
3. Which buffer layer and buffer layer thickness should be used to process a range of device grade a-SiGe:H absorber single junction devices?
4. To what extend can the a-SiGe:H absorber layer be manipulated for use in a multi-junction device?

This document is structured as follows. In this chapter the reader was introduced to PV technology and the importance of the research. Further theoretical background is given in Chapter 2. The theoretical background and the methodology will form the fundamentals of this research thesis. Chapter 3 will describe the methodology that is used during the experimental phase of this thesis project. A brief description of optical-, electrical- and material characterization methods and deposition techniques will be presented in this chapter. Chapter 4 will focus on the results of the a-SiGe:H film characterization.

The document will continue with n-i-p substrate single junction solar cell results in Chapter 5. Its main focus is on the intrinsic layer optimization, including GeH_4 flow rate, intrinsic layer thickness, bandgap profiling and grading series. This is followed by the buffer layer investigation. Combining all results will lead to Chapter 6, where two-junction cells will be displayed with a-SiGe:H as a bottom cell. This thesis will be finalized in Chapter 7 by the conclusions and recommendations, where a summary of the most important results obtained during this thesis and an outlook of possible options to further improve the performance of the tandem solar cells, as an indication for future research will be provided.

2

Theoretical Background

This chapter will introduce all fundamental concepts of physics and material related properties involved in PV and provide the theoretical background of this thesis. Firstly, in paragraph 2.1 specific properties related to the a-SiGe:H absorber layer will be discussed. The chapter is followed by optical, electrical and material properties. They are sequentially discussed in section 2.2, 2.3 and 2.4. The chapter ends with the device related properties. These are explained in detail in section 2.5.

2.1. a-SiGe:H absorber layer properties

In general, light is absorbed in all layers of the solar cell. All the absorption in layers other than the absorber layer is loss, which is called parasitic absorption [20]. Further, due to the limited thickness of the absorber layer, not all the light entering the absorber layer is absorbed. Incomplete absorption in the absorber due to its limited thickness is an additional loss that lowers the energy conversion efficiency [4].

The thickness of the absorption layer is therefore essential. The absorption coefficient in a direct bandgap material is much higher than in an indirect bandgap material. Thus, the absorber can be much thinner [4]. However, the absorber should be optically thick to absorb as much light as possible and the thickness of the absorber layer should not exceed the carrier diffusion length [21].

2.2. Optical properties

Light management is crucial in a solar cell. The incidence of light on a medium can lead to three different outcomes, namely light will be either be reflected by the surface, transmitted through the material or absorbed in the material. Ideally you would expect all incident light on a solar cell to be absorbed, however in real life this is not the case. The following paragraphs will mainly focus on the introduction of absorption, followed by reflection and transmittance, given by equation 2.1.

$$A + R + T = 1 \tag{2.1}$$

where transmittance, absorptance and reflectance are all unit-less quantities and sum to unity.

2.2.1. Optical absorption

For efficient solar cells we are interested in part of light which can be absorbed. The absorbed light is used for exciting charge carriers that can be used to drive an electric circuit.

Absorptance can be more specified by equation 2.2. Absorptance is calculated by the multiplication of absorption coefficient (α) and the thickness (d).

$$A(\lambda) = \alpha(\lambda) \cdot d \tag{2.2}$$

The absorption coefficient depends on wavelength and is related to the extinction coefficient, which will be given by spectroscopic ellipsometry tests and is given by equation 2.3. The absorption coefficient is crucial.

$$\alpha(\lambda) = \frac{4 \cdot \pi \cdot \kappa(\lambda)}{\lambda} \tag{2.3}$$

To calculate the absorption coefficient, firstly the optical properties need to be described. In general, the optical properties of an absorbing medium are described by a complex electric permittivity, which started from the Maxwell equations.

$$\tilde{e}(\lambda) = e'(\lambda) + ie''((\lambda) \tag{2.4}$$

When light passes through a medium, some part of it will always be attenuated. This can be conveniently taken into account by defining a complex refractive index. The complex refractive index, $\tilde{n}$, is defined as the square root of $\tilde{e}$ [4].

$$\tilde{n}(\lambda) = \sqrt{\tilde{e}} = n(\lambda) + i\kappa(\lambda) \tag{2.5}$$

Equation 2.5 shows that the extinction coefficient equals the imaginary part of the refractive index. The real part, n, of the complex refractive index, is the refractive index and is related to the phase velocity of the wave, while the imaginary part, κ , is the amount of attenuation when the electromagnetic wave propagates through the certain material [22].

Ideally, we would like a solar cell to absorb 100% of the incident light. Such an absorber is called optically thick and has a transmissivity very close to 0. As we can see from the Lambert–Beer law, equation 2.6, this can be achieved either by absorbers with a large thickness or with a very large absorption coefficient.

$$I^{abs}(\lambda, d) = I_0(\lambda)e^{-\alpha(\lambda)d} \tag{2.6}$$

where I(λ,d) is the light intensity inside the medium, $I_0(\lambda)$ is the initial intensity at the surface, d is the thickness, and α(λ) is the material corresponding absorption coefficient.

The absorptance can be expressed by the absorption coefficient, which plays an important role in TFSSC. Since the optical bandgap of a-SiGe:H films can be varied (from 1.4 to 1.6 eV) by changing the composition, the absorption coefficient can be thus increased at long wavelengths.

2.2.2. Optical reflection

The second outcome of light on a medium is reflection. If light travels from air to the medium and the incident angle lower than the critical angle, the light does not enter the material, but reflects of the surface. The part which is transmitted into the medium will travel through or will be refracted. Figure 2.1 shows that when light enters medium 1, a part of it is reflected, with an angle of incident light equal to the angle of scattered/reflected light. The transmitted light enters medium 2, where the angle of refracted light, Θ_t, is related with the angle of incidence, Θ_i.

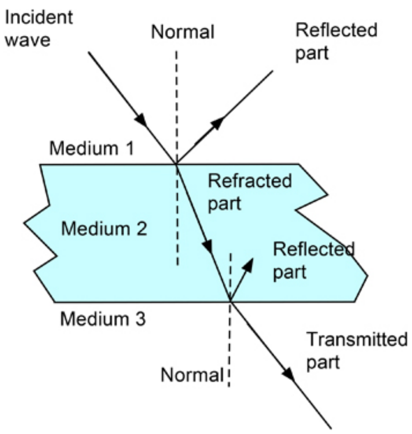

Figure 2.1: Scheme of light through a medium including reflected, refracted and transmitted light [6].

The characterization of reflection mostly involves the refractive index. The refractive index is the ratio of the velocity of light of a specified wavelength in air to its velocity in the examined substance. The higher the refractive index of the material, the more optically dense it is, which means the harder it will be for the light to travel through the material and vice versa. The refractive index of a material is often, for the sake of easy comparison, indicated with just one number. This is at a wavelength of 589 nm, which is seen as an average wavelength within the visible light spectrum [23].

However, the refractive index does vary over the entire spectrum depending on wavelength. The ratio of the sines of the incident and refractive angles of light in the tested liquid is equal to the ratio of light velocity to the velocity of light in vacuum, also known as Snell's Law [24].

$$n_1 \cdot sin\Theta_i = n_2 \cdot sin\Theta_t \tag{2.7}$$

Relations between the magnitudes of the incident, reflected and refracted fields are given by Fresnel equations, 2.8 and 2.9. A distinguishment between parallel and perpendicular polarized light is important to mention. When the electric field is parallel to plane of incidence the wave is P-Polarized. However, if the electric field is perpendicular to the plane of incidence, the wave is S-Polarized, which comes from the German word for perpendicular, namely 'Senkrecht'.

$$R_S = \left| \frac{n_1 cos\Theta_i - n_2 cos\Theta_t}{n_1 cos\Theta_i + n_2 cos\Theta_t} \right|^2 \tag{2.8}$$

$$R_P = \left| \frac{n_1 cos\Theta_t - n_2 cos\Theta_i}{n_1 cos\Theta_t + n_2 cos\Theta_i} \right|^2 \tag{2.9}$$

The sun emits unpolarized light, so it will emit the same amount of S and P polarized light. So, for the case of normal incidence, $\Theta_i = \Theta_t = 0$ there is no distinction between S and P polarization, and therefore at spectral reflectance the total reflectance equals half of the sum of the S and P type reflectance. Combining equation 2.7,2.8 and 2.9 will finally lead to the overall equation 2.10.

$$R = \left| \frac{n_1 - n_2}{n_1 + n_2} \right|^2 \tag{2.10}$$

In order to reduce reflection an anti-reflective coating can be applied. The reflection of an interface can be reduced if another layer is introduced with refractive index n_2. Every refractive index n_2 that satisfies $n_1 < n_2 < n_3$ will reduce the total reflection. However, there is an optimum refractive index, which is equal to n_2 of equation 2.11.

$$n_2 = \sqrt{n_1 \cdot n_3} \tag{2.11}$$

whereby the refractive index of n_2 should be in between n_1 and n_3, which relates to Figure 2.1.

Moreover, a change in deposition conditions, can lead to significant differences in optical reflection and therefore also in the refracted index, which will influence important solar parameters. For example, in thin film organic solar cells, light trapping schemes need to be modified due to the low refractive index of the substrate, or practical difficulties of employing large textured structures.

2.2.3. Optical transmittance

The third outcome is related to transmittance. The transmittance is the ratio of the light passing through with respect to the light incident on the medium, as can be seen in Figure 2.1. A very important consequence of Snell's law is total reflection. If $n_2 > n_1$, there is a critical angle at which light can no longer leave the layer with n_2, Hence if $\Theta_2 \geq \Theta_{crit}$, no light will be transmitted, but everything will be reflected back into the layer [4].

$$sin\Theta_{crit} = \frac{n_1}{n_2} \tag{2.12}$$

Therefore, it is important to keep the transmittance to the outside of the medium on a minimum level, so all the light will be refracted in the solar cell layers.

2.3. Electrical properties

After introduction of the optical properties the next important property for the absorber layer is electrical, divided in conductivity and activation energy.

2.3.1. Conductivity

Conductivity is an intrinsic material property. It is defined as the degree to which a specified material conducts electricity, calculated as the ratio of the current density in the material to the electric field which causes the flow of current. This is the amount of electrical current a material can carry or its ability to carry a current. There is a relation between conductivity and resistivity, which leads to the total formula, given by equation 2.13.

$$\sigma = \frac{1}{R_{TEMP}} \frac{d_{gap}}{d \cdot l} \tag{2.13}$$

As can be seen, the conductivity is the conductance measured in Siemens per meter. It depends on the temperature dependent resistance, R_{TEMP}, the layer thickness, d, the contact length, l, and the gap between the contacts, d_{gap}.

Electrical conductivity gradually increases as the temperature is increased, see equation 2.13. The number of free electrons in a unit volume of the semi-conductor increases exponentially with an increase in the temperature. Thus, the resistivity decreases with a temperature increase. Doping can influence the conductivity as well.

2.3.2. Activation Energy

Activation energy is a measure of the amount of energy required to excite an electron to a state where it can conduct. The average energy level of an electron in a material is called the Fermi level. In an intrinsic semiconductor material, the Fermi level will be halfway the bandgap. In a doped semiconductor material, the Fermi level will be closer to one of the bands than the other [5]. Low activation energy will contribute to higher conductivity, due to the fact that more electrons can be conducted. The activation energy is related to the conductivity, through the Arrhenius equation, given by equation 2.14.

$$\sigma(T) = \sigma_0 \cdot exp\left(\frac{-E_{act}}{k_B T}\right) \tag{2.14}$$

with σ_0 is the material dependent conductivity constant, k_B is the Boltzmann's constant and T is the temperature in Kelvin. This means that E_{act} can be seen as a slope, when the conductivity is measured at a certain temperature, see Figure 2.2. The activation energy is sensitive to the temperature.

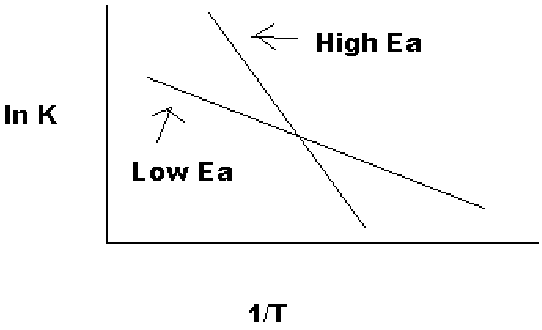

Figure 2.2: The relation between temperature, conductivity and activation energy [7].

2.4. Material properties

Lastly the typical material properties of amorphous materials will be discussed.

2.4.1. Amorphous Silicon

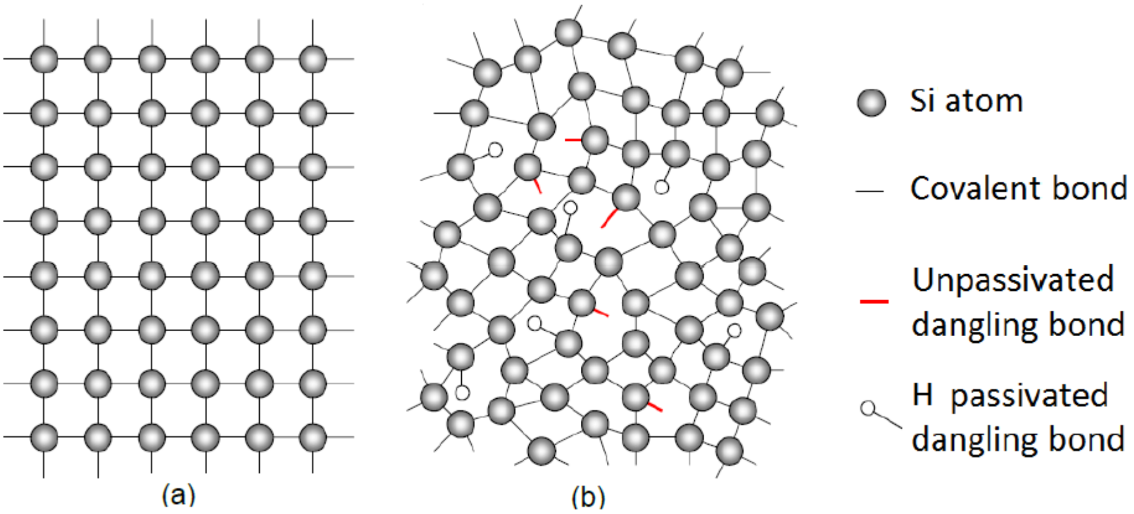

Figure 2.3: Overview of c-Si atom structure **(a)** and a-Si:H structure **(b)** [5].

Crystalline silicon is a well known semiconductor. In c-Si, atoms are arranged in a diamond-like lattice structure, which is consistent with the underling chemical bonding properties [10]. Therefore, crystalline structures are generally very ordered, which generates strength and rigidity. However, amorphous polymers are different, because they have flexibility and elasticity, but lack long range order. Small deviations in both the bond angle and the distance cause dangling bonds.

These dangling bonds can be passivated by additional hydrogen. Part of the silicon atoms make covalent bonds with only three or two other silicon neigbours and the remaining valence electrons bond to hydrogen atoms [10]. Passivation with hydrogen is of great importance to reduce the dangling bonds and thereby prevent deterioration of the electronic properties. Therefore, a change in deposition parameters can affect the amorphous structure of the a-SiGe:H material.

2.4.2. Defects

This paragraph will focus on defects. In c-Si the periodicity of the lattice, results in the existence of clearly defined energy bands and a corresponding forbidden bandgap in between. Due to the spatial disorder in the atomic structure of a-Si:H the periodicity of the potential energy associated with the lattice in crystalline silicon is disturbed. This leads to a broadening of the conduction and valence bands into the so-called tails, which extend into the bandgap [25]. Due to the fact that c-Si contains just a few defects, the density of states in the bandgap is approximately zero.

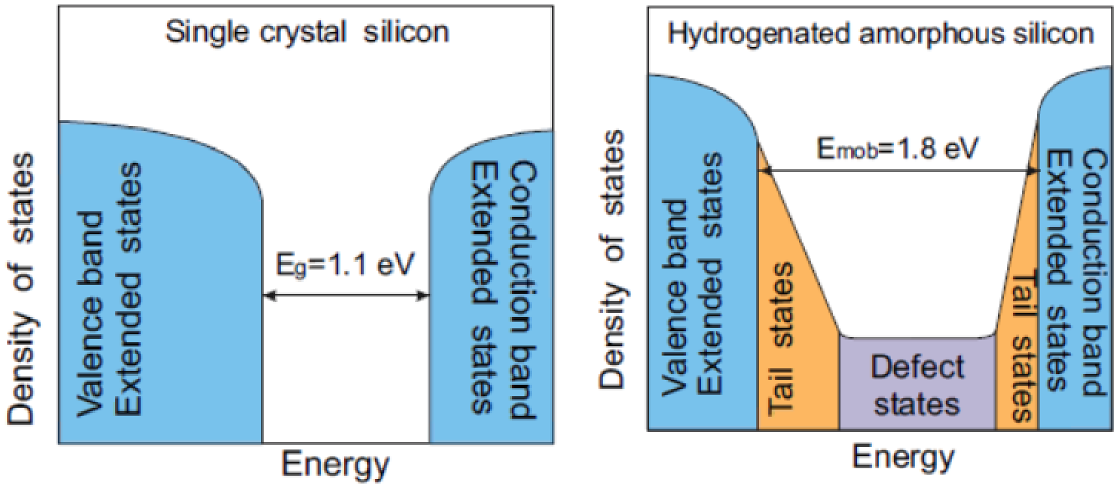

(a) (b)

Figure 2.4: Schematic representation of density of states distribution in c-Si **(a)** and a-Si:H **(b)**.

Figure 2.4 shows the difference between a-Si and c-Si in case of Density of States (DOS) profiles. The DOS of a system describes the number of states per interval of energy at each energy level available to be occupied. Therefore, the DOS is the number of different states at a particular energy level that electrons are allowed to occupy. A high 'DOS' at a specific energy level means many states available for occupation. However, a DOS of zero means that no states can be occupied at that energy level. Thereby, a low DOS automatically leads to a higher chance of forming unbounded valence electrons, also known as dangling bonds.

The band edges of a-Si are distributed over a range of energy levels, which will lead to the tail states. The density of states in both valence and conduction band does decrease significantly with the energy. In between those tail states the defect states are present, mostly in the form of dangling bonds. Due to the continuous DOS distribution the transport in amorphous silicon is much more complex than in its crystalline counterpart. In a-Si:H the electric current is carried not only in extended states of the conduction and valence band, but the states in the mobility gap can also be involved in the transport [25]. It is important to mention that a-Si:H and a-SiGe:H are comparable.

2.4.3. Composition

The composition of the material depends extensively on the deposition parameters. The composition determines the material properties and thereby most optical and electrical parameters of the absorber layer.

2.4.4. Crystallinity

Crystalline structures are generally opaque because the structure acts to reflect light. One way of recognizing amorphous polymers is by their transparency. As the percentage crystallinity increases the polymer becomes progressively less clear.

The crystallinity of the material is estimated through the following equation:

$$X_C = \frac{I_{c-Si}}{I_{c-Si} + I_{a-Si} \cdot \gamma} \tag{2.15}$$

Where X_C is the crystalline fraction, I_{c-Si} is the crystalline peak area, I_{a-Si} is the amorphous peak area and lastly γ is the correction factor for cross section difference for phonon excitation of c-Si with respect to a-Si. The TU Delft PVMD group adopts 0.8 as a standard for γ and therefore this is used as correction factor [26]. However, to calculate the overall crystallinity Germanium should be added as well to equation 2.15.

2.4.5. Bandgap

The important bandgap to use in this thesis is the optical bandgap, which is the threshold for photons to be absorbed. To determine the optical bandgap of a-SiGe:H, the Tauc-Lorentz model [27] was fitted to the SE data measured. Those film depositions are performed on glass substrates. To verify this bandgap two other optical bandgaps are calculated by using the absorption coefficient. The absorption coefficient from the SE measurement is used to calculate the Tauc bandgap, E_{TAUC}.

$$E_{TAUC} = (\alpha \cdot h \cdot v)^{1/r} \tag{2.16}$$

Equation 2.16 shows the calculation of the Tauc bandgap. The value of the exponent r denotes the nature of the transition, which is indirect for a-SiGe:H and has a value of 1/2 [28]. Typically, a Tauc plot shows the quantity hν (the energy of the light) on the abscissa and the quantity $(\alpha h\nu)^{1/r}$ on the ordinate. The line will be extrapolated and the Tauc bandgap can be calculated.

Another way to verify the optical bandgap is to calculate the E_{04} bandgap. It is defined as the energy at which the absorption coefficient of the material equals 10^4 cm^{-1} [29]. The absorption coefficient is calculated using equation 2.3, where the spectral extinction coefficient is obtained from the SE model fit. Fitting and comparing the E_{04} and E_{TAUC} bandgaps provides a reliable value for the optical bandgap.

2.5. Solar cell device properties

After material related properties, the focus in this paragraph will be on device characterization. The most important parameters to characterize the final solar cell are explained and will help for better understanding.

2.5.1. Parameters PV device

The Peak Power (P_{MPP}), the short circuit current density (J_{sc}), the open circuit voltage (V_{oc}) and the Fill factor (FF), are the most important parameters to characterize the solar cell. All these parameters are determined from an illuminated J-V characteristics curve, except for the J_{sc} which is determined from the EQE measurements. The conversion efficiency (η) of the solar cell can be determined from those parameters.

It is important to mention that all measurements should be performed under standard test conditions (STC), which means that the total irradiance measured on the solar cell is equal to 1000 $\mathrm{W/m^2}$, the spectrum should be AM1.5 as discussed earlier and the temperature of the cell is kept constant at 25 °C.

The first important parameter is the I_{sc}, which is the current that flows through an external circuit if the electrodes are short circuited. This means that no voltage is applied, V=0 and therefore R=0. The short circuit current depends on the photon flux incident on the solar cell and is determined by the spectrum of incident light [4]. The I_{sc} depends on the area of the solar cell and to remove the area dependence the short-circuit current density, J_{sc} is used to describe the maximum current delivered by the solar cell, given by equation 2.17.

$$J_{SC} = \frac{I_{SC}}{A_{cell}} \tag{2.17}$$

Secondly, the V_{oc} is the voltage at which no current flows to the external circuit, I=0, so the circuit is open and no load is attached. The V_{oc} corresponds to the forward bias voltage, at which the dark current density compensates the photocurrent density, given by equation 2.18.

$$V_{OC} = \frac{n_{ideal} \cdot k_B T}{q} \cdot ln\left(\frac{J_{sc}}{J_0}\right) \tag{2.18}$$

In this formula $\mathrm{n_{ideal}}$ is the ideality factor, indicating how closely the solar cell approaches ideal diode behaviour. $\mathrm{n_{ideal}}$ depends on recombination mechanisms of the solar cell. The term $k_B T/q$ is known as the thermal voltage and consists of the Boltzmann constant, the temperature and the elementary charge. Around 300K the thermal voltage is roughly equal to 0.0259 V. J_{sc} typically has a small variation on the V_{oc}. However, the J_0 can vary by orders of magnitude. The saturation current density, J_0, depends on the recombination in the solar cell. Therefore, V_{oc} is a measure of the amount of recombination in the device.

The third parameter is the maximum peak power, P_{MPP} and will be explained by Figure 2.5. The point at which the product of the voltage and current is maximal is called the maximal power point, calculated by equation 2.19. Operating at MPP is important, since it optimizes the operation and thereby power output of PV systems.

$$P_{MPP} = V_{MPP} \cdot I_{MPP} \tag{2.19}$$

Figure 2.5 indicates that V_{MPP} and I_{MPP} are both lower than the V_{oc} and I_{sc}. After introducing all parameters the Fill Factor (FF) can be calculated, which is the ratio between maximum power generated by a solar cell and the product of the V_{oc} and I_{sc}. The Fill factor is a measurement tool to indicate the quality of the solar cell. Therefore, graphically the FF is the area in between the x-axis and y-axis, below point C.

$$FF = \frac{J_{MPP} \cdot V_{MPP}}{J_{SC} \cdot V_{OC}} = \frac{I_{MPP} \cdot V_{MPP}}{I_{SC} \cdot V_{OC}} \tag{2.20}$$

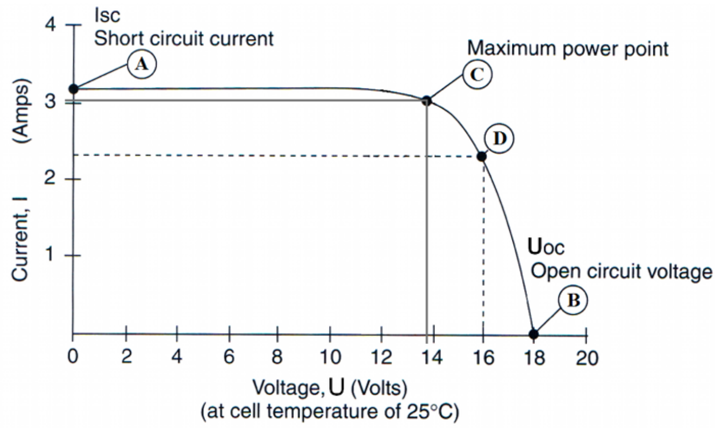

Figure 2.5: Schematic representation of basic principles behind the J-V and P-V curve [8].

The FF is directly affected by the values of the series resistance, shunt resistances and diodes losses. Increasing the shunt resistance (R_{sh}) and decreasing the series resistance (R_s) will lead to a higher FF, thus resulting in greater efficiency, and bringing the cell's output power closer to its theoretical maximum [30].

The parallel, or shunt, resistance, R_{sh}, represents the measure of isolation of the positive and negative terminals of the solar cell. A lower parallel resistance allows more current to leak from positive to negative terminal which prevents the current to be used in an external circuit, mostly affecting the operational current. The value of R_{sh} is mainly affected by quality of solar cell manufacturing and should be maximized [31]. The R_s normally has multiple causes, namely (i) the movement of current through the emitter and base of the solar cell, (ii) the contact resistance between the metal contact and the silicon and (iii) the resistance of the top and rear metal contacts [32].

The effects of the R_{sh} and R_s are visualized by Figure 2.6.

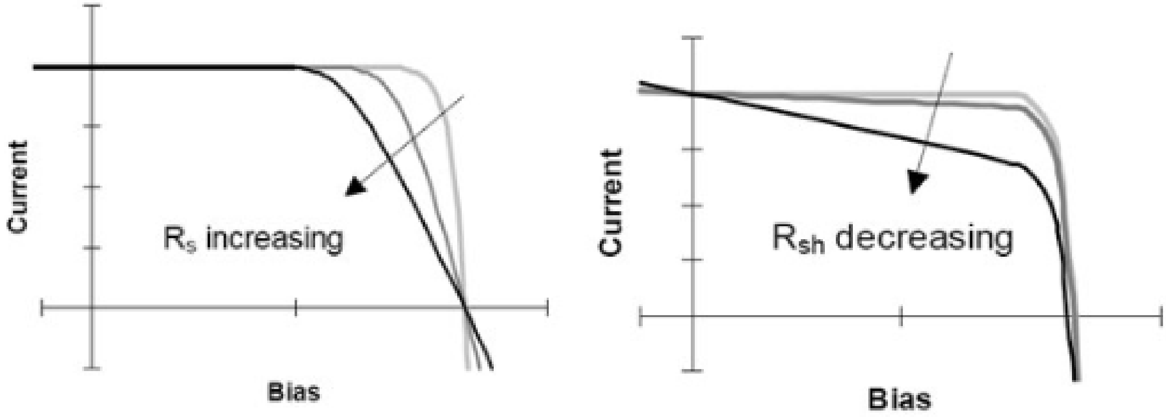

(a) (b)

Figure 2.6: Effect of increasing series resistance (R_s) **(a)** and decreasing shunt resistance (R_{sh}) **(b)** on the I-V curve [9].

Finally, all parameters are defined to calculate the conversion efficiency of the solar cell, η. The conversion efficiency is calculated as the ratio between the maximum generated versus the incident power, given by equation 2.21.

$$\eta = \frac{P_{MAX}}{P_{IN}} = \frac{J_{MPP} \cdot V_{MPP}}{P_{IN}} = \frac{J_{SC} \cdot V_{OC} \cdot FF}{P_{IN}} \tag{2.21}$$

Solar cell parameters can be enhanced by deposition parameters. For example, grading can influence the I_{sc}, V_{oc}, FF and therefore the η of the solar cell significantly.

The last important device parameter is the EQE. The external quantum efficiency EQE(λ) is the fraction of photons incident on the solar cell that create electron-hole pairs in the absorber which are successfully collected. As can be seen in the definition, the EQE is wavelength dependent and is usually measured by illuminating the solar cell with monochromatic light of wavelength λ and measuring the photocurrent I_{ph} through the solar cell [4].

$$EQE(\lambda) = \frac{I_{ph}(\lambda)}{q\Phi_{ph,\lambda}} \tag{2.22}$$

where $\Phi_{ph,\lambda}$ is the spectral photon flow incident on the solar cell. Since I_{ph} is dependent on the bias voltage, the bias voltage must be fixed during the measurement. An important factor of EQE will be the difference between short and long wavelengths.

Losses can be defined into subgroups, namely optical losses and electrical losses. Optical losses happen at the front of the device, where part of light is lost due to external reflection. At the back side of the device, part of the long wavelength light is lost by transmission through the gaps between the rear electrodes whereas another part is internally reflected toward the front side, where even a part of it further escapes. However, electrical losses depend on the spectral region of occurrence: like short wavelength so in between 350 and 600 nm (ultraviolet-blue), medium between 600-1000 nm (visible range) and long for 1000-1200 nm (infrared region). The shape of the EQE curve is determined by optical and electrical losses such as parasitic absorption and recombination losses [4].

All the above parameters will be used to finally characterize both single- and multi-junction solar cells.

2.5.2. Light Induced Degradation

It is well known that the electrical properties of Si:H based materials suffer deterioration under light exposure. This Light Induced Degradation (LID) behaviour is known as the Staebler–Wronski effect [33]. The Staebler–Wronski Effect (SWE) refers to light-induced metastable changes in the properties of hydrogenated amorphous silicon [34].

The defect density of hydrogenated amorphous silicon (a-Si:H) increases with light exposure, causing an increase in the recombination current, caused by the creation of defects that act as recombination centers, which will reduce the efficiency of the solar cell [35]. These LID problems can be partly solved using a-SiGe:H with a low bandgap [36].

Reduction of hydrogen is another option to reduce the degradation, but it will also reduce the defect passivation and lower the material quality. The performance loss by light-induced degradation of a-Si:H solar cells can be around 16% and between 30-40% for a-SiGe:H depending on material quality and germanium content [37]. Moreover, the SW effect appears to diminish for multi-junction solar cells. Reported stabilized efficiency only show a relative drop of 18% in efficiency of an a-Si:H/a-SiGe:H/nc-Si:H 3J solar cell [31].

One of the reasons for this difference is that the photocurrent for multi-junction solar cells is much lower than what individual single-junctions can achieve, which limits shunt resistance losses [31]. However, LID still has a significant influence on the long term stability of solar cells and will therefore be tabulated in this thesis.

3

Methodology

This chapter will concern a discussion of the equipment and software used to do measurements on both cell and device level. A brief introduction of the working principles behind the fabrication process is given. The process will be followed by measurement tools and techniques.

3.1. Deposition process

All depositions are done in the Else Kooi Laboratory on the TU Delft in a cleanroom 10000. Cleanrooms maintain extremely low levels of particulates, such as dust or vaporized particles. Cleanrooms are typically quantified by the number of particles per cubic feet at a predetermined molecule measure. For comparison the ambient outdoor air in a typical urban area contains 35,000,000 particles for each cubic feet which shows the level of filtering and extraction of particles in a cleanroom 10000.

3.1.1. n-i-p configuration

TFSSC can consist of two different configurations, namely p-i-n (superstrate) or n-i-p (substrate) structure, where the intrinsic absorber layer is sandwiched between the p and n doped layers. Figure 3.1 schematically displays those different configurations.

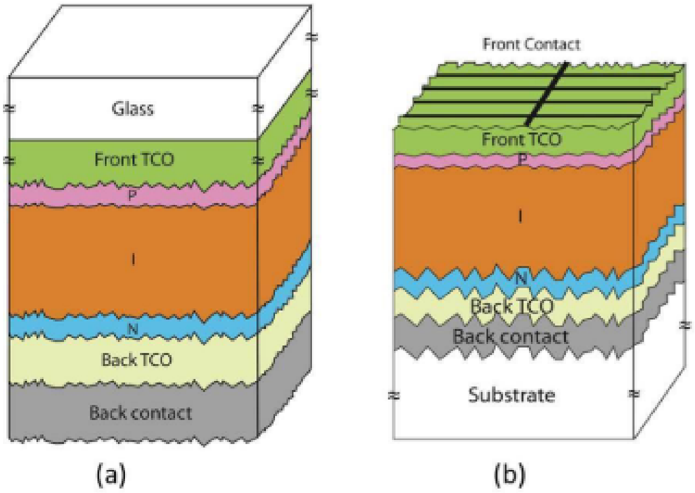

Figure 3.1: Configuration of typical single junction film solar cell in p-i-n superstrate **(a)** and n-i-p substrate structure **(b)** [10].

The p-i-n solar cell fabrication starts with glass, followed by deposition of the front Transparent Conductive Oxide (TCO). Incoming light enters the solar cell from the top, through the transparent glass.

Most electron-hole pairs will be generated near the side where light is incident. This means the carrier type collected by the top doped layer will, on average, not have to travel as far through the i-layer as the carrier type collected by the bottom doped layer. Therefore, it is useful to deposit the p-layer first and use n-i-p structure, since holes are less mobile than electrons. In n-i-p structure the process starts with deposition of a back contact on top of the substrate, followed by a back TCO.

The use of substrate n-i-p configuration can have different advantages or disadvantages. An advantage of n-i-p substrate deposition is that the most critical and sensitive top electrode/p-type window layers are deposited last and are not exposed to subsequent plasma.

3.1.2. Process overview

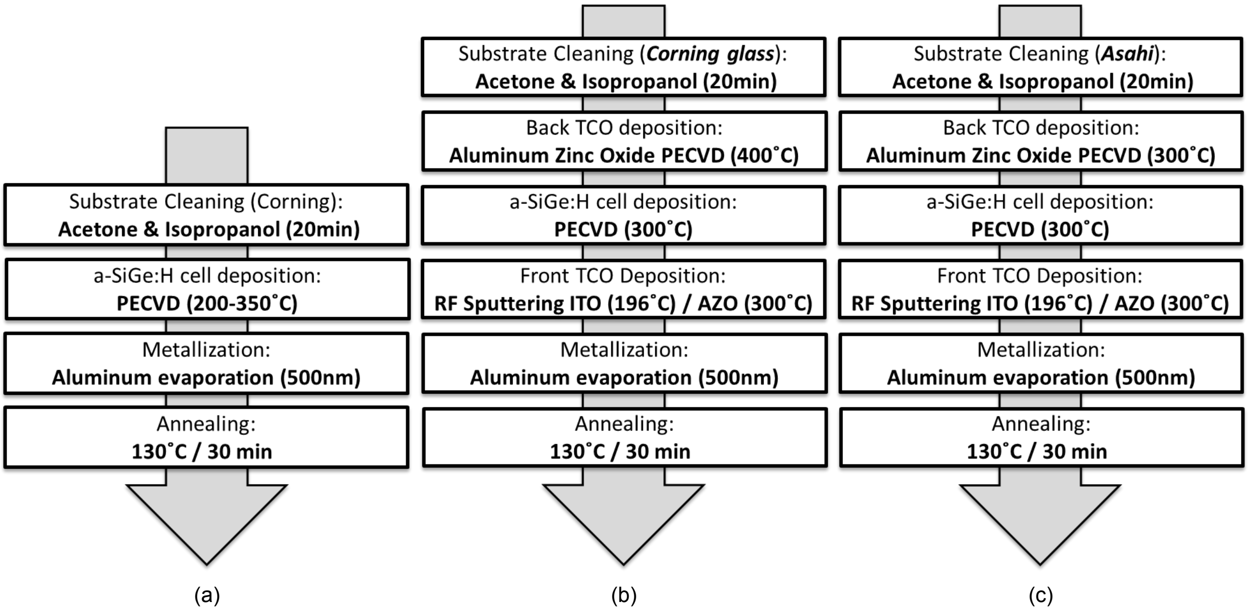

Figure 3.2: Flowchart of fabrication process of cell characterization films **(a)**, Corning glass as substrate for solar cells **(b)** and Asahi glass as substrate for solar cells **(c)**.

Figure 3.2 displays the flow chart of the fabrication process of the layers, followed by fabrication process of solar cells. In the coming paragraphs all processes will be explained in further detail. The fabrication will be followed by the measurement tools and techniques.

3.1.3. Substrate preparation

Corning® Eagle XG glass was first cut into pieces of 25 by 100 mm, after which they were cleaned in an ultrasonic bath with acetone and isopropanol. Cleaning in an ultrasonic bath can be done up to 6 glass substrates per session. First a 10 minute cleaning in acetone was applied. The substrates were dried with compressed nitrogen and followed by a 10 minute cleaning in an isopropanol bath. However, while processing solar cells also Asahi-VU substrate was prepared, following the same procedure as explained for Corning® Eagle XG substrate. Asahi is textured SnO_2 coated on glass, which can be used for better light trapping.

3.1.4. Plasma Enhanced Chemical Vapour deposition

The current industrial technique for the deposition of thin film amorphous solar cells is plasma-enhanced chemical vapor deposition (PECVD) [38]. PECVD uses a chemical reaction of gas phase precursors to accomplish growth on a substrate. One of the main reasons for its usage is the capability to operate at lower temperatures (200-400°C) compared to thermally driven CVD (600-800°C), while maintaining quality and homogeneity. In this project the `AMIGO RF-PECVD Cluster tool by Elettrorava s.p.A` is used and will be explained.

In PECVD a plasma which consists of ionised gas species (ions), electrons and some neutral species in both ground and excited states. The plasma is usually ignited and sustained by applying a high frequency voltage (microwave frequencies, ultrahigh frequencies or radio frequencies) to a low pressure gas. In the plasma inelastic collisions take place between electrons and gas molecules forming reactive species, such as excited neutrals and free radicals, as well as ions and electrons. In essence the electrons acquire sufficient energy from the applied electric field to create highly reactive species without significantly raising the gas temperature [39].

It is important to mention that silane, germane, methane, hydrogen and carbon dioxide are used in PECVD as source of silicon, germanium, carbon, hydrogen and oxygen. Additionally, diborane and phosphane are used as doping gas for the p- and n-type materials.

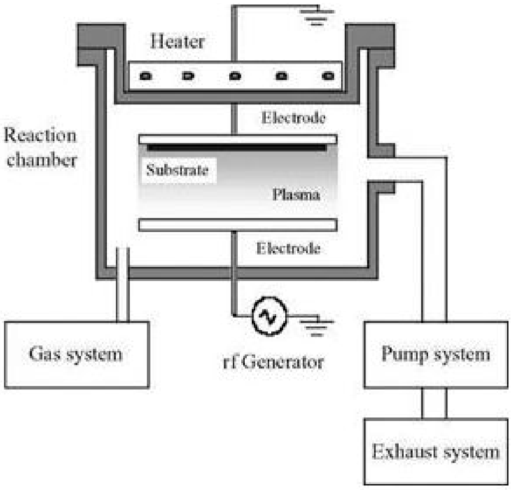

Figure 3.3: Schematic diagram of a RF PECVD deposition system [11].

A schematic diagram of a RF PECVD deposition system is shown in Figure 3.3. This systems contains a high vacuum reaction chamber with coupled parallel electrodes, RF power feedthrough and holders and heaters for the substrate. The next important asset is the gas system, which controls the inflow of different gasses in the chamber. Another important aspect is the pumping system, which usually consists of both a turbomolecular pump and a mechanical rotary pump, which can handle reactive gasses [11]. The last important asset is the controlling system.

The deposition by PECVD can be divided into four steps [40] and can be found in Appendix A. Different RF power, gas pressure, temperature, deposition time and gas flows can be used. Hydrogenation is done during the PECVD process and therefore should not be performed separately.

3.1.5. Transparent Conductive Oxide deposition

After the PECVD deposition the front TCO is deposited. TCO's are both optically transparent and electrically conductive. This is done by establishing a high lateral conductivity to the metal electrodes for electrons. Moreover, using a suitable thickness will increase the light trapping mechanisms for the TCO, and therefore a TCO also acts as an anti-reflection coating (ARC). The TCO is deposited using radio-frequency (RF) magnetron sputtering.

RF magnetron sputtering supports the deposition of thin layers on a substrate by bombarding the target material with highly energetic atoms or ions. In this technique, the target is bombarded with Argon plasma, and the substrate is placed in front of the target at an appropriate distance [41]. Magnetron sputtering is widely seen as a relatively a low-cost and easy control method for film growth, especially suitable for large-scale film deposition.

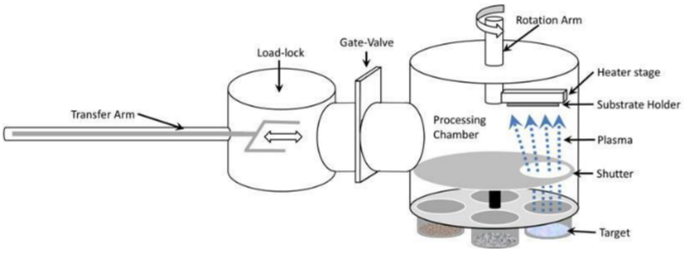

Figure 3.4: Schematic overview of sputtering system PVMD Group [10].

The RF magnetron sputtering system used in the PVMD group is a multi-target system, a `Polyteknik AS cluster tool`, as displayed in Figure 3.4. In sputtering systems, the cathode, which is the electron emitter, is the target material. The anode, which is the electron receiver, is usually the vacuum chamber wall or the substrate. By applying an RF power, sputtering from a dielectric or electrically insulating target material can be accomplished [10].

The deposition chamber has a temperature of 196°C, a power of 135 W and a pressure of 2.2 x 10^{-2} mbar during deposition. This will ensure that no damage is done during the sputtering process. However, exposing the sample to high power should be taken into consideration, because it can damage the lastly deposited p-layer.

Different TCO's are used, namely Aluminum (doped) Zinc Oxide (AZO) and Indium Tin Oxide (ITO). ITO has a target of 10 % SnO_2 and 90 % In_2O_3. AZO has a target of 2 % Al_2O_3 and 98 % ZnO. The deposition of AZO happened in the previously mentioned PECVD tool. The same plasma frequency is used and all working principles between the ITO and AZO deposition tool are the same. However, the deposition chamber has a temperature of 300°C, a power of 400 W and a pressure of 2.6 mbar.

3.1.6. Electron Beam Evaporation

The process is followed by metallization, where the substrate is placed in a holder, which can hold 4 substrates and is covered with a shadow mask facing the evaporating metal. Evaporation of metal by electron beam deposition is done by `Provac PRO500S` metal evaporation tool. A 500 nm thick aluminum front contact is evaporated on the substrates.

The technique involves evaporation of a metal under high vacuum circumstances. Low pressure is used to avoid contamination of the film by residual gases and even increases the free path length of metal atoms. Additionally, to increase the uniformity of the metal layer, a slowly rotating (10-20 rpm) sample stage is used during the evaporation process [42]. The metallic sources are located at the bottom of the chamber, such that the metallic vapour flows upwards.

E-beam is a process where highly energetic electrons from an "electron source" are used to evaporate a material which condense on any surface in a vacuum chamber. The heat source of the electron beam evaporation method is the kinetic energy of the electrons and therefore the evaporant material is heated directly, which gives an efficient result [12]. These materials mostly include metals like aluminum, titanium and chromium.

Compared with other methods like sputtering and CVD, the deposition rate of E-beam evaporation is high, because the e-beam source is capable of heating materials to much higher temperatures than is possible using a resistive boat or crucible heater. Additionally, precise control and direct heating give accurate results and a higher purity of the material is maintained.

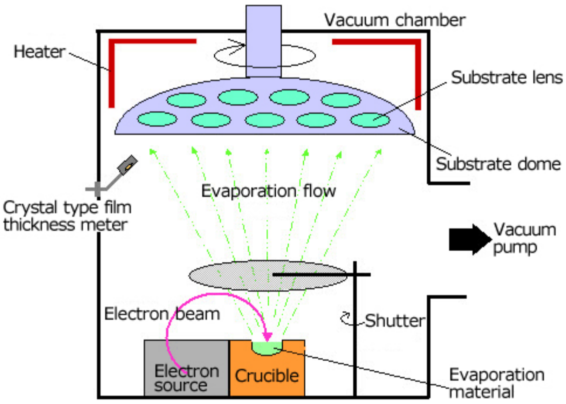

Figure 3.5: Schematic overview of evaporation of metal by electron beam deposition tool [12].

Figure 3.5 shows the schematic overview of the evaporation chamber. The evaporation target is aluminum and the substrate is placed in the upper part of the vacuum chamber. The thickness is measured by the crystal type film meter, while the electron source is generated in the bottom of the chamber. The shutter opens, exposing the aluminum target and the evaporation flow evaporates the metal on the substrates. The e-beam is finally switched off when the desired thickness is reached.

3.1.7. Annealing

After all previous deposition steps there is just one step left before measuring, namely annealing. Annealing is performed for contact adhesion and growth related stress release. The annealing process is done at a temperature below the actual deposition temperature, namely 130°C versus 200-350°C and an annealing step of 30 minutes in a `Heratherm Thermo Scientific oven` is performed.

3.2. Film Measurements

In the previous paragraph the main focus was on the fabrications. In this section an explanation will be given on the different measurement techniques used. Measurements are divided in material-, optical-, electrical- and device related measurements.

3.2.1. Raman Spectroscopy

Raman spectroscopy is a technique used to observe vibrational, rotational, and other low-frequency modes. Raman scattering arises from molecular vibration causing a change in polarizability. This means that intense Raman scattering occurs from symmetric vibrations which induce a large distortion of the electron cloud around the molecule [43]. One of the purposes of Raman spectroscopy is to quantify the (relative) fractions of crystalline and amorphous silicon in thin layer deposits.

Photons from the laser beam are scattered by the atoms in the samples lattice. Most photons undergo Rayleigh scattering, which means that the photon will not lose energy during the scattering event. A small fraction of scattered photons however, around one photon per 10^6 photons, experience inelastic scattering. This scattering is known as Raman scattering, where a fraction of the photons' energy causes an atom in the material lattice to vibrate [5]. This vibrational energy, known as a phonon, is lost as thermal energy. So, the Raman shift is the energy difference of the incident and the scattered photons.

The experiments are performed on a `Renishaw inVia Raman microscope` on a sample which is illuminated by a 633 nm red laser. The red laser is used, due to the fact that the penetration depth into the material is higher compared to the 514 nm green laser. Measurement settings were done at 5% power intensity with a scan time of 100 s and 1 accumulation. The Raman spectrum width is determined to be 0-2200 cm^{-1}, because all relevant stretching modes occur within this range.

Table 3.1: Raman stretching mode peaks for a-SiGe:H to their corresponding wavenumber.

Peak Wavenumber (cm^{-1})	Bonds	Stretching Mode	Source
80	a-Ge	TA [transverse acoustic phonon mode]	[44, 45]
160	a-Si	TA [transverse acoustic phonon mode]	[46]
177	a-Ge	LA [longitudinal acoustic phonon mode	[44, 45]
230	a-Ge	LO [longitudinal optic phonon mode]	[44, 45]
278	Ge-Ge	TO [transverse optic phonon mode]	[46]
320	a-Si	LA [longitudinal acoustic phonon mode]	[46]
380	Si-Ge	Stretching motions	[44–46]
390	a-Si	LO [longitudinal optic phonon mode]	[46]
470	Si-Si	Optic like modes	[46]
480	a-Si	TO [transverse optic phonon mode]	[46]
522	c-Si	Zone-centre optical phonon	[47]
620	Si-H	Wagging	[47]
1870	Ge-H	Stretching	[48]
2000	Si-H	indicating voids	[49]
2080	Si-H_2	Stability Issues	[49]
2100	Si-H	(HSM) on void rich surfaces	[50]

Table 3.1 displays different Raman stretching mode peaks with corresponding wavelength. The most important ones for this thesis are the (i) Ge-Ge stretching at 280 cm^{-1}, (ii) Si-Ge stretching at 380 cm^{-1}, (iii) a-Si stretching at 480 cm^{-1}, (iv) c-Si stretching at 512-520 cm^{-1} and (v) Si-H_2 stretching at 2080 cm^{-1}. (i) Shows the Ge-Ge stretching motions, which can be a good indication for the Ge-Ge bonds in the material. (ii) Shows the Si-Ge stretching motions, which can be a good indication for the Germanium fractions in the material. The (iii) mode corresponds to the a-Si peak which shows the amorphous fraction of the material, which will be plotted against the (iv) which represents the crystalline silicon fraction in the material. The amorphous peak is lower and wider compared to the sharp peak for crystalline materials. (v) Shows the Si-H_2 bonds, which can be an indicator for the stability of the material.

3.2.2. Spectroscopic Ellipsometry

Spectroscopic ellipsometry (SE) is used for optical measurements. SE measures the change in the polarized state of light upon light reflection. It is based on the polarization state, which is reflected or transmitted by a given sample. The light polarization is classified into p- and s-polarizations depending on the oscillatory direction of the electric field. Ellipsometry measures the two values (ψ, Δ), which represent the amplitude ratio ψ and phase difference Δ between the p- and s-polarizations. When sample structures are simple (i.e., only substrates), the amplitude ratio ψ is characterized by n, while Δ represents light absorption described by k or the absorption coefficient α [51].

Among many physical parameters, the bandgap and absorption coefficient of light absorbers are the most important physical quantities. The ellipsometry technique remains the only method by which the bandgap and the optical functions (i.e., the refractive index, extinction coefficient, and absorption coefficient spectra) can be determined accurately [51].

The hardware used to conduct the ellipsometry measurements is the `Woollam M2000-DI SE` including the `CompleteEASE` software. The light source covered angles from 55 to 70° with a wavelength ranges from 190-1700 nm. This angle spectrum is around the Brewster's angle, which is ±62.5°. Measurements are performed around the Brewster's angle, because the difference between p and s polarized light is largest.

A model is fitted to the measurement data. The model itself is a Cody Lorentz oscillator. The model uses a global fitting procedure to find the best fitting value while undergoing 10 iterations, taking into consideration the Mean Square Error (MSE). The MSE is proportional to the total difference between measured data and model calculations. A MSE of less than 10 is desirable for intrinsic layers below 300 nm, because it increases the reliability of the fitted model and given outcome data.

3.2.3. Reflectance, Transmittance and Absorptance

The absorptance, reflectance and transmittance measurements can tell about what happens with the incident light on a solar cell. The setup is able to measure both reflectance and transmittance and therefore with the use of equation 2.1 the total absorptance over the a-SiGe:H cell can be calculated. Comparing the absorptance and transmittance with the EQE gives a total overview of electrical or optical losses of a solar cell.

A `double beam Lambda 950 UV/vis spectrometer by Perkin Elmer` was used in this work. Double beam means that the light beam is split into a reference and a measurement beam, which are guided into an integrating sphere, which is coated with a highly reflecting material. To measure the transmittance the substrate is placed in front of the sphere, while reflectance measurements are done at the back of the sphere, where light is scattered back into the sphere.

The spectrometer can measure in three different ranges, namely near infrared, visible light and UV light. The used spectrometer contains a tungsten-halogen lamp for the visible and near infrared regions, while using a deuterium arc lamp for the UV region. Those two lamps switch at a wavelength of around 800 nm and therefore can give some small error near the switching point. Multiple mirrors are used in the spectrometer, but due to the fact that all measured spectra are calculated in relative terms, compared to the reference beam, no extra losses are detected.

3.2.4. Dark Conductivity

Dark conductivity is used to characterize electrical properties. The dark conductivity setup uses the `Keithley 6517A electrometer` with the `EACTM mainv1.1.1` software. The data can be used to calculate the dark conductivity, which is needed for to the final calculation of the activation energy.

In this setup the temperature ranges from 130-60°C including increments of 5°C. Moreover, a stabilization time of 60 seconds takes place after every temperature iteration. On each point there are 10 measurements with a time between the measurements of 3 seconds. The dark conductivity setup measures the current over this temperature range with a fixed bias voltage of 10 V. Therefore, it can be said that the dark conductivity measurement, measures the temperature dependent resistance, R_{TEMP} for the calculation of the conductivity, see equation 2.13.

3.2.5. I-V measurements

For device measurements the current-voltage characteristics are measured at room temperature by the `Wacom Solar Simulator`. The measurement setup is used to measure V_{oc}, FF and finally calculate the efficiency for solar cells under 1-sun illumination under STC. This includes AM 1.5 illumination at 25°C under 1000 W/m^2 illumination. The AM1.5 solar spectrum is realized by the solar simulator with two lamps (halogen and xenon). There is a variable illumination/spectrum to detect the presence of shunt in the measurement setup. This is used to analyze the electrical losses in the cells.

To verify that the measurement setup is performed under STC, the temperature and illumination are controlled and calibrated by two mono-crystalline silicon reference cells. Both those cells are manufactured by the Fraunhofer Institute for Solar Energy Systems.

3.2.6. EQE measurements

Another important measurement tool is the External Quantum Efficiency (EQE). The EQE measurement is done after the J-V measurements, by measuring the best 2-3 cells per sample.

The EQE measures the spectral response and gives the fraction of photons that is transferred to collected electron-hole pairs [10]. This means that reflection, transmission, absorption in non-photoactive layers, and collection losses do not contribute to the EQE.

This setup at the TU Delft measures short-circuit condition in the wavelength range from 300 to 850 nm for a-Si solar cells, using the AM1.5G spectrum. In this way overestimation of the J_{sc} due to lateral current collection and inaccuracy in defining the active area of the solar cells in J-V measurements is excluded [10], which is done by the calculated $\mathrm{J_{sc}}$ from I-V measurements.

3.2.7. LID 1000h Soaking

a-SiGe:H solar cells suffer from the well-known LID effect. Due to the reversibility of the degradation by annealing, the solar cells are annealed before the measurement starts. The setup includes three conditions, namely 50°C, 1 sun and 1000 hours. The light soaking experiment is performed by a setup chamber, which includes mirrored walls and six halogen lamps. The solar cells are placed under the halogen lamps and illuminated for 1000 hours.

During the experiment the solar cells are taken out and their I-V curve is measured by the `Wacom Solar Simulator`. Measurements will be done at 15, 24, 48, 100, 250 and 1000 hours to compare the LID effect over a period of time.

4

a-SiGe:H Material Characterization

This chapter will mainly focus on the first research question, namely which combination of deposition parameters can be used to process a range of device grade a-SiGe:H absorber layers. The paragraph focuses on the different deposition parameters and characterization results for a-SiGe:H films.

Deposition parameters can influence the optical-, electrical- and material properties of the a-SiGe:H film differently. It is important to use a proper combination of deposition parameters to process a range of device grade a-SiGe:H absorbers. Therefore, deposition parameter variations tests are performed on a-SiGe:H films and are summarized in Table 4.1.

Table 4.1: Deposition parameter ranges for material characterization.

Parameter	**Value**	**Unit**
GeH_4 flow rate	0.8-6.3	sccm
SiH_4 flow rate	20-40	sccm
H_2 flow rate	150-200	sccm
Substrate Temperature	120-210	°C
Deposition Power	2-8	W
Deposition Pressure	1.6-6	mbar

Appendix B shows the absorption coefficient curves for variation of GeH_4 flow rate, SiH_4 flow rate, H_2 flow rate, substrate temperature, deposition power and deposition pressure for a wavelength range from 400 - 1200 nm. Additionally, it consists of transmittance, reflectance absorptance measurements on films to show that the film depositions are uniform.

The bandgap used in this chapter is the one given by ellipsometry. The E_{04} and E_{TAUC} bandgaps are higher, however the trends are the same, see Appendix B. Additionally, all E_{act} graphs are displayed in Appendix B. Finally, if one deposition parameter is varied, all other deposition parameters are kept the same.

$$J_0 = qN_cN_v\left(\frac{1}{N_A}\sqrt{\frac{D_n}{\tau_n}} + \frac{1}{N_D}\sqrt{\frac{D_p}{\tau_p}}\right)e^{-E_g/kT} \tag{4.1}$$

Equation 4.1 displays the J_0 dependency on the bandgap and defects. J_0 equals the dark conductivity, due to the fact that V, L and A are constant. Therefore, the measured dark conductivity can be compared with the calculated dark conductivity. The DOS in the conduction- and valence band (N_c and N_v) depends on the GeH_4 flow rate in the film [52]. The exact concentration is related to the GeH_4 flow rate, but could not be measured. The defect dependency (between the brackets) changes with variation of GeH_4 flow rate [52]. However, the paper suggests N_c and N_v based on crystalline material. Therefore, many assumptions are made, which makes a conclusion harder. Nonetheless, it is likely to say that variation of GeH_4 flow rate changes the dark conductivity, related to the bandgap and the defect density.

4.1. Flow rate GeH_4

The first deposition parameter which is likely to influence the optical-, electrical- and material properties is the GeH_4 flow rate. Germane is used as a source for germanium. The chemical reactions can be found in Appendix A. The GeH_4 flow rate is varied between 0.8 and 5.3 sccm.

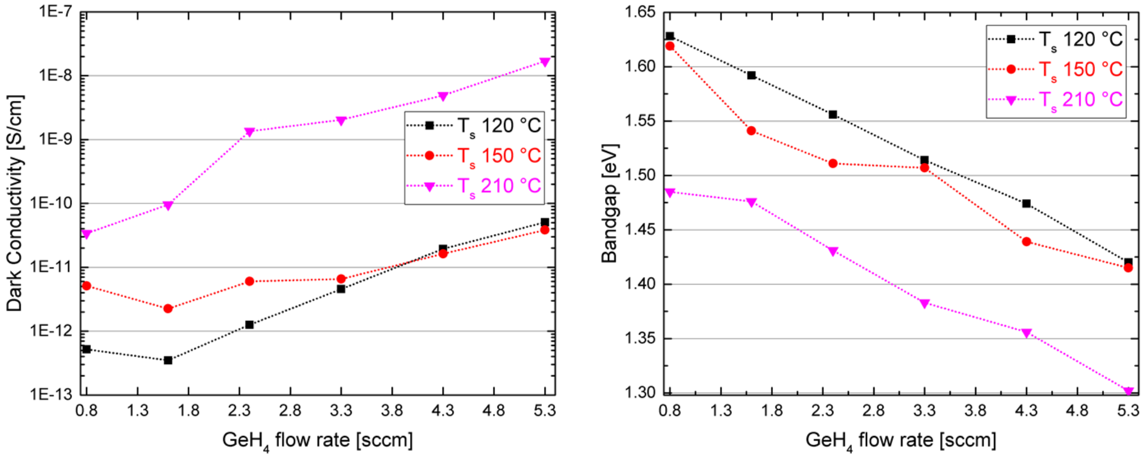

(a) (b)

Figure 4.1: The effect of variation of GeH_4 flow rate of a-SiGe:H film on the dark conductivity **(a)** and on the bandgap **(b)**.

The samples processed at a substrate temperature of 180°C have been omitted, since its dark conductivity was too fluctuating to get a reliable trend.

Figure 4.1a displays an increase in dark conductivity of 10^2 S/cm while increasing the GeH_4 flow rate between 0.8 and 5.3 sccm, which is likely related to the decrease in bandgap and increase of defect density. The E_{act} decreases accordingly by 100 meV between the highest and lowest used GeH_4 flow rate. Figure 4.1b shows that an increase of GeH_4 flow rate from 0.8 to 5.3 sccm decreases the bandgap by 0.2 eV. Different substrate temperatures show different bandgap energy levels, but the decrease in bandgap with increasing GeH_4 flow rate is almost linear for increasing substrate temperatures.

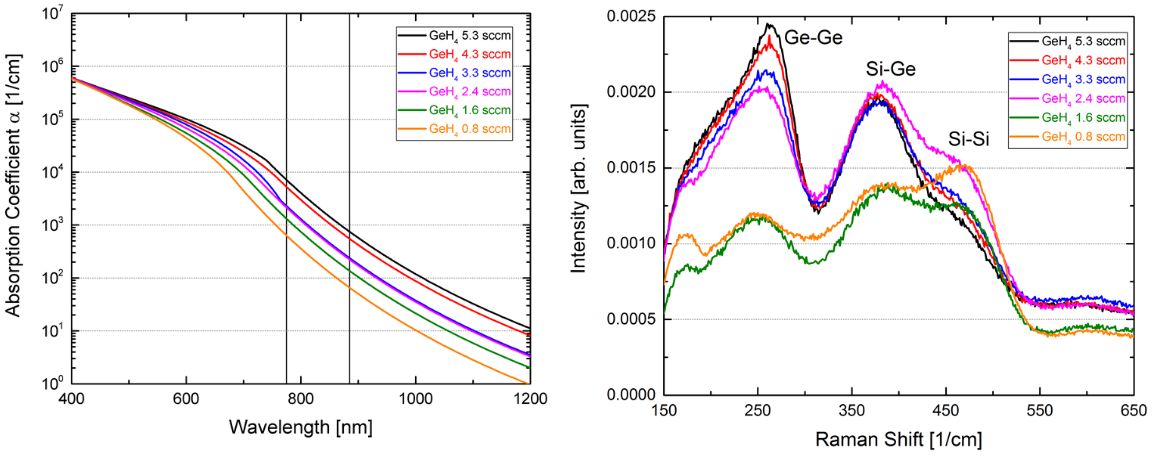

(a) (b)

Figure 4.2: The effect of variation of GeH_4 flow rate of a-SiGe:H film on the absorption coefficient with the two vertical lines indicating the wavelength ranges between 1.4 and 1.6 eV **(a)** and the effect on the Raman spectrum **(b)**.

Figure 4.2a shows that the absorption coefficient increases with an increase of GeH_4 flow rate. Additionally, Figure 4.2b shows that variations of the GeH_4 flow rate can directly influence the optical-, electrical- and material properties due to the fact that it changes the GeH_4 flow rate in the material.

Figure 4.1b displays that increasing the GeH_4 flow rate decreases the bandgap. Ge has a lower bandgap compared to Si, 0.67 eV to respectively 1.11 eV for Si. Addition of GeH_4 would increase the flow rate of Ge in the film and therefore it is likely that the overall bandgap decreases. Moreover, the decrease in bandgap increases the dark conductivity apparently due to the increase in Ge-Ge bonds, see Figure 4.2b.

Figure 4.2b shows a lack of a Raman peak around 512 cm^{-1}, which means the material lacks crystallinity. Therefore, the increase in dark conductivity cannot be caused by an increase of the crystalline phase. The peak at 470 cm^{-1} shows the Si-Si bonds. They tend to increase with decreasing the GeH_4 flow.

Additionally, there is a peak around 380 cm^{-1}, indicating the Si-Ge bonds. Addition of GeH_4 leads to an increase in Si-Ge stretching if the GeH_4 flow rate of 2.4 sccm is taken out of consideration. Therefore, it seems likely that the lower the GeH_4 flow rate, the lower the Si-Ge peaks are. Comparing the Si-Si and Ge-Si bonds, shows that the Si fraction decreases while increasing the GeH_4 flow rate. Another important matter in the graph is the shift in peak around 280 cm^{-1}, which is the Ge-Ge stretching. It indicates that an increase of GeH_4 flow rate increases the peak and more Ge-Ge bonds will be available. More Ge-Ge bonds will be present with respect to the Si-Si bonds. Preferential bonding of Ge-Ge is plausible, because GeH_4 decomposes much faster in the plasma than SiH_4 does [53]. More Ge-bonds therefore indicate a lower bandgap causing a higher absorption coefficient, see Figure 4.2a.

4.2. Flow rate SiH_4

The previous paragraph showed that the GeH_4 flow rate can directly change the optical-, electrical- and material properties. Another parameter to vary is the SiH_4 flow rate. Silane is used as a precursor to elemental silicon. The chemical reactions can be found in Appendix A. The SiH_4 flow rate is varied between 20 and 40 sccm.

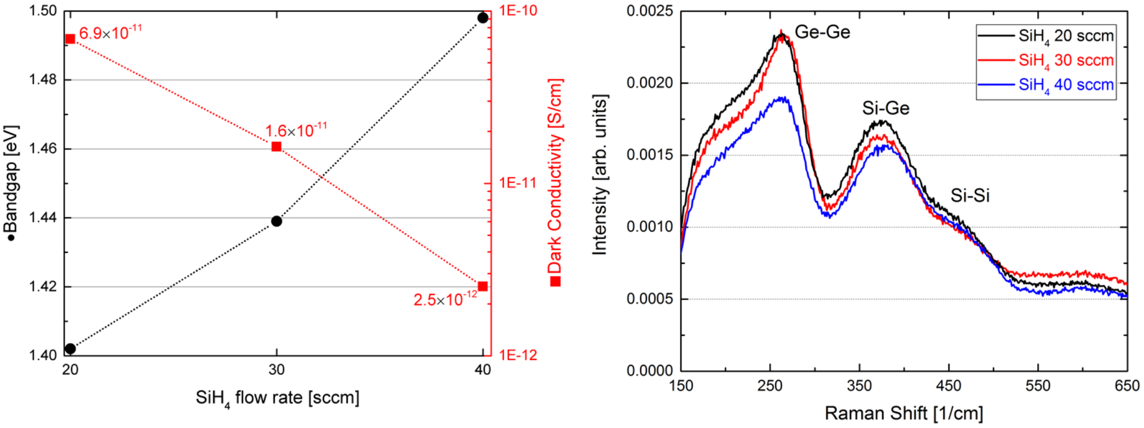

(a) (b)

Figure 4.3: The effect of variation of SiH_4 flow rate of a-SiGe:H film on the bandgap and dark conductivity **(a)** and the effect on the Raman spectrum **(b)**.

Figure 4.3a displays a decrease in dark conductivity of 10^1 S/cm while increasing the SiH_4 flow rate between 20 and 40 sccm. The E_{act} increases accordingly by 200 meV between the highest and lowest used SiH_4 flow rate. Figure 4.3a also shows that an increase of SiH_4 flow rate from 20 to 40 sccm increases the bandgap by 0.1 eV. The lower GeH_4 flow rate in the film decreases the absorption coefficient with increasing SiH_4 flow rate. Moreover, the decrease in dark conductivity is likely related to the decrease in bandgap and increase of defect density, due to the decrease in Ge-Ge bonds at higher SiH_4 flow rate.

Figure 4.3b shows that variation of the the SiH_4 flow rate can indirectly influence the optical-, electrical- and material properties due to the fact that it changes the GeH_4 flow rate in the material.

Figure 4.3b shows the Si-Si bonds at 470 cm^{-1}. They tend to increase with increasing the SiH_4 flow. Additionally, there is a peak around 380 cm^{-1}, indicating the Si-Ge bonds. Addition of SiH_4 indicates a decrease in Si-Ge peaks. Another important peak is around 280 cm^{-1}, which is the Ge-Ge stretching. It indicates that an increase of SiH_4 flow rate decreases the peak and less Ge-Ge bonds will be available [54]. The reasoning behind it is that increasing the SiH_4 flow decreases the GeH_4/SiH_4 ratio. Therefore, less Ge-Ge bonds will be present with respect to the Si-Si bonds, which indicates that more Si-Si bonds are present. This likely indicates a higher bandgap.

4.3. Flow rate H_2

Another parameter to vary to influence the optical-, electrical- and material properties is the H_2 flow rate. The H_2 flow rate is varied between 150 and 200 sccm.

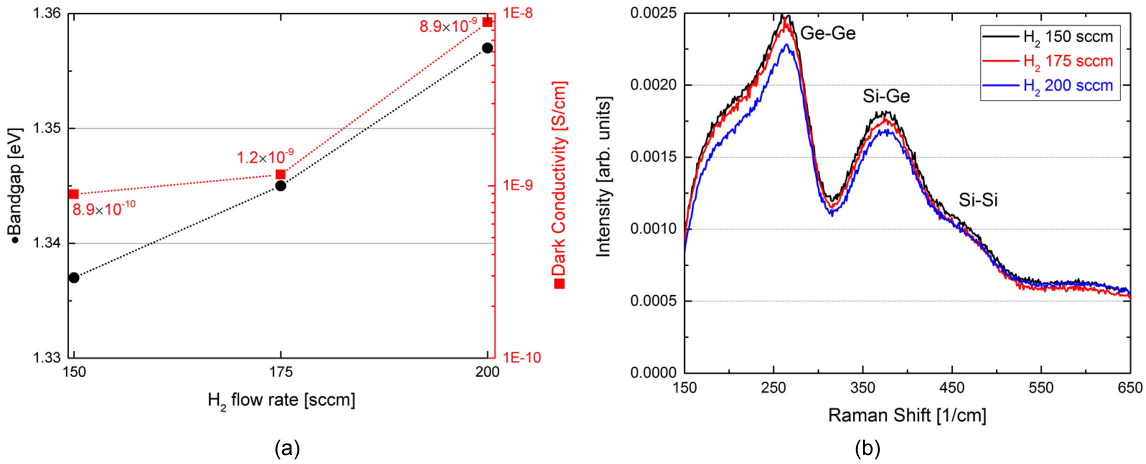

(a) (b)

Figure 4.4: The effect of variation of H_2 flow rate of a-SiGe:H film on the bandgap and dark conductivity **(a)** and the effect on the Raman spectrum **(b)**.

Figure 4.3a displays an increase in dark conductivity of 10^1 S/cm while increasing the H_2 flow rate between 150 and 200 sccm, which is unexpected. The E_{act} decreases accordingly by 200 meV between the lowest and highest used H_2 flow rate. Figure 4.4a also shows an increase of H_2 flow rate from 150 to 200 sccm increases the bandgap by 0.02 eV. The lower GeH_4 flow rate in the film decreases the absorption coefficient slightly with increasing H_2 flow rate. Figure 4.4b shows that variation of the the H_2 flow rate can indirectly influence the optical-, electrical- and material properties due to the fact that it changes the GeH_4 flow rate in the material.

Figure 4.4b shows the Si-Si bonds at 470 cm^{-1}. They tend to fluctuate with increasing the H_2 flow. Therefore, no trend is observed here. Additionally, there is a peak around 380 cm^{-1}, indicating the Si-Ge bonds. Addition of H_2 indicates a decrease in Si-Ge peaks. Therefore, with lower H_2 flow rate more Ge is present in the film, which indicates a lower bandgap. Adopting H_2 in a-SiGe:H thin films is one of the most essential approaches for passivation of dangling bonds [55]. H_2 incorporation reduces the bulk density of defect states by orders of magnitude [56]. Moreover, it widens the bandgap and increases the dark conductivity [57].

Another important peak is around 280 cm^{-1}, which is the Ge-Ge stretching. It indicates that with an increase of the H_2 flow rate the Ge-Ge peak decreases and more Ge is passivated. When the atomic H_2 is sufficient in plasma, a high H-coverage growth surface and local heating lead to a well-relaxed network [58]. Therefore, the increase of H_2 flow rate is showing passivation of Ge dangling bonds, which increases the bandgap.

4.4. Substrate temperature

Another parameter which can likely influence the optical-, electrical- and material properties is the substrate temperature. The substrate temperature is varied between 120 and 210°C.

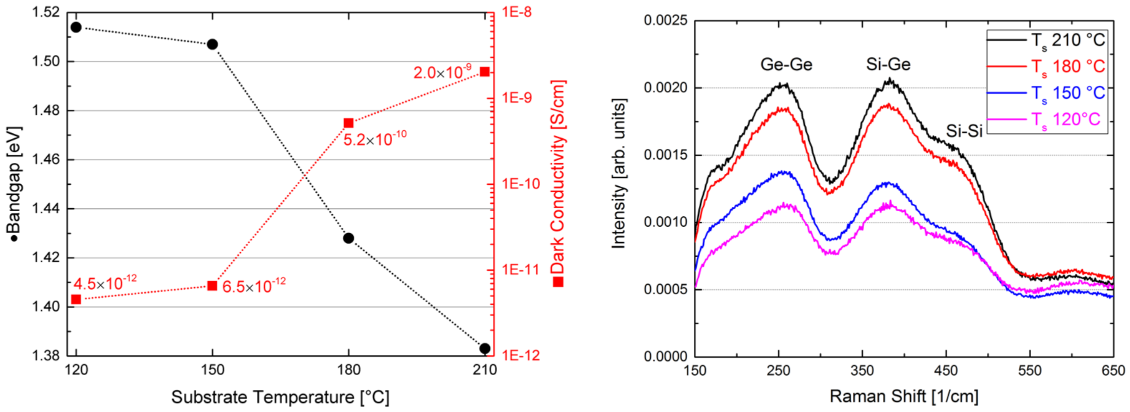

(a) (b)

Figure 4.5: The effect of variation of substrate temperature with a GeH_4 flow rate of 3.3 sccm of a-SiGe:H film on the bandgap and dark conductivity **(a)** and the effect on the Raman spectrum **(b)**.

Figure 4.5a displays an increase in dark conductivity of 10^3 S/cm while increasing the substrate temperature between 120 and 210°C, which is likely related to the decrease in bandgap and increase of defect density. The E_{act} decreases accordingly by 125 meV between the lowest and highest used substrate temperature. Figure 4.5a also shows that with an increase of the substrate temperature from 120 to 210°C the bandgap decreases by 0.14 eV. The higher GeH_4 flow rate in the film increases the absorption coefficient with increasing substrate temperature. Moreover, the decrease in bandgap increases the dark conductivity. Figure 4.5b displays that the change of substrate temperature can indirectly influence the optical-, electrical- and material properties due to the fact that it changes the GeH_4 flow rate in the material.

Figure 4.5b shows the Si-Si bonds at 470 cm^{-1}. They tend to increase with increasing the substrate temperature. Additionally, there is a peak around 380 cm^{-1}, indicating the Si-Ge bonds. An increase in substrate temperature indicates an increase in Si-Ge bonds. Another important peak is around 280 cm^{-1}, which is the Ge-Ge stretching. It indicates that an increase of the substrate temperature increases the peak and more Ge-Ge bonds will be available [54]. However, both the Ge-Ge, Si-Ge and Si-Si bonds are higher at higher substrate temperature, relatively more Ge-Ge bonds will be present with respect to the Si-Si bonds, which lowers the bandgap.

An increase in temperature leads to a continuous decrease of the H_2 content, shown in the Raman peaks between 1800-2200 cm^{-1} in Appendix B. This will decrease the bandgap energy, by increasing the Ge dangling bonds. The increase of substrate temperature will cause a more void rich, so more porous material [59]. A reason for the temperature effect can be due to enhanced H_2 effusion at higher substrate temperatures [5]. Moreover, an increase in temperature decreases the material resistance, which increases the dark conductivity.

4.5. Deposition power

Another important parameter which can influence the optical-, electrical- and material properties is the deposition power. The deposition power is varied between 2 and 8 W.

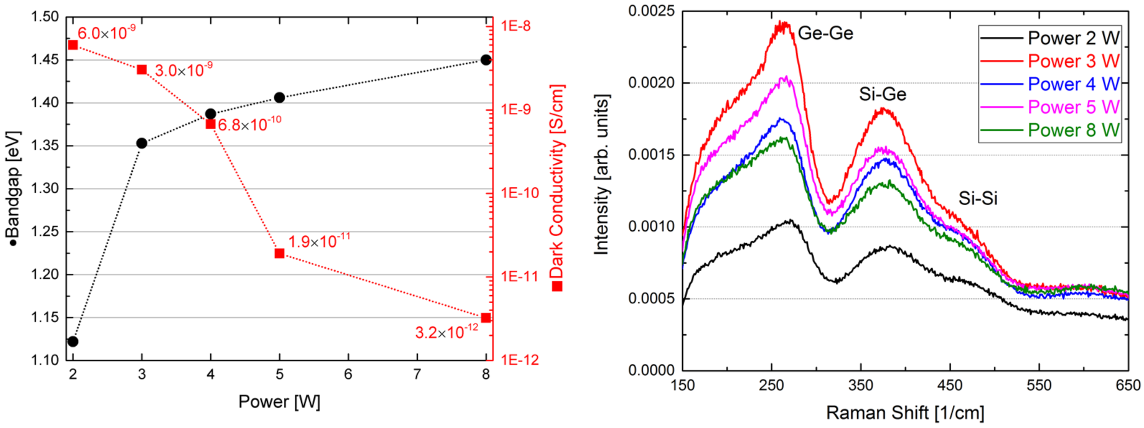

(a) (b)

Figure 4.6: The effect of variation of deposition power with a GeH_4 flow rate of 4.3 sccm of a-SiGe:H film on the bandgap and dark conductivity **(a)** and the effect on the Raman spectrum **(b)**.

Figure 4.6a displays a decrease in dark conductivity of 10^3 S/cm while increasing the deposition power in steps between 2 and 8 W. The E_{act} increases accordingly by 500 meV between the lowest and highest used deposition power. Figure 4.6a also shows that an increase of the deposition power in steps between 2 and 8 W increases the bandgap by 0.3 eV. The lower GeH_4 flow rate in the film decreases the absorption coefficient with increasing deposition power. Figure 4.6b displays that the change of deposition power can indirectly influence the optical-, electrical- and material properties due to the fact that it changes the GeH_4 flow rate in the material.

Figure 4.6b shows the Si-Si bonds at 470 cm^{-1}. They tend to decrease with increasing the deposition power. However, the bandgap shows opposite trend, namely increase of Si-Si bonds, which increases the bandgap. At high RF power more Ge dangling bonds get passivated by the H_2 atoms [40]. This increases the SiH_4/GeH_4 content in the film, which increase the bandgap, and therefore decrease the dark conductivity. At high power particles continuously bombard the film during growth and combining this with an increase of the deposition rate with high power, likely results in physical damage to the material [60]. Therefore, more defects may be incorporated in the intrinsic film at a high growth rate, leading to poor stability. Thus, the increase of power can lead to physical damage, causing a more void rich material [59]. The Raman peak of Si-H bonds at 620 cm^{-1} and the Si-H_2 bonds at 2080 cm^{-1} show that those assumptions are likely to occur, see Appendix B.

Another reason for the increased bandgap while increasing power is the increase of the hydrogen content in the films. This can be seen by the Raman peaks at an intensity of 620 cm^{-1} corresponding to the wagging and rocking modes of Si–H bonds, and the intensity at 1870 cm^{-1} corresponding to that of Ge–H bonds. A gradual increase of the hydrogen content is observed on increasing the plasma power, see Appendix B.

Additionally, there is a peak around 380 cm^{-1}, indicating the Si-Ge bonds. The Si-Ge bonds tend to increase with decreasing power if the 2 W film is not taken into consideration [61]. Another important peak is found around 280 cm^{-1}, which is the Ge-Ge stretching. It is likely that, if the 2 W film is not taken into consideration, with a decrease of the deposition power more Ge-Ge bonds are present in the film, which decreases the bandgap at low deposition power.

4.6. Deposition pressure

The last reported parameter which can likely change the optical-, electrical- and material properties is the deposition pressure. The deposition pressure is varied between 1.6 and 6 mbar.

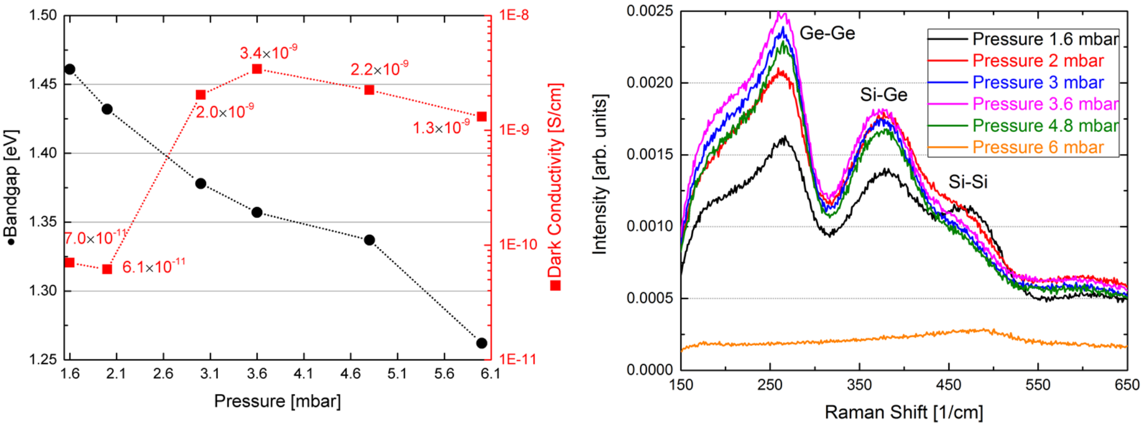

(a) (b)

Figure 4.7: The effect of variation of deposition pressure with a GeH_4 flow rate of 4.3 sccm of a-SiGe:H film on the dark conductivity **(a)** and on the activation energy **(b)**.

Figure 4.7a displays an increase in dark conductivity of 10^2 S/cm while increasing the deposition pressure in steps between 1.6 and 6 mbar. The E_{act} decreases accordingly by 300 meV between the lowest and highest used deposition pressure. Figure 4.7a also shows that with increasing the deposition pressure in steps between 1.6 and 6 mbar the bandgap decreases by 0.2 eV. The higher GeH_4 flow rate in the film increases the absorption coefficient with increasing deposition pressure. Figure 4.7b displays that the change of deposition pressure can indirectly influence the optical-, electrical- and material properties due to the fact that it changes the GeH_4 flow rate in the material.

Figure 4.7b shows the Si-Si bonds at 470 cm^{-1}. They tend to increase with decreasing the deposition pressure. Additionally, there is a peak around 380 cm^{-1}, indicating the Si-Ge bonds. It seems likely that the Si-Ge bonds increase with a decrease in pressure if the 1.6 mbar sample is not taken into consideration [40]. At higher pressures more Si has reacted, which increases the GeH_4/SiH_4 ratio, likely by a decrease in Si radical fraction, and therefore decreases the bandgap [62]. The peaks at 380 and 470 cm $^{-1}$ combined show that more SiH_4 is present in the film at lower pressure and therefore the GeH_4/SiH_4 ratio decreases and accordingly the bandgap increases.

Another important peak is around 280 cm^{-1}, which is the Ge-Ge stretching. It does not show a significant effect, and therefore no clear trend can be observed from this Raman peak. However, the bandgap displays that it is likely that with an increase of pressure more GeH_4 is present in the film and therefore the Ge-Ge bonds increase. This will decrease the bandgap and increase dark conductivity. This is confirmed by the increasing Ge-Ge bonds with respect to the Si-Si bonds. Increasing deposition pressure showed decreased transparency, which leads to decreasing bandgap energy and will lead to decreasing H_2 content due to more Ge dangling bonds, as shown by the increase in Si-H bonding peak at 620 cm^{-1}, see Appendix B.

4.7. Conclusion materials

The influence of different deposition parameters on the optical-, electrical- and material properties is divided in a direct and indirect effect. The flow rate of GeH_4 can directly influence the optical-, electrical- and material properties due to the fact that it directly changes the GeH_4 flow rate in the material. Other deposition parameters, like deposition power, deposition pressure, substrate temperature, H_2 flow rate and SiH_4 flow rate have an indirect effect on the final properties. All different effects of deposition parameters on the dark conductivity, bandgap and absorption coefficient are given by Table 4.2.

Table 4.2: Overview of the deposition parameters influences on material properties.

Parameters	**Dark Conductivity**	**Bandgap**	**Absorption Coefficient**
	[S/cm]	[eV]	[1/cm]
GeH_4/SiH_4	↑↑	↓↓	↑
H_2/SiH_4	↑	↑	↓
Substrate Temperature	↑↑	↓	↑
Deposition Power	↓↓	↑↑	↓
Deposition Pressure	↑↑	↓↓	↑

5

Single Junction Solar Cell

In this chapter an investigation on the a-SiGe:H intrinsic layer of a single junction solar cell is performed. This chapter will answer two research questions, namely (i) which bandgap grading profile in terms of shape, grading region width and absorber thickness should be used in an optimal single junction a-SiGe:H device and (ii) which buffer layer and buffer layer thickness should be used in an optimal single junction a-SiGe:H device.

5.1. Multiple layer investigation

As a starting point a n-i-p single junction solar cell is fabricated by reversing the p-i-n single junction a-SiGe:H solar cell fabricated by the PVMD group [63]. The reference a-SiGe:H solar cell cell has a V_{oc} of 508 mV, a FF of 0.39, a J_{sc} of 9.9 mA/cm^2 and a final efficiency of 2.9%. Therefore significant optimization is needed.

The optimization process is performed on a transparent substrate without a back reflector, due the fact that the a-SiGe:H cell will be used as middle cell in a triple junction device. Each sample consists of 24 cells with an active area of 5 by 5 mm each and the best 3 cells per sample are averaged and used for interpretation in this thesis. Additionally, all flow rates in this chapter are peak flow rates, unless it is stated differently.

5.1.1. Transparent Conductive Oxide

All results of the front and back TCO optimization can be found in Appendix C. It is important to highlight that the FF and V_{oc} are significantly lower for the depositions with AZO as front TCO, compared to ITO. AZO is deposited at high RF power of 400 W, which likely caused the p-layer to be damaged [54]. ITO is the most favorable front TCO due to its electro-optical properties and performance. AZO deposited on a corning glass substrate is used at the back of the device, since it outperformed Asahi substrates both in terms of the V_{oc} and FF [64].

5.1.2. n-layer optimization

Different combinations of n-layers are proposed, namely (i) a n-a-Si/n-SiOx:H bilayer and (ii) a layer in which the oxygen flow is gradually introduced, such that the layer is graded from n-nc-Si to n-SiOx:H, see Appendix C. N-nc-Si has the lowest E_{act} and can provide the best back contact with the TCO, while the high bandgap of n-SiOx is favourable at the n/i interface and in terms of parasitic absorption losses at the back [5].

The layer in which the oxygen flow is gradually introduced, such that the layer is graded from n-nc-Si to n-SiOx:H, provides the best results. It is important to grade the oxygen flow of n-SiOx:H from low to high. In this case a more oxygen rich fraction will be present near the n/i interface. It is likely that this leads to high optical transparency and low parasitic absorption losses [65].

5.1.3. p-layer optimization

Due to the fact that charge carriers generated in the p-layer hardly contribute to the solar cell performance, a wide bandgap material should be used as p-layer [10]. Two extensively researched, but different materials are investigated, namely p-SiC:H and p-SiOx:H.

The optimized p-SiC:H and first round of p-SiOx:H layers can be found in Appendix C. It indicates that p-SiOx:H with a seed layer and a thin p-nc-Si:H contact layer outperforms the optimized p-SiC:H layers. The p-SiOx:H stack consists of a thin i-nc-Si:H seed layer and a very thin p-nc-Si:H contact to ensure good ohmic contact with the front TCO [66].

The single-junction a-SiGe:H solar cell structure, before optimization of the intrinsic layer and addition of buffer layers, is displayed in Figure 5.1.

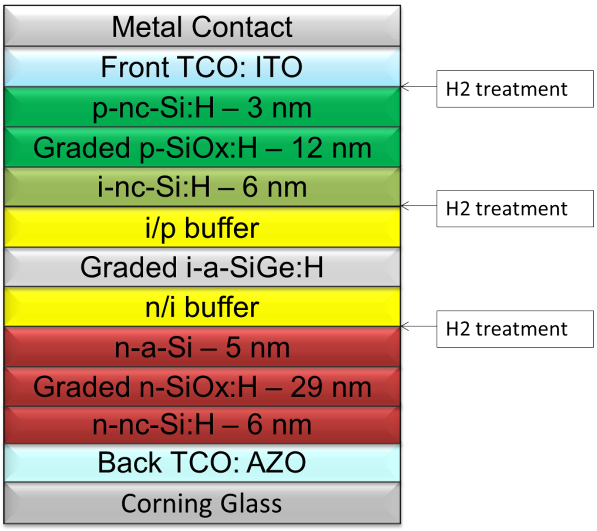

Figure 5.1: Structure of single junction solar cell before intrinsic layer optimization.

Figure 5.1 displays the reference n-i-p solar cell, which is fabricated with Corning glass as substrate, in the following sequence: AZO back TCO 700 nm/ n-nc-Si:H 6 nm/ n-SiOx:H 29 nm/ n-a-Si 5 nm/ i-a-SiGe:H 150 nm/ i-nc-Si:H 6 nm/ p-SiOx:H 12 nm/ p-nc-Si:H 3 nm/ ITO front TCO 75 nm and lastly a metal grid as front contact of 500 nm aluminum.

5.2. Intrinsic layer

In the coming paragraphs the a-SiGe:H intrinsic layer investigation is performed. Firstly, the influence of deposition power variation from 2 to 8 W is tested, which is followed by a deposition pressure series from 2.4 to 6 mbar. Those optimized parameters will be the starting point for the intrinsic layer investigation.

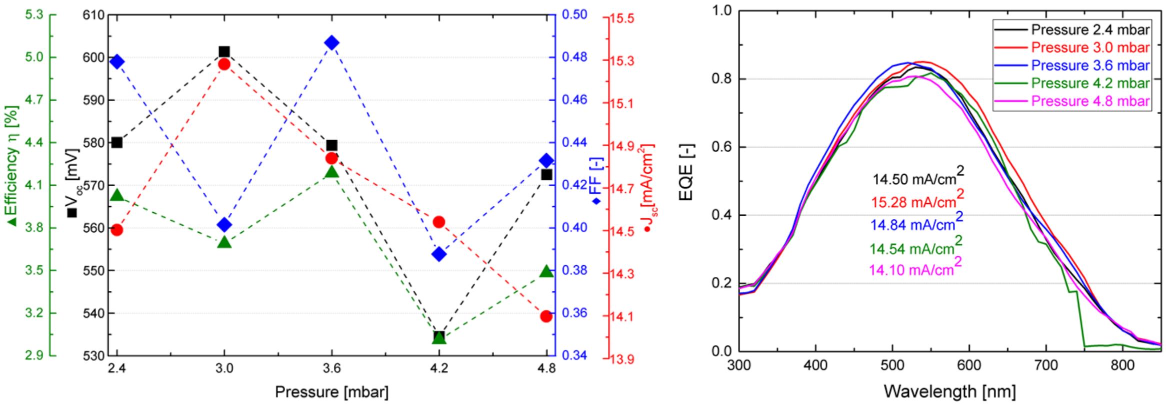

(a) (b)

Figure 5.2: The effect of variations in deposition pressure on solar cell parameters **(a)** and EQE **(b)**.

Figure 5.2a shows that no clear trend is observed with the deposition pressure series. It seems likely that J_{sc} decreases with increasing deposition pressure. However, this is not as expected since the film characterization showed that the bandgap decreases with increasing deposition pressure. The deposition rate decreases with increasing pressure [54], which can indicate that different thickness is deposited. The highest product in terms of V_{oc} and FF is found at a deposition pressure of 3.6 mbar.

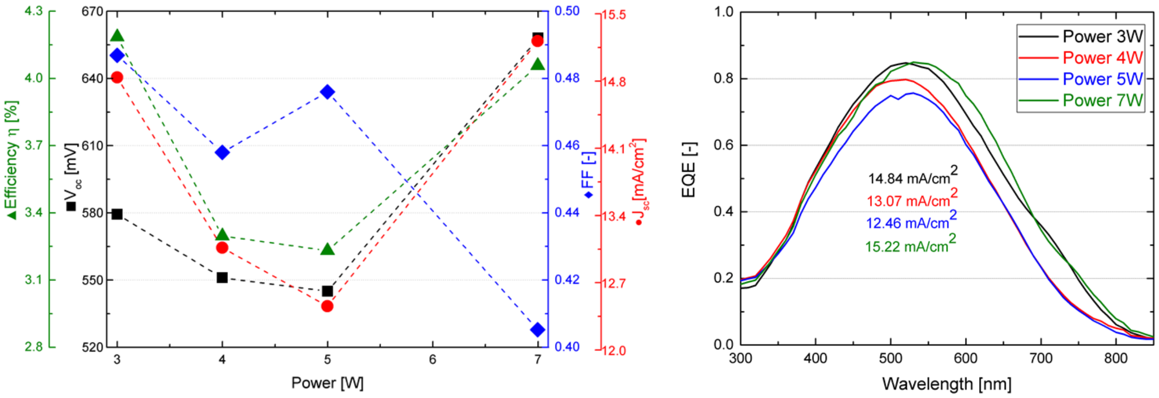

(a) (b)

Figure 5.3: The effect of variations in deposition power on solar cell parameters **(a)** and EQE **(b)**.

Figure 5.3a shows that the highest product in terms of V_{oc} and FF is found at low power of 3 W. Additionally, a poor stability is experienced at high power, likely due to an increase in dangling bonds, resulting in a low FF. This phenomenon is observed due to an increase in Si-H_2 bonds. This can be found in the Raman graph, which shows stability problems, see Appendix B. This is related to an increase in deposition rate at higher deposition power [60]. Therefore, a low deposition power is chosen. The deposition pressure of 3.6 mbar and a deposition power of 3 W will be used for further optimization.

5.2.1. GeH_4 flow rate

The influence of variations in the GeH_4 flow rate is tested by varying the flow rate from 0.8 to 5.3 sccm.

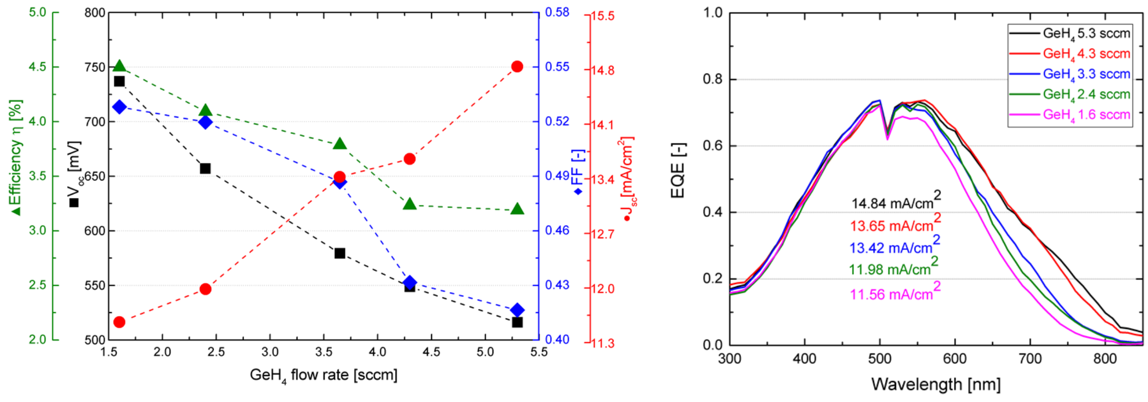

(a) (b)

Figure 5.4: The effect of variation of GeH_4 flow rate on a-SiGe:H solar cell parameters **(a)** and EQE **(b)**.

Figure 5.4a shows that the V_{oc} decreases from 740 to almost 510 mV and that the J_{sc} increases by almost 3.5 mA/cm^2 when the GeH_4 flow rate is increased from 1.6 to 5.3 sccm. This is related to the bandgap decrease of over 0.2 eV observed in the a-SiGe:H films. The characterization of films showed that if the GeH_4 is increased the defect density increases as well. It is likely that the GeH_4 flow cannot be increased to a further level, due to the increased defect density, which causes a decrease in solar cell parameters.

In addition, the FF of the cell decreases when lowering the bandgap, which reflects a higher recombination in the device, due to an increase of R_s from 15.9 to 22.8 Ωm^2. This is a result of the increased dangling bond density in the bulk of the absorber. Figure 5.4b shows that a higher GeH_4 flow rate improves the J_{sc}, due to a lower overall bandgap and extra absorption in the longer wavelengths [67]. The decision is made to further investigate a GeH_4 flow rate of 2.4 sccm, due to the highest product in terms of V_{oc} and FF with a J_{sc} of around 12 mA/cm^2.

Annealing

It has been reported that annealing effects can occur at temperatures above 100°C. Annealing is performed for contact adhesion and growth related stress release. The annealing series started at 130°C for 20 minutes and ended at 190°C for 20 minutes. This annealing experiment is performed for multiple GeH_4 flow rates.

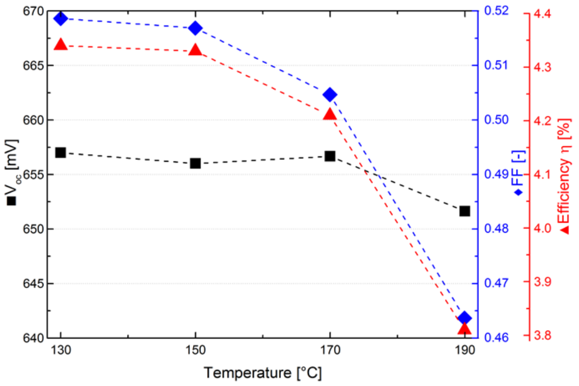

Figure 5.5: Annealing conditions under different temperatures with a GeH_4 flow rate of 2.4 sccm.

However, for an easier overview only a GeH_4 flow rate of 2.4 sccm is displayed in Figure 5.5. Figure 5.5 shows that the reference annealing temperature of 130°C for 30 minutes outperforms the other annealing temperatures. It indicates that low temperature annealing improves the performance of a-SiGe:H. The results from Figure 5.5 are further specified in Table 5.1.

Table 5.1: The effect of annealing series on variation of GeH_4 flow rate for single junction solar cells.

Temperature (°C)	150	170	190	150	170	190	150	170	190
GeH_4 flow rate (sccm)	V_{oc} (%)	V_{oc} (%)	V_{oc} (%)	FF (%)	FF (%)	FF (%)	η (%)	η (%)	η (%)
4.3	-0.1	-0.4	-3.3	-1.5	-2.7	-13.3	-2.0	-2.7	-18.3
3.65	-0.2	-0.3	-1.3	-0.1	-2.5	-12.4	-0.3	-3.2	-16.0
2.4	-0.2	-0.1	-0.8	-0.6	-2.9	-10.8	-0.2	-2.8	-12.2

The results of Table 5.1 indicate the performance relative to the sample annealed at 130°C. The higher the annealing temperature the lower the V_{oc}, FF and η are. Further annealing at higher temperatures will deteriorate the device quality even more. This is both due to a decrease in R_{sh} and an increase in R_s.

Light Induced Degradation

LID tests are performed on single junction solar cells with different GeH_4 flow rates. The cells were first annealed for 90 minutes at 130°C likely for reordering of the defects, since the cells have been exposed to ambient light for several hours.

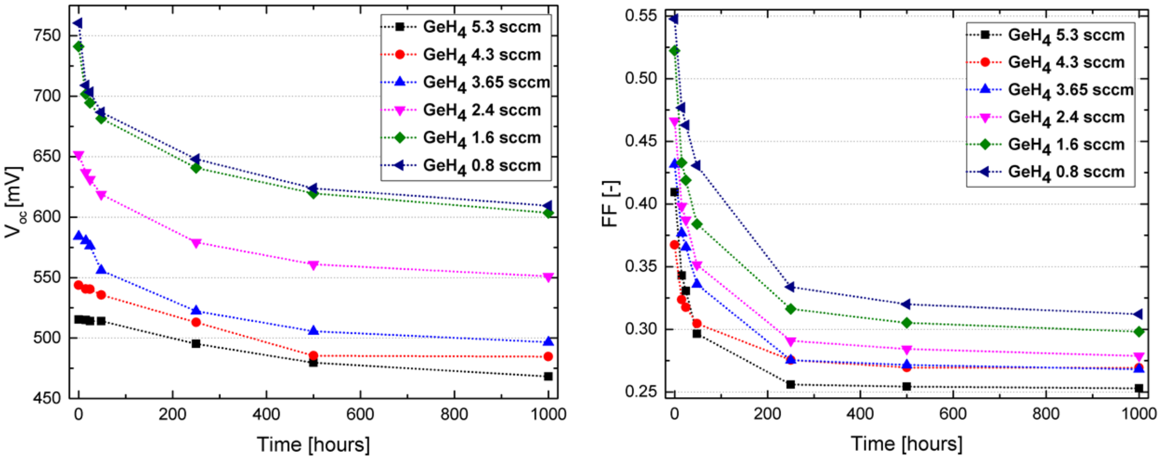

(a) (b)

Figure 5.6: The effect of Light Induced Degradation under different GeH_4 flow rate conditions on V_{oc} **(a)** and the effect on FF **(b)**.

Figure 5.6a represents the LID tests effect on the V_{oc}, where I-V measurements are performed after 15, 24, 48, 250, 500 and 1000 hours. Figure 5.6b shows the LID tests effect on the FF. The significant drop in overall efficiency is mostly related to the decrease in FF. This is related to an increase of R_s and a decrease of R_{sh}, which indicates recombination. Table 5.2 summarizes the results of the LID measurements with respect to the reference cell.

Table 5.2: The effect of LID series of different GeH_4 flow rate single junction solar cells after 1000h in reference to their initial values.

GeH_4	**V_{oc}**	**FF**	**Efficiency**	**R_{sh}**	**R_s**
[sccm]	[V]	[-]	[%]	[Ωm^2]	[Ωm^2]
5.3	-9.1%	-38.2%	-42.3%	-43.6%	0.0%
4.3	-10.9%	-26.7%	-34.6%	-29.3%	10.1%
3.65	-15.0%	-37.9%	-37.7%	-42.9%	11.3%
2.4	-15.5%	-40.2%	-47.6%	-71.1%	10.1%
1.6	-18.6%	-42.9%	-51.1%	-75.6%	23.2%
0.8	-19.9%	-43.0%	-52.2%	-78.0%	5.8%

It is assumed that the J_{sc} does not change significantly over time. Table 5.2 indicates a significant decrease in R_{sh} and an increase in R_s. The contributions to the decrease of R_s can originate from bulk resistance, the contact resistance between the junction and electrodes and the resistance of the electrodes themselves [4]. Moreover, R_s affects the FF and is caused by interface/bulk phenomena. The decrease in R_{sh} mostly happens if the effective resistance of the solar cell is high [4], which decreases the V_{oc}.

Table 5.2 displays an almost linear decrease in both FF and V_{oc} with decreasing GeH_4 flow rate. The biggest drop in FF happens in the first 15 hours, effectively around 15%, depending on the GeH_4 flow rate. After 1000h of light soaking the deterioration stabilizes and V_{oc} was measured to show a relative degradation of only 0.01-0.02% per hour, while the FF drops 0.04% per hour. Therefore, solar cells with a higher GeH_4 flow rate suffer less from LID compared to cells with a lower GeH_4 flow rate. Detailed tables can be found in Appendix D.

5.2.2. Intrinsic layer thickness

Variation of the absorber thickness can affect the amount of carriers being collected [4]. Therefore, a trade-off between collection of photogenerated charge carriers (V_{oc}) and absorption of photons (J_{sc}) should be considered.

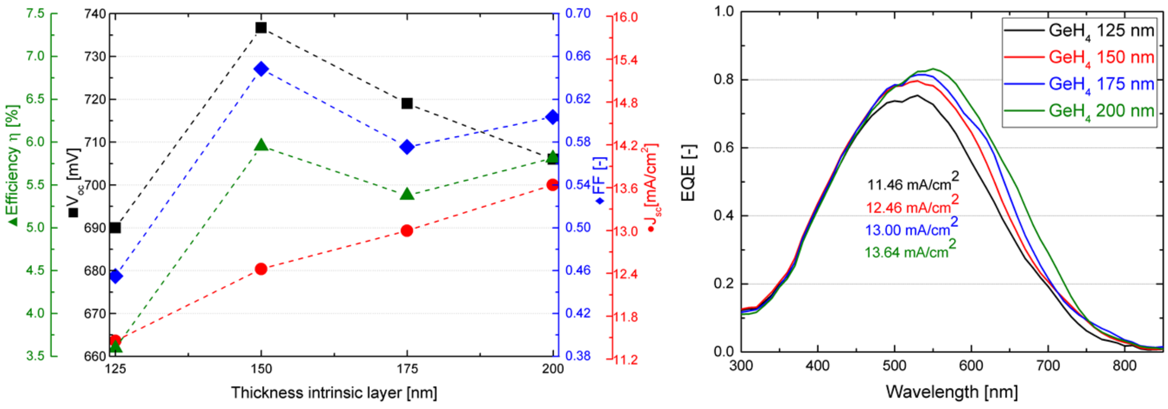

(a) (b)

Figure 5.7: The effect of intrinsic layer thickness variations in the GeH_4 flow rate of 2.4 sccm including grading and buffers on a-SiGe:H solar cell parameters **(a)** and EQE **(b)**.

Figure 5.7a shows the device properties as a function of intrinsic layer thickness. At a thin layer of 125 nm collection seems to be inefficient. The EQE is 1 mA/cm^2 lower compared to the 150 nm thickness. However, due to the fact that the R_s is in the same range as the other thickness, it might be a processing error. The R_{sh} of 714.4 Ωm^2 is significantly lower than the R_{sh} of 5093.7 Ωm^2 at 150 nm. The low R_{sh} explains the low V_{oc}. Moreover, the bulk recombination causes the decrease in FF, mostly dominated by the decrease in R_{sh}.

A thickness of 150 nm generates a V_{oc} of 736.67 mV, a FF of 0.65, a J_{sc} of 12.5 mA/cm^2 and an efficiency of 5.95%. Moreover, the 150 nm sample shows a homogeneous deposition. However, after 150 nm, due to addition of GeH_4 in the layer the V_{oc} decreases, the J_{sc} increases, see Figure 5.7b. The FF decreases due to an increase in R_s from 13.8 to 16.3 Ωm^2. This likely leads to more bulk recombination, which weakens the electric field. Therefore, an intrinsic layer thickness of 150 nm will be used.

5.2.3. Grading shape

Some major challenges in developing a-SiGe:H solar cells are the defective interfaces between the a-SiGe:H absorber and the doped layers. The n/i and i/p interfaces can contain a considerable amount of defects due to sharp changes in material composition [68]. In order to optimize the performance of solar cells, grading of the intrinsic layer by variations in the GeH_4 flow rate near the more sensitive regions, namely the n/i and i/p interfaces can be an interesting option [69]. Literature suggests different types of bandgap grading, such as E-, U- and V-shape.

The aim of the V-shape is to improve the carrier collection inside the i-layer. It moves the position of the minimum bandgap away from the i/p junction [70]. The U-shape can replace the low bandgap material, by an increase in average GeH_4 flow rate, for a higher bandgap material. This can reduce the recombination at the n/i and i/p interfaces. Finally, the E-shape aims to combine the advantages of both the V- and U-shape [54]. These different functionalities per shape can generate design flexibility of the absorber layer.

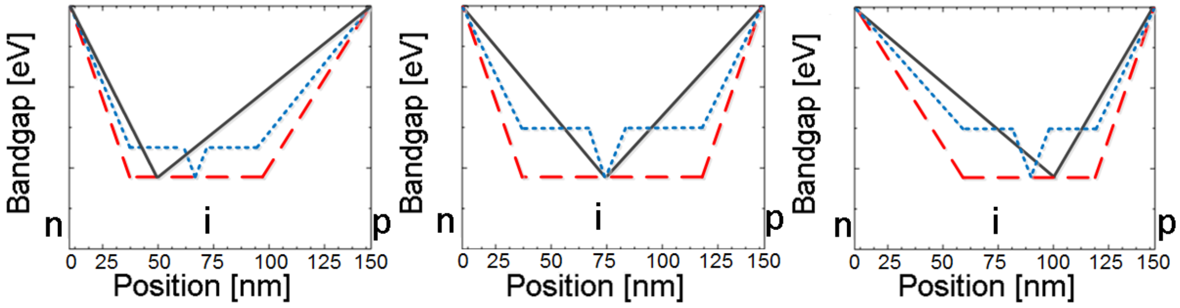

(a) (b) (c)

Figure 5.8: Different E- (red), U- (blue) and V-shape (black) grading structures.

Figure 5.8 displays the schematic overview of the grading options in terms of shape and bandgap. Three different profiling schemes are proposed for the different shapes, namely (a) a small n/i grading width, (b) a large i/i grading width and (c) a large n/i grading width. The different shapes are shown and described in the coming paragraphs. This is followed by an extensive comparison between the shapes.

V-Shape

Firstly, the V-shape will be discussed.

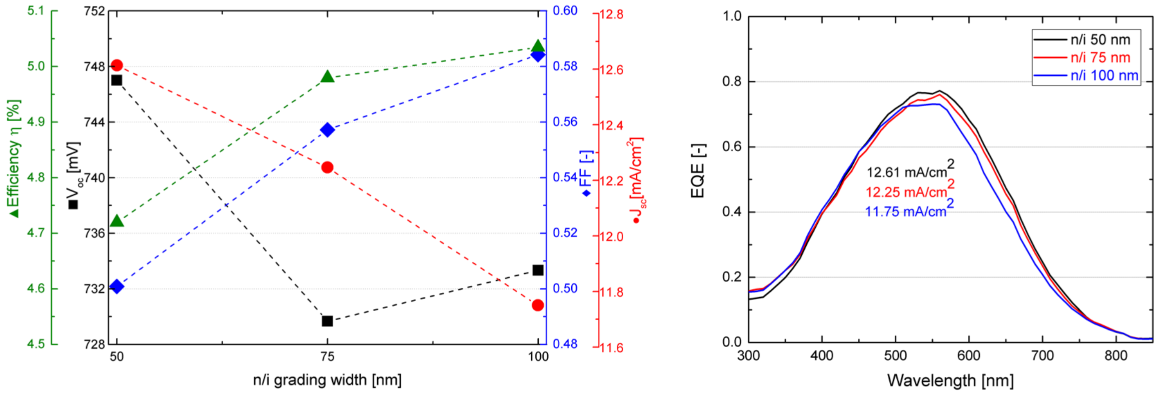

(a) (b)

Figure 5.9: The effect of variations in grading of the V-shape with a GeH_4 flow rate of 2.4 sccm on a-SiGe:H solar cell parameters **(a)** and EQE **(b)**.

Figure 5.9a shows that an increase of the n/i grading width improves the FF from 0.50 to 0.58. However, the V_{oc} is decreased from 747 to 734 mV. Additionally, Figure 5.9b shows that the J_{sc} decreases from 12.6 to 11.7 mA/cm^2, due to decrease of absorption in longer wavelengths.

U-Shape

Secondly, the U-shape will be discussed.

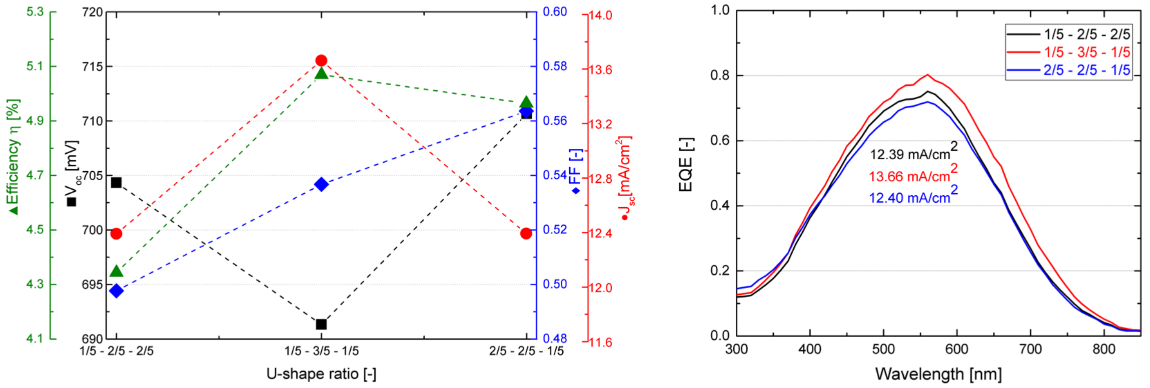

(a) (b)

Figure 5.10: The effect of variations in grading of the U-shape with a GeH_4 flow rate of 2.4 sccm on a-SiGe:H solar cell parameters **(a)** and EQE **(b)**.

Figure 5.10a shows that an increase of the n/i width improves the FF from 0.50 to 0.56. The V_{oc} is the lowest for the U-shape with the largest i-i width, namely 15 mV lower. Additionally, Figure 5.10b shows that the J_{sc} increases for the largest i-i width from 12.4 to 13.7 mA/cm^2, due to increase of absorption in longer wavelengths, by lowering the overall bandgap.

E-Shape

Finally, the E-shape will be discussed.

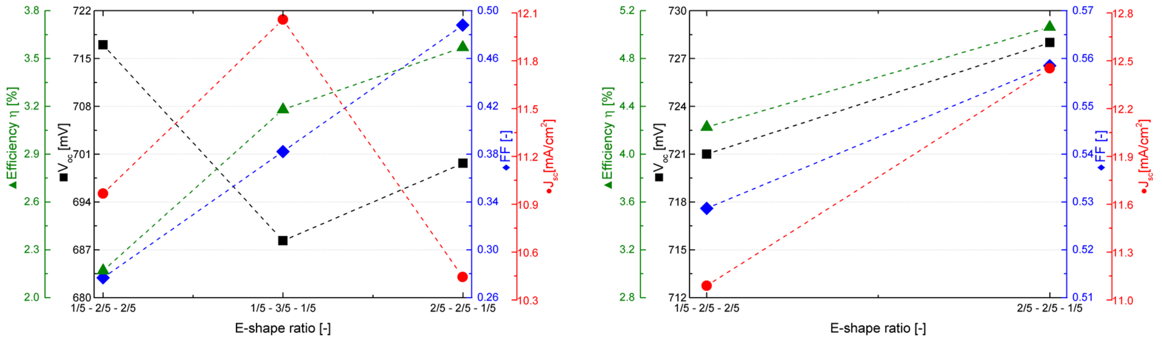

(a) (b)

Figure 5.11: The effect of variations in grading of the E-shape with a GeH_4 flow rate from 2 to 2.4 sccm on a-SiGe:H solar cell parameters **(a)** and on a-SiGe:H solar cell parameters with a GeH_4 flow rate from 0 to 2.4 sccm **(b)**.

Figure 5.11a shows that an increase of the n/i width improves the FF from 0.28 to 0.5. However, the V_{oc} is the lowest for the E-shape with the largest i-i width, namely 25 mV lower. Additionally, Figure 5.11b shows that the J_{sc} increases for a large n/i grading width from 11.0 to 12.4 mA/cm^2, due to increase of absorption in both short and long wavelengths. The EQE graph can be found in Appendix F. The E-shape with the thick i-i grading was shunted in multiple experiments, but it is likely that it will give a higher J_{sc} than the two other E-shapes, due to an overall lower bandgap.

Similarities Shapes

The three different shapes show similar behaviour in terms of FF. The wider the n/i grading the higher the FF. The wide n/i grading moves the position of the minimum bandgap closer to the i/p junction. The increase of n/i grading width likely decreased the recombination, due to a higher overall bandgap, and also strengthened the built-in electric field in the absorber [68]. Additionally, the R_s slightly increases, while the R_{sh} also increases. It is likely that the increase in R_{sh} outweighs the decrease in R_s.

The next comparison is the increase in J_{sc} with the thick i-i plateau. The higher average GeH_4 flow rate reduces the bandgap. More GeH_4 will be present in the layer, which will increase the absorption in the longer wavelength region. However, due to a higher GeH_4 flow rate all shapes suffer from suppression of the V_{oc}.

The deeper back grading at the i/p interface (small n/i grading) decreases the charged defect state density near the i/p interface, leading to a higher internal electric field [70]. This improves the V_{oc}, by a reduction in the recombination process in this region, due a significant increase in R_{sh} for all different shapes. Therefore, the V_{oc} is in all shapes the highest at the small n/i grading.

Dissimilarities Shapes

The aim of the V-shape is to avoid defect states in the middle and rear parts of the i-layer in order to improve the electric field (carrier collection) inside the i-layer. This moves the position of the minimum bandgap away from the i/p junction. To decrease the density of charged defect states in the bulk of the intrinsic a-SiGe:H layer, the V-shape can replace the low bandgap material, which is related to high defect density, for a higher bandgap material, which is related to a lower defect density [70]. The U-shape grading of the i-layer can lead to a better performance of the cell, by reducing the recombination at the i/p and n/i interfaces. The aim of the E-shape is to keep this advantage of the V-shape, while enhancing the generation rate [71]. The E-shape grading profile increases the electric field in the bulk by reducing the charged defect states and the recombination losses and generates more current due to an average lower bandgap compared to the U-shape [54].

The first grading shape has the small n/i width, see Figure 5.8a. The V-shape has the highest V_{oc}. It is 40 mV higher than the U-shape and 25 mV higher than the E-shape. This is due to an average lower amount of GeH_4 flow rate and therefore a higher bandgap. The R_{sh} of the V-shape is 2759.3 Ωm^2, while the U-shape has the lowest R_{sh} of 2507.4 Ωm^2 and therefore the lowest V_{oc}. This is due to the fact that more GeH_4 is alloyed in the U-shape and therefore the bandgap is lower. If the n/i grading is minimized, the highest V_{oc} is reached. The defective i/p interface is likely the dominant junction for the V_{oc}. The J_{sc} of the U-shape is significantly higher than for E-shape, namely 1.3 mA/cm^2, due to a lower bandgap of around 0.05-0.1 eV.

The highest FF can be found for the E-shape due to lower R_s of 12.9 Ωm^2 compared to R_s of the V-shape 13.8 Ωm^2. The position of the minimum bandgap is closer to the i/p junction for the V-shape, which decreases the FF. The highest efficiency of 4.7% is found at the V-shape. This is 0.5 % higher than both the U- and E-shape due to the significantly higher V_{oc} and comparable FF.

The next grading shape has the widest i-i plateau for the U- and E-shape, while the V-shape has exactly the same n/i as i/p grading width, see Figure 5.8b. The peak GeH_4 flow rate for the E- and V-shape happens at the same intrinsic layer thickness position. The V_{oc} is the highest for the V-shape, around 40 mV higher than the U- and E-shape. This is due a higher bandgap of the V-shape by the lower overall GeH_4 flow rate. Additionally, the R_{sh} is twice as high for the V-shape compared to other shapes. Therefore, the J_{sc} is 1.4 mA/cm^2 higher for the U-shape compared to the V-shape, due to lower bandgap and higher absorption coefficient.

The FF of the V-shape is 0.02 higher than for the U-shape. This is due to the position shift away from the defective i/p interface. Moreover, the i/n grading for the V-shape is wider compared to the U-shape. Recombination in the bulk of the i-layer can reduce the FF [54] and therefore the FF is lower for the U-shape compared to the V-shape.

Finally, the wide i/n grading is discussed for the different shapes, see Figure 5.8c. The V_{oc} of the V-shape and E-shape are both around 20 mV higher than for the U-shape. The R_{sh} of the V-shape is 4133.8 Ωm^2, which is higher than the R_{sh} of 2919.3 Ωm^2 for the U-shape. This is related to a higher bandgap for the V-shape. However, the E- and V-shape show almost similar V_{oc} with a difference of 5 mV. Due to the difference in bandgap of around 0.05 eV the difference in V_{oc} was expected to be bigger. The decrease of this difference is caused by the peak GeH_4 flow rate of the V-shape, which position is around 15 nm closer to the i/p interface.

The FF of the V-shape is 0.02 higher than for the E- and U-shape. One of the reasons is due to the position shift away from the defective i/p interface. Additionally, the R_s is around 1 Ωm^2 smaller for the V-shape compared to the E-shape. Moreover, an average higher GeH_4 flow rate decreases the FF, due to a higher defect density at higher GeH_4 flow rate.

The J_{sc} is around 0.6 mA/cm^2 lower for the V-shape compared to the U- and E-shape due to a higher bandgap, which lowers the absorption in long wavelengths. However, in this grading width scheme the difference in J_{sc} is smaller than in the other two grading schemes, due to relative suppression of the Ge amount alloyed due to long i/n grading and a smaller i-i plateau for the U- and E-shape.

Due to the highest product in terms of V_{oc} and FF, mostly dictated by the significant increase in FF, by reducing the recombination at the i/p and n/i interfaces, the decision is made to continue with the V-, U- and E-shape with the largest n/i grading width.

All top performers per shape are summarized in Table 5.3.

Table 5.3: The comparison between best performing V-, U- and E-shape in single junction solar cells with an initial GeH_4 flow rate of 2.4 sccm.

Shape	**Efficiency**	$\mathbf{V_{oc}}$	**FF**	$\mathbf{J_{sc}}$	$\mathbf{R_s}$	$\mathbf{R_{sh}}$
	[%]	[mV]	[-]	[mA/cm^2]	[Ωm^2]	[Ωm^2]
V-shape	5.03	733	0.58	11.75	13.95	4133.82
U-shape	4.96	710	0.56	12.39	13.81	2919.35
E-shape	5.06	728	0.56	12.45	14.91	3123.65

Table 5.3 shows that the highest efficiency can be reached while using the E-shape. However, the V_{oc} and FF are the highest for the V-shape, followed by the E-shape. The J_{sc} is significantly lower for the V-shape compared to the other shapes. However, the enhancement in carrier collection could not compensate the loss of carriers for the U- and E-shape [54].

The E-shape will therefore not combine the advantages of both shapes. Previous research showed that by using V-shape instead of U-shape the V_{oc} and FF will enhance, while it suffers from a loss in J_{sc} due to reduction of amount of Ge alloyed. The same is observed in the experiment. Based on the high product in terms of V_{oc} and FF, the V-shape will be used for further investigation. The best V-shape has a V_{oc} equal to 733 mV, a FF of 0.58, a J_{sc} of 11.8 mA/cm^2 and an efficiency of 5.03%.

5.2.4. Buffer layers

Buffer layers are part of an iterative process. Multiple structures are possible, from single to double buffers on both n/i and i/p interface.

Buffer layers play the role of controlling the quality of the n/i and i/p interface in order to increase both the V_{oc} and the FF. They can have several different effects, namely: (i) reduction of interface recombination, (ii) relaxation of the bandgap discontinuity at the interface, (iii) prevention of excessive boron diffusion from the p-layer into the i-layer, (iv) prevention of back-diffusion of photogenerated electrons, (v) spreading of the electric field into the i-layer near the i/p interface and (vi) prevention of recombination by spatially separating photogenerated electrons from holes [72].

Different buffers are used, namely high bandgap i-a-SiGe:H, high bandgap i-a-Si and i-SiOx:H. High bandgap i-a-Si and i-a-SiGe:H are used to extend the high bandgap at the i/p and n/i interfaces between the narrow band gap i-a-SiGe:H and wide bandgap p-SiOx/n-SiOx. The i-SiOx:H buffer can increase the oxygen which increases the optical transparency, reduces the refractive index and lastly increases the bandgap [73]. Figure 5.12 shows the depositions of i-a-Si, i-SiOx:H and high bandgap i-a-SiGe:H buffers on both the n/i and i/p interface.

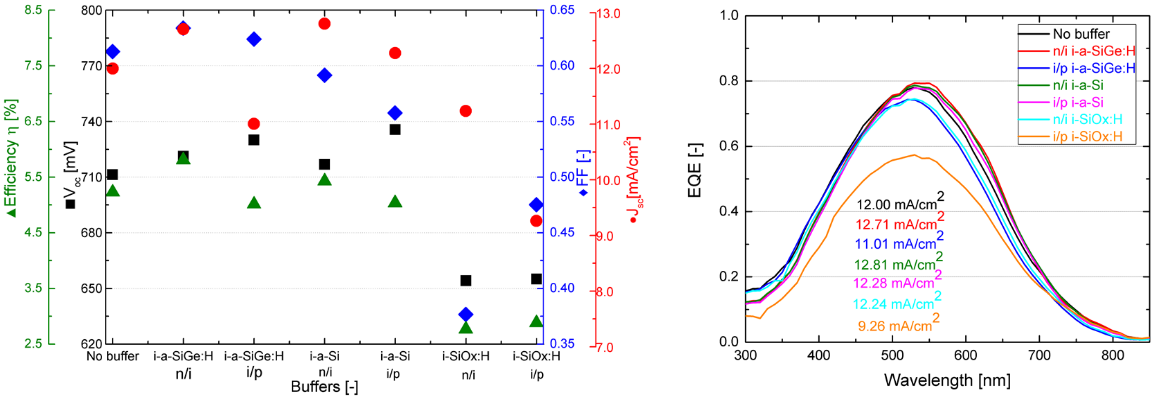

(a) (b)

Figure 5.12: The effect of different n/i and i/p buffers with a V-shape GeH_4 flow rate of 2.4 sccm on a-SiGe:H solar cell parameters **(a)** and EQE **(b)**.

Figure 5.12a indicates that the use of an i-SiOx:H buffer layer, with a bandgap of 2.0 eV, does not improve the electrical properties of the solar cell. The IV curves of those n/i and i/p i-SiOx:H buffers are S-shaped. This indicates at some possible barriers, which can be caused by for example imbalanced mobilities and likely leads to a damaged cell. Additionally, n/i and i/p i-a-Si and i-a-SiGe:H show higher FF and V_{oc} compared to i-SiOx:H. Due to the high product in terms of V_{oc} and FF the n/i and i/p i-a-SiGe:H will be further investigated. Moreover, n/i i-a-Si will also be further investigated due to the relatively high FF, while the i-SiOx:H buffer is eliminated.

i/p i-a-SiGe:H buffer thickness

The first buffer is the i/p i-a-SiGe:H. The thickness of the i/p i-a-SiGe:H buffer is varied between 0 and 11 nm.

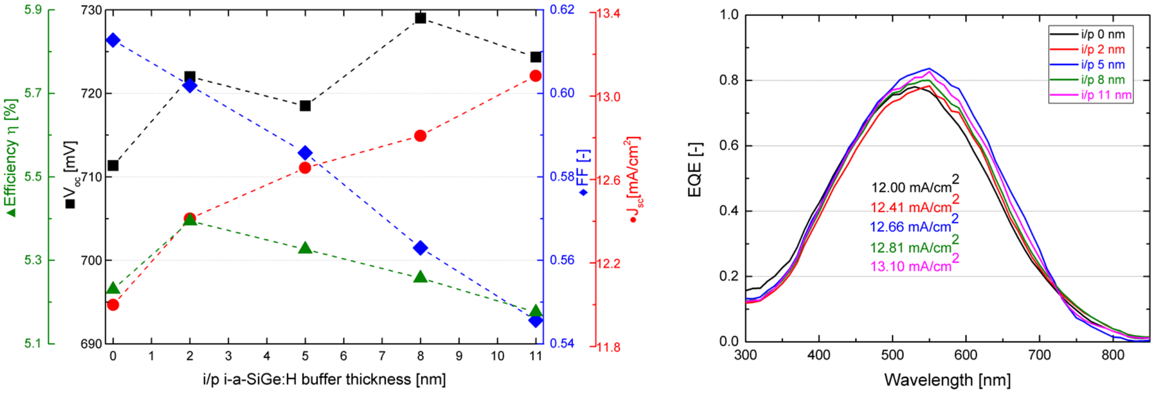

(a) (b)

Figure 5.13: The effect of different i/p i-a-SiGe:H buffer thickness with a V-shape GeH_4 flow rate of 2.4 sccm on a-SiGe:H solar cell parameters **(a)** and EQE **(b)**.

Figure 5.13a shows that an increase of the i/p i-a-SiGe:H buffer thickness decreases the FF from 0.61 to 0.55. However, the V_{oc} is slightly improved from 710 to 725 mV. Additionally, Figure 5.13b shows that the J_{sc} increases from 12.0 to 13.1 mA/cm^2, due to an increase of absorption in the longer wavelengths.

n/i i-a-SiGe:H buffer thickness

The second buffer is the n/i i-a-SiGe:H. The thickness of the n/i i-a-SiGe:H buffer is varied between 0 and 8 nm.

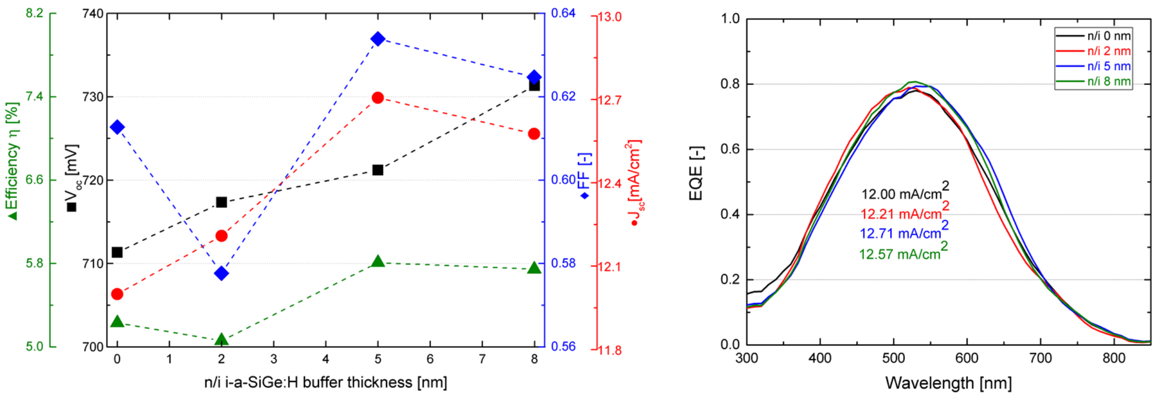

(a) (b)

Figure 5.14: The effect of different n/i i-a-SiGe:H buffer thickness with a V-shape GeH_4 flow rate of 2.4 sccm on a-SiGe:H solar cell parameters **(a)** and EQE **(b)**.

Figure 5.14a shows that an increase of the n/i i-a-SiGe:H buffer thickness improves the FF after 2 nm from 0.58 to 0.62. The V_{oc} is improved from 710 to 730 mV between 0 and 8 nm. Additionally, Figure 5.14b shows that the J_{sc} increases from 12.0 to 12.7 mA/cm^2 between 0 and 5 nm, due to an increase of absorption in longer wavelengths. However, after 5 nm a slight drop is observed in J_{sc}.

n/i i-a-SiGe:H and i/p i-a-SiGe:H buffer thickness

The previous results for both n/i i-a-SiGe:H and i/p buffers i-a-SiGe:H are combined to compare if the two support each other. A thicker i/p i-a-SiGe:H buffer decreases the FF, while slightly increasing the V_{oc} and J_{sc}. Moreover, a thicker n/i i-a-SiGe:H buffer increased the FF and the V_{oc}. The 5 nm i/p i-a-SiGe:H buffer is chosen as standard and the n/i i-a-SiGe:H buffer thickness is varied between 0 and 8 nm.

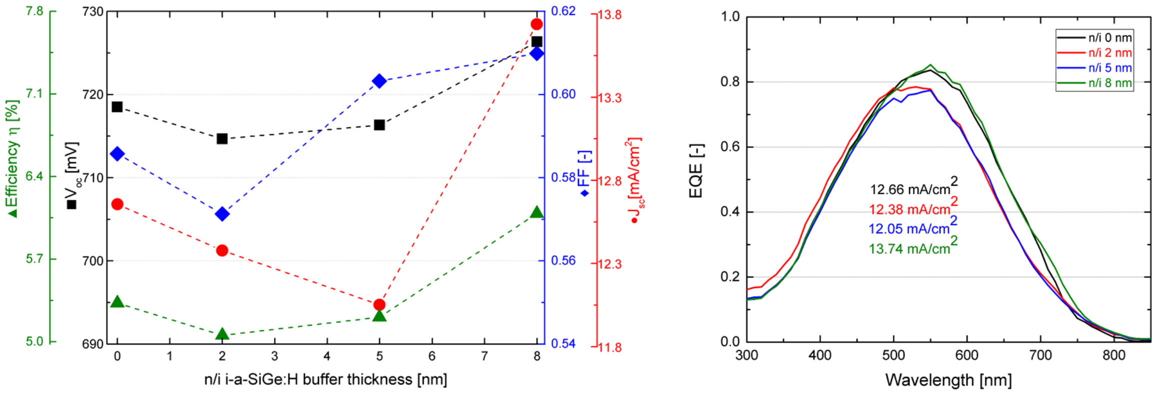

(a) (b)

Figure 5.15: The effect of different n/i i-a-SiGe:H buffer thickness with 5 nm i/p i-a-SiGe:H buffer with a V-shape GeH_4 flow rate of 2.4 sccm on a-SiGe:H solar cell parameters **(a)** and EQE **(b)**.

Figure 5.15a shows that an increase of the n/i i-a-SiGe:H buffer thickness improves the FF after 2 nm from 0.57 to 0.61. The V_{oc} decreases between 0 and 5 nm, but shows a slight increase from 718 to 725 mV after 5 nm. Additionally, Figure 5.15b shows that the J_{sc}

decreases between 0 and 5 nm, but provides an increase from 12.1 to 13.7 mA/cm^2 between 5 and 8 nm, due to an increase of absorption in longer wavelengths.

n/i a-Si, n/i i-a-SiGe:H and i/p i-a-SiGe:H combinations

The n/i i-a-Si buffer gave a relatively high product in terms of V_{oc} and FF and therefore, the 3.2 nm n/i i-a-Si buffer is added. In this test n/i i-a-Si and n/i i-a-SiGe:H buffers are combined. Extra tests are performed with combining the double n/i buffers with an addition of i/p i-a-SiGe:H buffer.

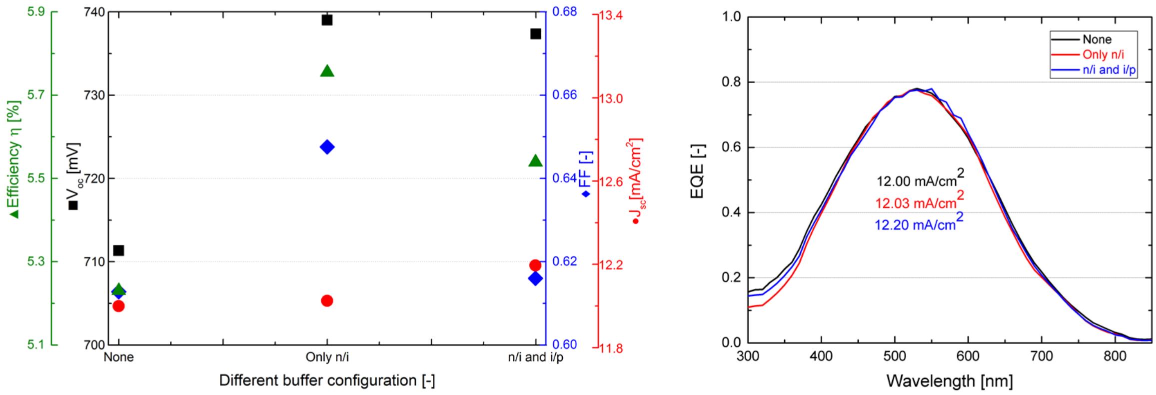

(a) (b)

Figure 5.16: The effect of different buffer configurations with a 3.2 nm n/i i-a-Si buffer, a 5 nm n/i i-a-SiGe:H buffer, and a 5 nm i/p i-a-SiGe:H buffer with a V-shape GeH$_4$ flow rate of 2.4 sccm on a-SiGe:H solar cell parameters **(a)** and EQE **(b)**.

Figure 5.16a shows that an addition of 3.2 nm n/i i-a-Si buffer and 5 nm i/n i-a-SiGe:H buffer compared to no buffers improves the FF from 0.61 to 0.65. The V_{oc} is improved from 710 to 740 mV. The addition of an extra 5 nm i/p i-a-SiGe:H shows a slight decrease in V_{oc} from 740 to 737 mV. Additionally, the 5 nm i/p i-a-SiGe:H addition shows a decrease in FF from 0.65 to 0.62.

Moreover, Figure 5.16b shows that the J_{sc} slightly increases from 12.0 to 12.2 mA/cm^2 with addition of 5 nm i/p i-a-SiGe:H buffer, due to an increase of absorption in longer wavelengths compared to no buffers and without addition of 5 nm i/p i-a-SiGe:H.

Comparison buffers

The first buffer is the i/p i-a-SiGe:H. An increase in thickness of the i/p i-a-SiGe:H buffer indicates two opposite effects, namely an increase in J_{sc}, while the FF decreases. The p-layer is the first layer which is exposed to light and therefore increasing the buffer thickness can act as a potential charge barrier and likely blocks the collection. Another possible explanation of the lowered FF could be the decreased hole tunneling probability through the i/p interface from the reduced potential gradient due to bandgap discontinuity and a mismatch originating from a thicker i/p interface [73]. This increases the R_s from 11.6 to 14.8 Ωm^2. The fluctuations in V_{oc} are likely to be dictated by the fluctuation of R_{sh}.

The EQE measurements in Figure 5.13b show that the thicker i/p i-a-SiGe:H buffer gradually improves the J_{sc}. This is as expected, because more GeH$_4$ is added on the i/p interface, which decreases the bandgap, and therefore more absorption in longer wavelength range can happen.

The second buffer is the n/i i-a-SiGe:H. The addition of high bandgap n/i i-a-SiGe:H should act as a graded interface between the i-layer and the n-a-Si layer. A thicker n/i i-a-SiGe:H buffer increases the V_{oc}, due to an increase in R_{sh} from 2760 to 4512 Ωm^2. The increased FF is related to the decrease in R_s from 18.7 to 11.7 Ωm^2 between 2 and 8 nm.

The addition of a n/i i-a-SiGe:H buffer likely improves the electron collection at the back of the cell. It increases the collection in longer wavelengths, as shown by Figure 5.14b. It is likely that the n/i i-a-SiGe:H buffer lowers the n/i interface potential barrier and can reduce the conduction band discontinuity. This will promote the electron collection, which is one of the key factors for enhancing cell parameters, especially the FF [74].

However, after 5 nm the FF and J_{sc} both slightly drop. A thicker buffer layer can make the travelling distance for electrons larger and therefore less electrons will be collected at the n side, as observed by the lower J_{sc}. The J_{sc} was expected to be higher for 8 nm n/i i-a-SiGe:H buffer, however the thicker layer likely acts as a barrier in this case.

The third buffer is a combination of a n/i i-a-SiGe:H and i/p i-a-SiGe:H. The FF increases if the n/i i-a-SiGe:H thickness increases. This is due to the fact that less recombination occurs at the n/i interface, due to a higher bandgap, displayed by a decrease in R_s from 16.6 to 12.2 Ωm^2.

Compared to the n/i i-a-SiGe:H buffer, combining the n/i and i/p i-a-SiGe:H buffer clearly shows around the same V_{oc}. The V_{oc} is slightly increased for both at a thicker n/i i-a-SiGe:H buffer. However, the FF is lower (maximum of 0.63 versus 0.61). At a thickness of 8 nm n/i i-a-SiGe:H the J_{sc} increases, which is mostly likely due to separating photogenerated electrons from holes. This combination supports each other in terms of J_{sc} compared to the individual n/i and i/p buffers.

Combining the n/i and i/p buffers clearly decreases the overall FF compared to n/i i-a-SiGe:H buffer and does not reach the same V_{oc} as the i/p i-a-SiGe:H. Therefore, the combination does not support each other in terms of FF and V_{oc} and is not improving the overall results.

The last buffer is the combination of buffers which includes n/i i-a-Si. The V_{oc} and FF are improved by the addition of the 3.2 nm n/i i-a-Si buffer. This is due to the decrease of defects at the n/i interface by inserting the n/i i-a-Si layer in the intrinsic layer [75]. The R_{sh} increased from 4825 to 5045 Ωm^2, while the R_s decreased from 11.6 to 10.5 Ωm^2.

The addition of i/p i-a-SiGe:H significantly reduces the FF. This reduction is due to a decrease of R_{sh} from 5045 to 4690 Ωm^2 and an increase in R_s from 10.5 to 13.6 Ωm^2. The i/p i-a-SiGe:H will likely act as a charge barrier and block collection. Moreover, the J_{sc} seems to be saturated and the maximum J_{sc} of 12.2 is reached with addition of the i/p i-a-SiGe:H buffer. The 3.2 nm n/i i-a-Si and 5 nm n/i i-a-SiGe:H buffer combination shows the highest product in terms of V_{oc} and FF.

The best performing buffers are summarized in Table 5.4.

Table 5.4: The overall comparison between different best performing buffers with an initial GeH_4 flow rate of 2.4 sccm.

Buffer	**Efficiency**	**V_{oc}**	**FF**	**J_{sc}**	**R_s**	**R_{sh}**
	[%]	[mV]	[-]	[mA/cm^2]	[Ωm^2]	[Ωm^2]
No Buffer	5.03	733	0.58	11.75	13.95	4134
5 nm n/i i-a-SiGe:H	5.81	721	0.63	12.71	11.19	6450
2 nm i/p i-a-SiGe:H	5.39	722	0.60	12.41	14.26	3350
8 nm n/i i-a-SiGe:H + 5 nm i/p i-a-SiGe:H	6.09	726	0.61	13.74	12.20	6172
3.2 nm n/i i-a-Si + 5 nm n/i i-a-SiGe:H	5.75	739	0.65	12.03	10.52	5045

The i/p buffer seems to be the bottleneck in overall performance. It forms a potential charge barrier and therefore blocks collection. The 8 nm n/i i-a-SiGe:H + 5 nm i/p i-a-SiGe:H buffer shows the highest efficiency of all performed buffers. However, it is chosen to continue with 3.2 nm n/i i-a-Si and 5 nm n/i i-a-SiGe:H due to highest FF and V_{oc}.

The V_{oc} without buffers was equal to 733 mV, with a J_{sc} of 11.75 mA/cm^2, a FF of 0.58 and lastly an efficiency of 5.03%. The V_{oc} of the 3.2 nm n/i i-a-Si buffer combined with the 5 nm n/i i-a-SiGe:H buffer equals a V_{oc} of 739 mV, which is just a slight increase. However, the FF increased from 0.58 to 0.65, which is an increase of almost 12%. Additionally, the J_{sc} was increased by ±0.3 mA/cm^2 and the efficiency was relatively increased by 14.3%. Therefore, it is likely to conclude that the additional buffer layer reduces the interface recombination and increases relaxation of the bandgap discontinuity at the interface [74].

5.2.5. Grading width

Previous literature suggests that the width of the profiled region of the intrinsic a-SiGe:H layer next to the p–i interface (p–i grading) should be small and the profiled region next to the i–n interface (i–n grading) should be large [76]. This will enhance both V_{oc} and FF.

The grading width is an iterative process. In the paragraph about shapes we have observed that a wider n/i grading width increases the performance of the cell. To investigate the appropriate bandgap grading width, the n/i grading width was varied from 80-140 nm.

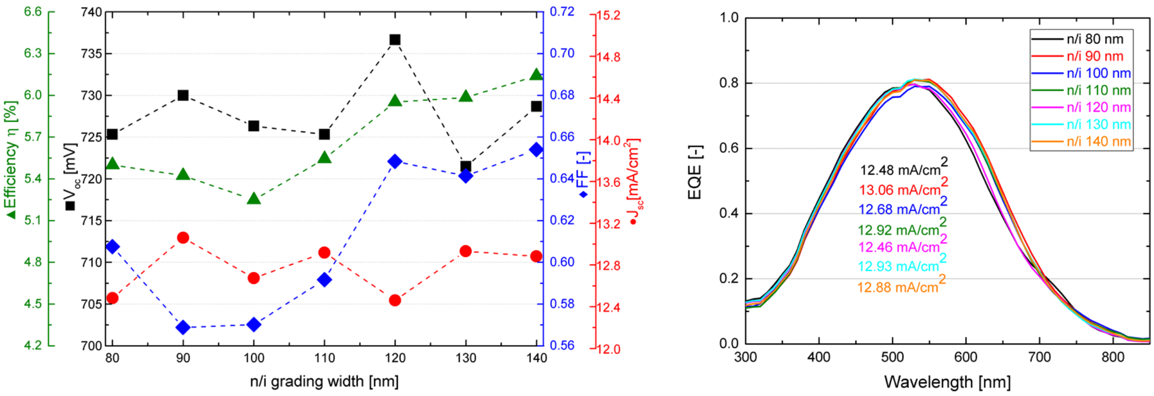

(a) (b)

Figure 5.17: The effect of variations in the n/i grading width from 80-140 nm with a V-shape GeH_4 flow rate of 2.4 sccm on a-SiGe:H solar cell parameters **(a)** and EQE **(b)**.

Figure 5.17a displays that the FF decreases with a smaller n/i grading width. When the n/i grading width is increased, a large improvement can be found in FF. The J_{sc} is saturated and fluctuates with a maximum of 0.5 mA/cm^2.

The V_{oc} is slightly improved with smaller n/i grading compared to wide n/i grading. The deeper back grading at the i/p interface in the V-type profile decreases the charged defect state density near the i/p interface, leading to a higher internal electric field [70], due to a higher bandgap at the i/p interface. This displays a reduction in the i/p interface recombination, due to an increase in R_{sh} from 3674 Ωm^2 to 3869 Ωm^2, which improves the V_{oc} slightly.

On the other hand, the FF decreases with a smaller n/i grading width. This is likely due to increased recombination near the i/n interface by an increase in R_s from 10.7 to 12.1 Ωm^2 and an overall lower bandgap at the i/n interface. However, after a n/i grading width of 100 nm an increase is observed in FF, caused by an improvement of R_s from 10.6 to 9.0 Ωm^2. The n/i grading width improved the carrier collection significantly [68].

Figure 5.17 suggests that an improvement in performance can happen after increasing the n/i grading width to a point behind 140 nm and therefore extra grading width experiments have been performed.

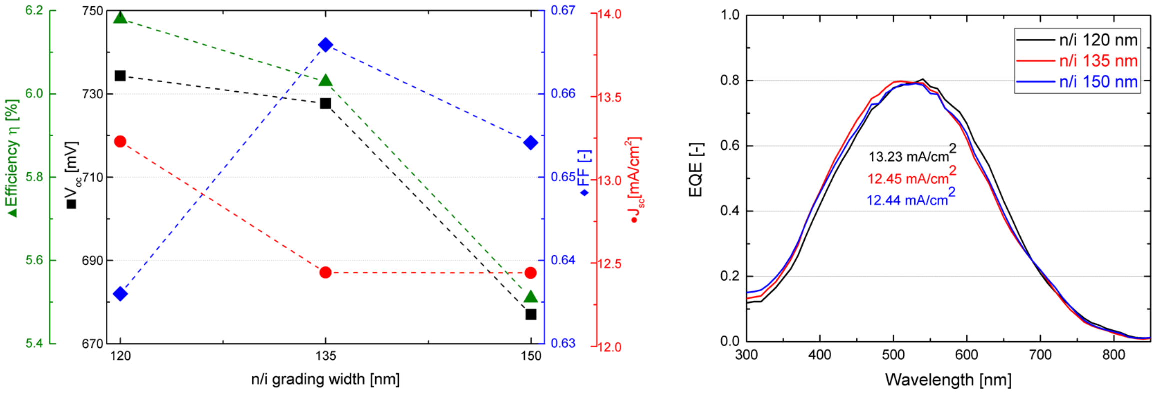

(a) (b)

Figure 5.18: The effect of variations in n/i grading width from 120-150 nm with a V-shape GeH_4 flow rate of 2.4 sccm on a-SiGe:H solar cell parameters **(a)** and EQE **(b)**.

Figure 5.18a displays that the highest efficiency is reached with a n/i grading width of 120 nm, due to the high J_{sc}. At 150 nm there is no bandgap minimum near the i/p interface. The lack of a bandgap minimum near the i/p interface clarifies the decreased FF. The lower V_{oc} is explained by the low bandgap at the i/p interface, due to a high GeH_4 flow rate.

At a n/i grading width of more than 120 nm one would expect a high J_{sc}, because a significant part of the intrinsic layer has a low bandgap. However, Figure 5.18b displays that, in this case it suppresses the carrier generation in the active layer of the solar cell and thus the J_{sc}. This decrease in EQE is likely due to the inefficient hole collection coming from the low drift mobility of holes in amorphous material [77].

Figure 5.17 and 5.18 both show that a n/i grading width of 120 nm for the V-shaped a-SiGe:H layer performs best. The improvement for n/i grading width of 120 nm in J_{sc} in Figure 5.18 compared to 5.17 is due to compensation for changed deposition rates in a-SiGe:H. Therefore, the layer will be slightly thicker. This slightly suppresses the V_{oc} and FF, but improves the J_{sc}, due to addition of GeH_4.

5.2.6. Champion single junction solar cell

The intrinsic layer optimization chapter started with a variation of GeH$_4$ flow rate for the non-optimized a-SiGe:H single junction solar cells. The chapter will end with the optimized variation of GeH$_4$ flow rate, including grading and buffers.

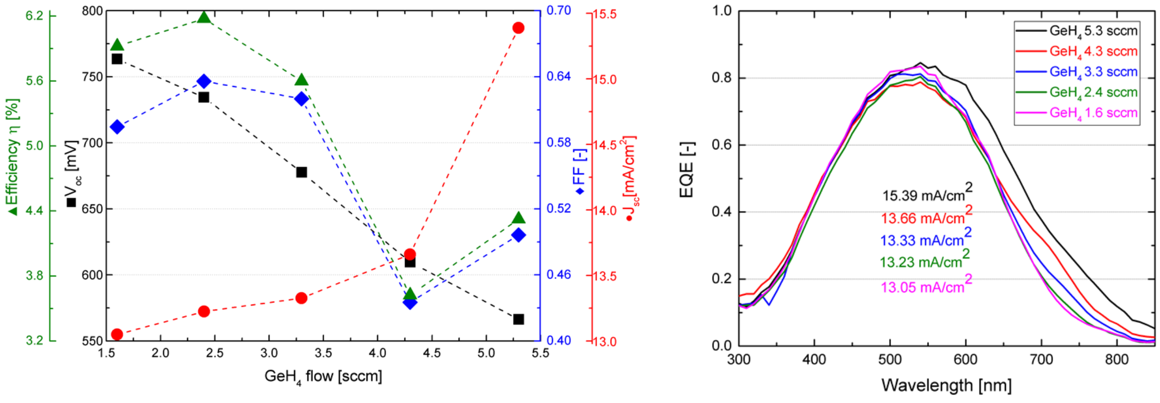

(a) (b)

Figure 5.19: The effect of variations of GeH$_4$ flow rate with buffers and grading on a-SiGe:H solar cell parameters **(a)** and EQE **(b)**.

Figure 5.19 displays the final single junction solar cell serie with a variation of GeH$_4$ flow rate including buffers and grading. The buffers and grading are especially optimized for high bandgap materials, which means a low GeH$_4$ flow rate. An overall comparison of the results is given in Table 5.5.

Table 5.5: The comparison between single junction solar cells with an initial V-shape GeH$_4$ flow rate of 2.4 sccm without a new grading profile and buffer layers compared to the optimized champion single junction solar cell.

Measured	**Efficiency**	**V$_{oc}$**	**FF**	**J$_{sc}$**	**R$_s$**	**R$_{sh}$**
	[%]	[mV]	[-]	[mA/cm^2]	[Ωm^2]	[Ωm^2]
Initial	4.1	657.0	0.52	12.0	22.0	1744.5
Champion	6.2	734.3	0.64	13.2	11.0	4779.5
Absolute Change	2.1	77.3	0.12	1.2	-11.0	3035.0
Relative Change	51 %	12%	22%	10%	-50%	174%

The overall champion single junction a-SiGe:H solar cell is the V-shaped cell with a double n/i buffer, namely 3.2 nm n/i i-a-Si combined with 5 nm n/i i-a-SiGe:H buffer. It has a GeH$_4$ flow rate of 2.4 sccm, n/i grading width of 136 nm, an i/p grading width of 34 nm and a total i-layer thickness of 170 nm. This champion single junction solar cell generates a V$_{oc}$ of 735 mV, a FF of 0.64, a J$_{sc}$ of 13.2 mA/cm^2 and a final efficiency of 6.18%.

The efficiency is relatively increased by 51.1%, the V$_{oc}$ by 12.5%, the FF by 23.1% and lastly the J$_{sc}$ is also improved by 10.4%. Important factor to mention is that Table 5.5 is not the first a-SiGe:H deposition compared to the champion cell. The initial cell is the first cell after optimization of TCO, p- and n-layer. Therefore, those differences in performance are relatively smaller compared to the first a-SiGe:H single junction solar cells, where a V$_{oc}$ of 508 mV, a FF of 0.39, a J$_{sc}$ of 9.9 mA/cm^2 and a final efficiency of 2.9% was reached. This is a relative increase of 44.5% in V$_{oc}$, a 64.1% increase in FF, a 33.6% increase in J$_{sc}$ and a relatively increase of 113.8% in efficiency.

The final thickness of the i-layer is 170 nm instead of 150 nm. Therefore, the n/i grading width moves relatively the same amount (from 120 to 136 nm). The layer is thicker to compensate for the different deposition rates during grading and therefore small differences in FF and V$_{oc}$ can be observed compared to previous results.

6

Tandem Cell

This chapter will be a demonstration of a two-junction a-Si and a-SiGe:H based solar cell. The last research question will be answered, namely to what extend can the a-SiGe:H absorber layer be manipulated for use in a multi-junction device.

The devices investigated in this section are two-junction tandem solar cells with an a-SiGe:H bottom cell and an a-Si top cell. If the intrinsic layer properties will change, it will be stated.

In a multi-junction device multiple single junction cells are generally connected in series. Therefore, the voltages of those cells are summed up, while the current of the lowest performing cell is limiting. The current generated by the high bandgap top cell absorber and the low bandgap bottom absorber should be matched so that that the output of the device is maximal [13].

The EQE measurements of the top and bottom cell are performed separately. To measure the top cell, the bottom cell is saturated by IR light with a peak intensity at a wavelength of 850 and 935 nm. The bottom cell measurement is performed by saturating the top cell by UV light with a peak intensity at a wavelength 365-400 nm and Royal Blue light with a peak intensity at a wavelength of 447.5 nm. The presented current limiting J_{sc} is the lowest of the top and bottom cell J_{sc} measured in EQE.

The single junction a-SiGe:H performed best when processed on Corning glass, while a-Si cells are generally processed on Asahi. Therefore, the first set of tandems was processed on both substrates. This first tandem cell deposition on both substrates showed a slight difference between V_{oc} and FF in favour of Asahi compared to Corning glass, due to increased R_{sh}, see Appendix F. However, the main difference is observed in J_{sc}. An average difference in J_{sc} of around 40% in the bottom cell is found. This is due to better light trapping techniques of the Asahi glass. Consequently, Asahi is used to process the tandems in this section.

6.1. Tandems best a-SiGe:H

Firstly, the tandems started with the standard single junction a-Si cell on top of the best working a-SiGe:H cell, see Appendix F.

However, the bottleneck of the tandem was the current mismatch. The top cell absorbs 9.5 mA/cm^2, while the bottom cell absorbs around 3.8 mA/cm^2. This is related to the overlap of spectral absorption between the top and bottom cell. The bandgap of the bottom absorber is close to the bandgap of the top absorber, due to the relatively low GeH$_4$ flow rate in combination with the V-shape. Therefore, manipulation techniques will be used to manipulate the tandem for current matching.

6.2. Tandems a-Si/a-Si:H

The low bandgap a-Si top cell and best a-SiGe:H cell show a large current mismatching. One of the manipulation options is to replace the low bandgap a-Si top cell by a high bandgap a-Si:H. This has the purpose to decrease the overlap of spectral absorption between the bottom and top absorbers. a-Si:H with higher bandgap transmits lager part of the spectrum, which should leave more light for the a-SiGe:H absorber.

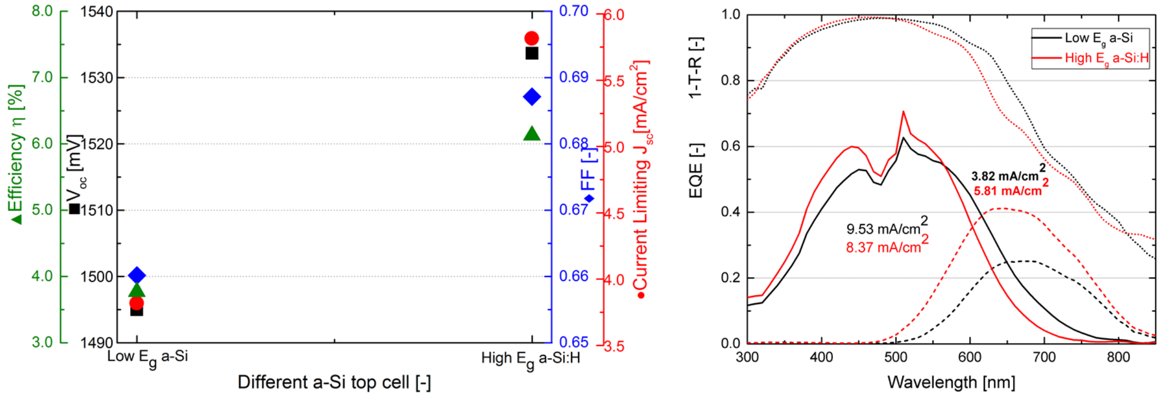

(a) (b)

Figure 6.1: The effect of different top cell absorbers of 250 nm and a 170 nm a-SiGe:H bottom cell absorber with a V-shape GeH$_4$ flow rate of 2.4 sccm on solar cell parameters of tandem solar cells **(a)** and the effect on EQE **(b)**.

Figure 6.1a displays an increase in all solar cell parameters for a-Si:H top cell compared to a-Si top cell. The V$_{oc}$ increased by almost 40 mV. , This is due to an increase in top cell bandgap and an increase of R$_{sh}$ from 13066 Ωm^2 to 16538 Ωm^2. Additionally, an increase in FF is observed due to a decrease in R$_s$ from 21.0 Ωm^2 to 14.9 Ωm^2. Finally, the current limiting J$_{sc}$ increased from 3.8 to 5.8 mA/cm^2, which dictated the increase in efficiency.

Figure 6.1b displays that the low bandgap a-Si generated a higher top cell J$_{sc}$ compared to the high bandgap a-Si:H top cell. Material characterization showed that a decrease in substrate temperature increased the bandgap. The high bandgap a-Si:H is deposited at low substrate temperature of 120°C compared to 180°C for low bandgap a-Si. Additionally, since H$_2$ is introduced in the a-Si layer, the bandgap increased even more. This increased the top cell bandgap and decreased the top cell absorption.

The most important fact is that the bottom cell absorption is increased and the top cell absorption decreased by using the high bandgap a-Si:H. The current limiting J$_{sc}$ is increased by almost 50%. The dotted line in Figure 6.1b shows that a-Si:H with higher bandgap transmits lager part of the spectrum, which leaves more light for the a-SiGe:H absorber, especially between a wavelength of 500-800 nm. Since the purpose of the tandems is to make the top and bottom cell current matched, a-Si:H is an interesting option.

6.3. Tandems GeH_4 flow rate

In the previous paragraph we have seen that the top and bottom cell were not current matched. Besides, replacing the a-Si top cell by a-Si:H, one of other manipulation options is to change the a-SiGe:H absorber layer. This can be done by a variation of the GeH_4 flow rate, as displayed in Chapter 4. This has the purpose to decrease the overlap of spectral absorption between the bottom and top absorbers. Therefore, in this paragraph the GeH_4 flow rate is increased from ±2.3 to 4.3 and 5.3 sccm, because this should decrease the bandgap of the bottom cell.

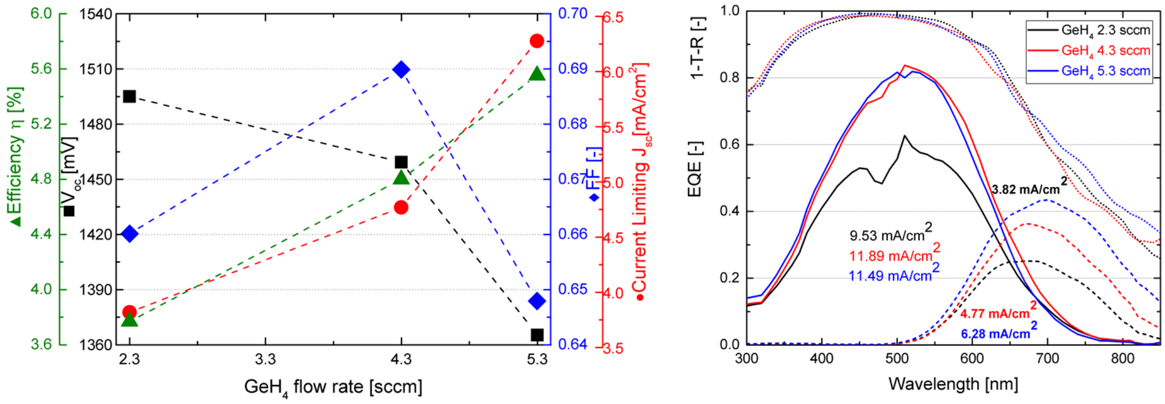

(a) (b)

Figure 6.2: The effect of different V-shape GeH_4 flow rates with a 250 nm a-Si top cell absorber and a 170 nm a-SiGe:H bottom cell absorber on solar cell parameters of tandem solar cells **(a)** and the effect on EQE **(b)**.

Figure 6.2a indicates that an increase in GeH_4 flow rate decreases the V_{oc}. Additionally, the FF decreases, while the R_s and R_{sh} both decrease. It is likely that the decrease in R_{sh} outweighs the decrease of R_s with increasing GeH_4. The GeH_4 flow rate of 4.3 sccm shows a higher FF, which could be due to a processing error. At high GeH_4 flow rate the plasma conditions are less stable and therefore nanoparticles can be formed in the plasma and attach themselves to the substrate [4]. This could have affected the tandem with a GeH_4 flow rate of 4.3 sccm. Other parameters are as expected, due to an increase in GeH_4 the V_{oc} decreases. This is related to a decrease in bandgap and therefore the J_{sc} increases.

Figure 6.2b shows that an increase of the GeH_4 flow rate leads to an increase in J_{sc} of the bottom cell, due to a lower bandgap. Additionally, a lower GeH_4 flow rate gives a lower refractive index, therefore less light is reflected back to the top cell after reaching the bottom cell i/p interface, which results in the lower J_{sc} in the top cell at a GeH_4 flow rate of 2.4 sccm. Combining the results of Figure 6.2 indicates that although a higher GeH_4 has a lower V_{oc} and FF compared to a GeH_4 flow rate of ±2.3 sccm, the increase in J_{sc} of the current limiting bottom cell increases the overall efficiency.

After those deposition a decision is made to continue with a combination of high bandgap a-Si:H and a GeH_4 flow rate of 5.3 sccm, due to the goal of making a current matched tandem. To increase the overall efficiency, which is dictated by the current limiting cell, the J_{sc} of the bottom cell should be increased, to level the top cell.

Firstly, some basic optical simulations with the `GenPro4` software are performed to get an indication of the thickness range of the a-Si:H top cell, see Appendix E.

6.4. Tandems V-shape

In the previous paragraphs we have seen that the top and bottom cell were not current matched. One of the manipulation options is to decrease the top cell a-Si:H thickness while using the V-shaped GeH_4 flow rate. Therefore, in this paragraph the a-Si:H thickness is decreased from 250 to 150 nm. A total thickness of 170 nm is used for a-SiGe:H bottom cell with a n/i width of 136 nm and an i/p width of 34 nm.

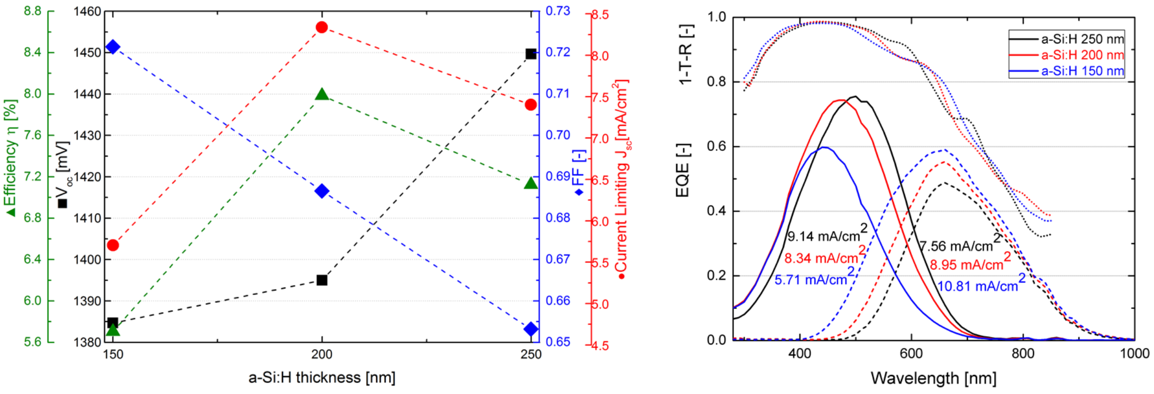

(a) (b)

Figure 6.3: The effect of different a-Si:H top cell thickness with a 170 nm a-SiGe:H bottom cell absorber with a V-shape GeH_4 flow rate of 5.3 sccm on solar cell parameters of tandem solar cells **(a)** and the effect on EQE **(b)**.

An increase in a-Si:H thickness linearly decreases the FF from 0.72 to 0.65. This is likely caused by an increase in R_s from 12.4 to 16.2 Ωm^2. The V_{oc} increases with an increase in thickness, due to an increase in R_{sh} from 16148 to 18673 Ωm^2. Additionally, a single junction a-SiGe:H with a V-shape and a GeH_4 flow rate of 5.3 sccm can reach a V_{oc} of 570 mV, which means that in this two-junction device 880 mV is reached in the top cell of 250 nm. Figure 6.3a indicates that an increase of the a-Si:H thickness improves the voltage of the top cell, namely an additional 55 mV over 100 nm extra thickness of a-Si:H.

The efficiency reached the maximum at an a-Si:H thickness of 200 nm, which gives an efficiency of around 8%. The top cell becomes current limiting here, while at 250 nm the current mismatch is higher and the bottom cell is limiting.

Figure 6.3b reveals that the low top cell J_{sc} for a thickness of 150 nm is out of the expected range. It is likely that this is due to the fact that a thinner top layer than 150 nm is deposited due to non-uniformity in the process. The thinner a-Si:H layer decreases the top cell J_{sc} and therefore increases the J_{sc} of the bottom cell.

Measurements, see Appendix D, show that the refractive index increases linearly with addition of GeH_4 in a-SiGe:H. The use of a GeH_4 flow rate of 5.3 sccm at the V-shaped a-SiGe:H layer results in relatively high refractive index of around 4.8, at a wavelength of 589 nm, which creates a large refractive index mismatch at the i/p interface of the bottom cell. A fraction of the light is, therefore, reflected to the top cell before being absorbed by the bottom cell absorber layer, due to the sharp edge at the i/p interface of the bottom cell.

6.5. Tandems U-shape

In the previous paragraph we have seen that with the use of the V-shape a-SiGe:H absorber, the top and bottom cell were not completely current matched. One of the manipulation options is to decrease the top cell a-Si:H thickness while using the U-shaped GeH_4 flow rate. Therefore, in this paragraph the a-Si:H thickness is decreased from 250 to 150 nm. Additionally, a U-shaped GeH_4 flow rate with a total thickness of 170 nm is used for a-SiGe:H bottom cell with a n/i width of 34 nm, an i-i width of 102 nm and an i/p width of 34 nm.

The U-shape is used in the tandem due to the higher J_{sc} compared to other shapes, shown in Chapter 5.

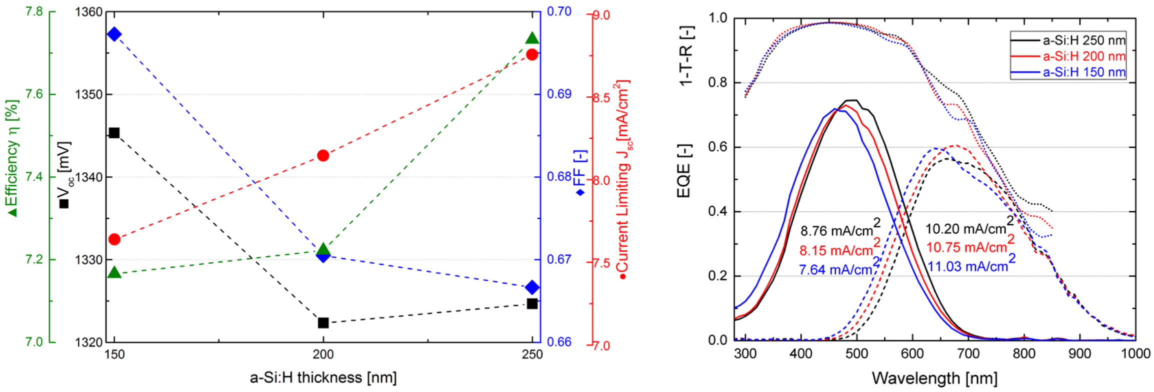

(a) (b)

Figure 6.4: The effect of different a-Si:H top cell thickness with a 170 nm a-SiGe:H bottom cell absorber with a U-shape GeH_4 flow rate of 5.3 sccm on solar cell parameters of tandem solar cells **(a)** and the effect on EQE **(b)**.

Figure 6.4a shows that the use of the U-shape adds more GeH_4 in the layer, which decreases the bottom cell bandgap. This lowers the V_{oc} and increases the J_{sc}. The V_{oc} of the U-shape is 5% lower than the V-shape. The decrease in FF, while increasing a-Si:H thickness, is mostly dictated by the increase in R_s from 15.2 to 18.8 Ωm^2. The V_{oc} decreases with an increase in thickness, partly due to a decrease in R_{sh} from 14584 to 10732 Ωm^2.

As can be seen in Figure 6.4b the top cell becomes current limiting, due to GeH_4 addition. The best result for the U-shape is achieved with a thickness of 250 nm for the a-Si:H top cell and gives an efficiency of around 7.8%.

With the use of the U-shape, less light is reflected back to the top cell compared to the V-shape, due to both the absence of a sharp edge at the i/p side and the high constant refractive index at a high GeH_4 flow rate. Therefore, it is likely that more light is absorbed in the bottom cell and a small fraction is reflected back compared to the V-shape. Additionally, a possible explanation can be that high GeH_4 flow rate changes the morphology and the texturing of the bottom cell. Therefore, it becomes more rough and less light will be scattered/reflected back to the top cell. This can be due to internal reflection by the roughness created at the average high GeH_4 flow rate in the U-shape.

Figure 6.3 and 6.4 clarify this statement. The U-shape results show that the top cell absorbs less current than the V-shape, due to less sharp edges at the i/p interface. The parasitic absorption of the cell becomes more sensitive to the TCO and top cell thickness (a-Si:H). Other parasitic absorption can be due to the n-a-Si:H from the top cell in the tunnel recombination junction of the two cells. The absorptance showed smaller losses around 750-800 nm for the U-shape compared to the V-shape, due to higher GeH_4flow rate more light will be effectively transmitted to the bottom cell.

6.6. Overview tandems

Table 6.1: Overview of parameters of the best V- and U-shape a-Si:H/a-SiGe:H tandem solar cells with a GeH_4 flow rate of 5.3 sccm.

Tandems	**Efficiency**	**V_{oc}**	**FF**	**J_{sc} Top**	**J_{sc} Bottom**
	[%]	[mV]	[-]	[mA/cm^2]	[mA/cm^2]
a-Si:H 200 nm/a-SiGe:H 170 nm - V-shape	7.99	1395.00	0.69	8.34	8.95
a-Si:H 250 nm/a-SiGe:H 170 nm - U-shape	7.73	1324.67	0.67	8.76	10.20

Table 6.1 displays that the overall champion solar cell is the V-shaped cell with a thickness of 200 nm with a high bandgap a-Si:H top cell and a thickness of 170 nm for the a-SiGe:H bottom cell. This champion tandem solar cell generates a V_{oc} of 1395 mV, a FF of 0.69, a current limiting J_{sc} of 8.34 mA/cm^2 and a final efficiency of 7.99%.

We have seen that an increase in GeH_4 flow rate increases the defect density. This is explained by the Raman spectra, the decreasing FF and previous literature. However, the research showed that it is possible to manipulate the cell by changing the a-SiGe:H absorber. The change in top and bottom cell thickness, the maximum GeH_4 flow rate and the U- and V-shape profiles can all be interesting manipulation options in a multi-junction device for different purposes, due to their flexibility, to increase the current limiting J_{sc} to improve current matching.

7

Conclusions and Recommendations

In this thesis the development of n-i-p substrate a-SiGe:H thin-film silicon solar cells is studied. In particular, it focuses on the intrinsic a-SiGe:H layer. This chapter provides a summary of the most important findings of this thesis. Additionally, it provides recommendations for further research. The aim of this thesis is summarized by the following statement:

"The characterization and determination of the range of device grade a-SiGe:H absorbers, that can flexibly be used in multi-junction devices, taking into account absorber bandgap, thickness, grading profile and buffer layers".

This statement was divided in four scientific questions. The following sections will discuss those scientific questions.

7.1. Material characterization

The first research question, stated in Chapter 1 is:
Which combination of deposition parameters can be used to process a range of device grade a-SiGe:H absorber layers?

The material characterization was carried out in Chapter 4. An investigation of deposition parameters showed that variation of the peak flow rate of GeH_4/SiH_4 can directly influence the optical-, electrical- and material properties due to the fact that it changes the GeH_4 concentration in the material. An increase in GeH_4 peak flow rate from 0.8 to 5.3 sccm decreases the bandgap by around 0.2 eV. It increases dark conductivity by 10^2 S/cm, likely related to bandgap decrease and defect increase. This decrease in bandgap is related to the increase in Ge-Ge bonds and due to the fact that Ge has a lower bandgap, 0.67 eV, compared to Si, 1.11 eV. Additionally, the absorption coefficient increases with increasing GeH_4 flow rate.

However, the H_2/SiH_4 ratio, the deposition pressure, the substrate temperature and the deposition power can have an indirect influence on the properties by indirectly changing the GeH_4 composition in the material, which is assumed to be the most important in this thesis. The influences of different deposition parameters on the dark conductivity, bandgap and absorption coefficient are summarized in Table 4.2.

7.2. Single junction solar cell grading

The second research question, stated in Chapter 1 is:
Which bandgap grading profile in terms of shape, grading region width and absorber thickness should be used to process a range of device grade a-SiGe:H absorber single junction devices?

After material characterization a reference n-i-p substrate solar cell is fabricated with Corning glass as substrate. This fabrication is done by reversing the p-i-n superstrate single junction a-SiGe:H solar cell processed by the PVMD group [63]. Due to low performance, manipulation techniques are used.

We have seen that an increase in GeH_4 flow rate from 1.6 to 5.3 sccm decreases the V_{oc} from 740 to almost 510 mV, the FF drops around 0.15, the defect density increases and that the J_{sc} increases by almost 3.5 mA/cm^2, which is related to bandgap decrease of over 0.2 eV in a-SiGe:H films. Therefore, the GeH_4 flow rate can be an interesting manipulation option in multi-junction devices.

Bandgap grading of the intrinsic layer is another important manipulation technique and is carried out in Chapter 5. The shapes consist of bandgap grading in the absorber through GeH_4 concentration profiling. The E-, U- and V-shapes are proposed as different grading profiles. The V-shape suffers due to an average lower GeH_4 flow rate from a lower J_{sc}, however it still outperforms other shapes based on the product of V_{oc} and FF. It increased the overall performance by 22%.

Additionally, an increase in n/i grading width from 80-120 nm mainly increased the FF, due to lower recombination at the n/i interface, which is related to a higher overall bandgap and increase of carrier collection. Finally, an increased absorber layer thickness of more than 150 nm suppresses the V_{oc} and FF, but enhances the J_{sc}. This is another interesting manipulation tool for multi-junction devices.

7.3. Single junction solar cell buffers

The third research question, stated in Chapter 1 is:
Which buffer layer and buffer layer thickness should be be used to process a range of device grade a-SiGe:H absorber single junction devices?

The different buffer options were carried out in Chapter 5. High bandgap i-a-SiGe:H and i-a-Si buffers are investigated both on the defective n/i and i/p interfaces, including buffer thickness change from 0 to 11 nm. The n/i interface was most crucial for significant improvement. The increase of i/p i-a-SiGe:H buffer thickness increased the J_{sc}, but did act as charge barrier and significantly decreased the FF. Combining the n/i i-a-SiGe:H and i/p i-a-SiGe:H buffers did support each other in terms of increased J_{sc}, but suffers from FF decrease. The extra addition of 3.2 nm n/i i-a-Si buffer with 5 nm n/i i-a-SiGe:H buffer increased both V_{oc} and FF compared to single i/p i-a-SiGe:H and single n/i i-a-SiGe:H buffer and suffers slightly from a decrease in J_{sc}. Therefore, the combination of 3.2 nm n/i i-a-Si buffer and 5 nm n/i i-a-SiGe:H buffer outperformed the other buffers, which included different i/p i-a-SiGe:H and n/i i-a-SiGe:H buffer thicknesses, and increased overall performance by 14.3%.

The overall champion single junction a-SiGe:H solar cell has a 3.2 nm n/i i-a-Si buffer combined with a 5 nm n/i i-a-SiGe:H buffer, a V-shape GeH_4 peak flow rate of 2.4 sccm, a 134 nm n/i grading width, a 36 nm i/p grading width and a total absorber thickness of 170 nm. This champion single junction solar cell generates a V_{oc} of 735 mV, a FF of 0.64, a J_{sc} of 13.23 mA/cm^2 and a final efficiency of 6.2%, while the first deposited a-SiGe:H single junction solar cell, the earlier mentioned flipped p-i-n a-SiGe:H, had a V_{oc} of 508 mV, a FF of 0.39, a J_{sc} of 9.9 mA/cm^2 and a final efficiency of 2.9%. This is a relative increase of 113.8% in efficiency. Therefore, it can be said that buffer type and thickness, different profiling schemes, grading widths and total absorber thickness can strongly improve the overall device performance of a n-i-p substrate a-SiGe:H single junction solar cell.

7.4. Two-junction solar cell

The final research question, stated in Chapter 1 is:
To what extend can the a-SiGe:H absorber layer be manipulated for use in a multi-junction device?

The different two-junction device manipulation techniques were carried out in Chapter 6. The current generated by the top cell and the bottom cell should be matched so that the output of the device is maximal. The first tandems showed that the bottom and top cell were not matched. Therefore, based on the single junction device results different manipulation techniques are used, namely (i) a-Si top cell replacement by a-Si:H, (ii) variation of the GeH_4 peak flow rate, (iii) changing thickness of the a-Si:H top cell and (iv) variation of the a-SiGe:H grading shape from V- to U-shape. The goal of these manipulation techniques is to decrease the overlap of spectral absorption between the top and bottom cell for current matching.

Firstly, the change of a-Si to a-Si:H increases the transmitted light to the bottom cell and increases the bandgap of the top cell, which decreases the J_{sc} in the top cell. Secondly, Chapter 4 indicated that the J_{sc} increases by increasing the GeH_4 flow rate. An increase in GeH_4 flow rate decreases the V_{oc} and FF. Thirdly, the decrease of a-Si:H top cell thickness decreases the V_{oc} and J_{sc} of top cell, but transmits more light to the bottom cell. Finally, the change in a-SiGe:H shape from V to U decreases the overall bandgap of the a-SiGe:H bottom cell, which leads to an increase in J_{sc}. The V-shape showed a larger refractive index mismatch at the i/p interface of the bottom cell. A fraction of the light is, therefore, reflected to the top cell before being absorbed by the bottom cell absorber layer, due to the sharp edge at the i/p interface of the bottom cell. Additionally, more light is reflected back to the top cell when using the V-shape compared to the U-shape, where more light is internally reflected, likely by an increase in roughness due to the high constant GeH_4 flow rate. The V-shape a-SiGe:H bottom cell increases the J_{sc} of the top cell compared to the U-shape.

The overall champion tandem solar cell consists of a 200 nm a-Si:H top cell and a 170 nm a-SiGe:H bottom cell with a V-shape GeH_4 peak flow rate of 5.3 sccm. This champion tandem solar cell generates a V_{oc} of 1395 mV, a FF of 0.69, a current limiting J_{sc} of 8.34 mA/cm^2 and a final efficiency of 7.99%.

7.5. Recommendations

The main focus of the recommendations will be on the multi-junction tandem. However, on material characterization level extra XPS measurements for typical content description of the Ge in the layer could be performed. Optionally, PDS measurements on a-SiGe:H for precise determination of the absorption coefficient could be done. However, the most interesting recommendations will be focused on multi-junction devices.

Firstly, the thickness of a-Si:H top cell could be increased, while using the U-shape a-SiGe:H for current matching of the J_{sc} of top and bottom cell. It is likely that in such a two-junction device a current matching J_{sc} of around 9.4-9.5 mA/cm^2 could be reached. However, the V_{oc} will be lower compared to the V-shape, but will increase compared to a thinner a-Si:H top absorber. Nonetheless, the long wavelength absorption of the U-shape can give some conflicts if a triple-junction will be used, because the bottom nc-Si cell starts absorbing around 900-1000 nm and if the bottom layer won't get sufficient light it will be current limiting.

Secondly, the thickness of the a-Si:H top cell could be increased, while using the V-shape a-SiGe:H. It is likely that in a two-junction device current matching J_{sc} of 8.5-8.6 mA/cm^2 can be reached, including a higher V_{oc} compared to the U-shape. The V_{oc} can even increase further if it follows the trend. Moreover, an advantage is that this bottom cell is less absorbing in the longer wavelengths and will likely increase the chance of sufficient current absorption in the nc-Si bottom cell in a triple-junction tandem device. Therefore a trade-off can be made between both U- and V-shape for the a-SiGe:H cell, depending on the purpose of the device.

Finally, the U- and V-shape could be customized, so a wide n/i grading will be combined with a short i-i plateau so the J_{sc} could be increased, while just suppressing the V_{oc} slightly. Further investigation depends on the type of device and the desired output in terms of V_{oc} and J_{sc}. This also includes p-layer optimization, due to the fact that it will be part of the tunnel recombination junction of the multiple-junction solar cell. Therefore, parasitic absorption could be reduced by optimizing this layer.

Bibliography

[1] International Energy Agency. Global Energy & CO2 Status Report The latest trends in energy and emissions in 2018, 2019.

[2] V. Smil and BP Statistical Review of World Energy. Statistical Review of World Energy | Energy economics | Home, 2017.

[3] S. White. What percentage of the light spectrum are humans able to see with their eyes?, 2016.

[4] A.H.M. Smets, K. Jäger, O. Isabella, R.A.C.M.M. Swaaij, van, and M. Zeman. *Solar energy : the physics and engineering of photovoltaic conversion technologies and systems.* UIT, 2016.

[5] T. de Vrijer, F.T. Si, H. Tan, and A.H.M. Smets. Chemical stability and Performance of Doped Silicon Oxide Layers for Use in Thin Film Silicon Solar Cells. *IEEE Journal of Photovoltaics-under review*, 2018.

[6] B. de Mayo. Wave properties. In *The Everyday Physics of Hearing and Vision*. Morgan & Claypool Publishers, 2014.

[7] Chemistry Libretexts. The arrhenius law: Activation energies, 2015.

[8] B. Anton. Photovoltaic cells efficiency of electricity production, 2013.

[9] M.N. Abdi H. Mollaaghaei Z. Enayatim S., Rezaie and A. Rezaei. Iran University of Science & Technology - Nanoptronics Research Center, 2010.

[10] G. Yang. *High-efficient n-i-p thin-film silicon solar cells*. Technical University Delft, 2015.

[11] SolarEnergy. Radio frequency plasma enhanced chemical vapor deposition | Everything about solar energy, 2018.

[12] JEOL. Electron Beam Source for Electron Beam Deposition | Introduction to JEOL Products | JEOL Ltd., 2019.

[13] P. Rodriguez Perez. Photovoltaic-(photo)electrochemical devices for water splitting and water treatment, 2018.

[14] IRENA. Accelerating Renewables Is Our Most Effective Climate Solution. */newsroom/articles/2018/Oct/Accelerating-Renewables-Is-Our-Most-Effective-Climate-Solution*, 2018.

[15] Unfccc. Adoption of the Paris Agreement - Paris Agreement text English. Technical report, United Nations, 2015.

[16] S. Vogel. *Glimpses of creatures in their physical worlds*. Princeton University Press, 2009.

[17] M.A. Green, Y. Hishikawa, E.D. Dunlop, D. H. Levi, J. Hohl-Ebinger, M. Yoshita, and A.W.Y. Ho-Baillie. Solar cell efficiency tables (Version 53). *Progress in Photovoltaics: Research and Applications*, 27(1):3–12, jan 2019.

[18] T.C. Loef. Periodic-Random Modulated Surface Textures, 2018.

[19] M.A. Green and A. Martin. Third generation photovoltaics: solar cells for 2020 and beyond. *Physica E: Low-dimensional Systems and Nanostructures*, 14(1-2):65–70, apr 2002.

[20] Z. Tang, W. Tress, and O. Inganäs. Light trapping in thin film organic solar cells. *Materials Today*, 17(8):389–396, 2014.

[21] Y.T. Huang, H.J. Hsu, S.W. Liang, C.H. Hsu, and C.C. Tsai. Development of hydrogenated microcrystalline silicon-germanium alloys for improving long-wavelength absorption in si-based thin-film solar cells. *International Journal of Photoenergy*, 2014:1–7, 2014.

[22] E. Hecht. *Optics*. Addison-Wesley, 2002.

[23] J. Räty, P. Pääkkönen, K.E. Peiponen, V. Lucarini, J.J. Saarinen, K.E. Peiponen, E.M. Vartiainen, I. Niskanen, J. Räty, H. Koivula, M. Toivakka, J.S. Preston, N.J. Elton, J.C. Husband, J. Dalton, P.J. Heard, and G.C. Allen. Spectroscopy, visible; (120.1840) Densitometers, reflectometers; (120.4530) Optical constants; (160.4890) Organic materials; (260.2030) Dispersion., Kramers-Kronig relations in. Technical report, University of Oulu, 2005.

[24] Arnau A. Silla, E. and Tuñón. Fundamental principles governing solvents use. *Handbook of Solvents*, pages 11–72, jan 2014.

[25] M. Zeman, J. van den Heuvel, M. Kroon, J. Willemen, B. Pieters, J. Krc, and S. Solntsev. Advanced Semiconductor Analysis opto-electronic simulator for amorphous and crystalline semiconductor devices User's Manual. Technical report, Delft University of Technology, Laboratory of Photovoltaic Materials and Devices, 2013.

[26] M. de Grunt. IRFR Manual, PVMD Group, TU Delft, 2013.

[27] G.E. Jellison and F.A. Modine. Erratum: "parameterization of the optical functions of amorphous materials in the interband region" [appl. phys. lett. 69, 371 (1996)]. *Applied Physics Letters*, 69:2137 – 2137, 10 1996.

[28] E.A. Davis and N.F. Mott. Conduction in non-crystalline systems v. conductivity, optical absorption and photoconductivity in amorphous semiconductors. *The Philosophical Magazine: A Journal of Theoretical Experimental and Applied Physics*, 22(179):0903–0922, 1970.

[29] J.P. Conde, V. Chu, M.F. Da Silva, A. Kling, Z. Dai, J.C. Soares, S. Arekat, A. Fedorov, M.N. Berberan-Santos, F. Giorgis, and C.F. Pirri. Optoelectronic and structural properties of amorphous silicon-carbon alloys deposited by low-power electron-cyclotron resonance plasma-enhanced chemical-vapor deposition. Technical report, Instituto Superior Técnico (IST), 1999.

[30] J. Nelson. *The Physics of Solar Cells*. Imperial College Press, may 2003.

[31] V.C.S. Hamoen. Thin film silicon triple junction solar cell for solar fuels, 2017.

[32] C. Christiana Honsberg and S. Bowden. Series resistance, 2019.

[33] S. Kim, J.W. Chung, H. Lee, J. Park, Y. Heo, and H.M. Lee. Remarkable progress in thin-film silicon solar cells using high-efficiency triple-junction technology. *Solar Energy Materials and Solar Cells*, 119:26–35, 2013.

[34] M. Gostein and L. Dunn. Light soaking effects on photovoltaic modules: Overview and literature review. In *2011 37th IEEE Photovoltaic Specialists Conference*, pages 003126–003131, June 2011.

[35] D.L. Staebler and C.R. Wronski. Reversible conductivity changes in discharge□produced amorphous Si. *Applied Physics Letters*, 31(4):292–294, aug 1977.

[36] C.C. Wang, C.H. Liu, S.Y. Lien, K.W. Weng, J.J. Huang, C.F. Chen, and D.S. Wuu. Hydrogenated amorphous silicon-germanium thin films with a narrow band gap for silicon-based solar cells. *Current Applied Physics*, 11(1 SUPPL.):50–53, 2011.

[37] S. Guha, J. Yang, A. Banerjee, B. Yan, and K. Lord. High quality amorphous silicon materials and cells grown with hydrogen dilution. *Solar Energy Materials & Solar Cells*, 78:329–347, 2003.

[38] K. Zweibel. Issues in thin film pv manufacturing cost reduction. *Solar Energy Materials and Solar Cells*, 59(1):1 – 18, 1999.

[39] I. Ibrahim and M.H. Rü. Methods for Obtaining Graphene Mechanical Exfoliation. *Graphene*, pages 129–228, 2013.

[40] R. Jimenez Zambrano. 3 Deposition of a-SiGe:H at low temperatures and high deposition rate. Technical report, University Of Utrecht, 2003.

[41] P.M. Martin. *Handbook of deposition technologies for films and coatings : science, applications and technology*. Elsevier, 2010.

[42] D.M. Mattox. *Handbook of physical vapor deposition (PVD) processing*. William Andrew, Oxford, UK., 2010.

[43] Nanophoton. What is raman spectroscopy?, 2018.

[44] D. Bermejo and M. Cardona. Raman scattering in pure and hydrogenated amorphous germanium and silicon. *Journal of Non-Crystalline Solids*, 32(1):405 – 419, 1979. Electronic Properties and Structure of Amorphous Solids.

[45] O. Madelung, U. Rössler, and M. Schulz. *Germanium (Ge) Raman phonon frequencies and wavenumbers*, pages 1–17. Springer Berlin Heidelberg, Berlin, Heidelberg, 2001.

[46] H. Fritzsche. FRONT MATTER. In *Amorphous Silicon and Related Materials*, pages i–xv. WORLD SCIENTIFIC, jan 1989.

[47] M.H. Brodsky, M. Cardona, and J.J. Cuomo. Infrared and raman spectra of the silicon-hydrogen bonds in amorphous silicon prepared by glow discharge and sputtering. *Phys. Rev. B*, 16:3556–3571, Oct 1977.

[48] W.S. Lau. *Infrared Characterization for Microelectronics*. World Scientific, 1999.

[49] Y. Toyoshima, K. Arai, A. Matsuda, and K. Tanaka. Study of silicon-hydrogen bonds at an amorphous silicon/silicon nitride interface using infrared attenuated total reflection spectroscopy. *Applied Physics Letters*, 60:1942–1944, 1992.

[50] D. Deligiannis, R. Vasudevan, A.H.M. Smets, R.A.C.M.M. Van Swaaij, and M. Zeman. Surface passivation of c-si for silicon heterojunction solar cells using high-pressure hydrogen diluted plasmas. *AIP Advances*, 5:097165, 09 2015.

[51] H. Fujiwara and R.W. Collins. *Spectroscopic Ellipsometry for Photovoltaics*, volume 1. Springer Series in Optical Sciences, 2018.

[52] A.K. Singh, J. Tiwari, A. Yadav, and R.K. Jha. Analysis of Si/SiGe Heterostructure Solar Cell. *Journal of Energy*, 2014(July):1–7, 2014.

[53] L Yang, J Newton, and B Fieselmann. Raman spectroscopy of a.sige:h alloys. *MRS Online Proceedings Library (OPL)*, 149:497–502, 1989.

[54] R. Jimenez Zambrano, F.A. Rubinelli, J.K. Rath, and R.E.I. Schropp. Improvement in the spectral response at long wavelength of a-SiGe:H solar cells by exponential band gap design of the i-layer. *Journal of Non-Crystalline Solids*, 299-302(PART 2):1131–1135, 2002.

[55] W. Paul, D.K. Paul, B. von Roedern, J. Blake, and S. Oguz. Preferential attachment of h in amorphous hydrogenated binary semiconductors and consequent inferior reduction of pseudogap state density. *Phys. Rev. Lett.*, 46:1016–1020, Apr 1981.

[56] G.A.N. Connell and J.R. Pawlik. Use of hydrogenation in structural and electronic studies of gap states in amorphous germanium. *Phys. Rev. B*, 13:787–804, Jan 1976.

[57] I. Nakamura, T. Ajiki, H. Abe, D. Hoshi, and M. Isomura. Formation of polycrystalline sige thin films by the rf magnetron sputtering method with ar–h2 mixture gases. *Vacuum*, 80(7):712 – 715, 2006. Selected Papers revised from the Proceedings of the Eighth International Symposium on Sputtering and Plasma Processes (ISSP 2005), 8-10 June 2005, Kanazawa, Japan.

[58] A. Matsuda. Growth mechanism of microcrystalline silicon obtained from reactive plasmas. *Thin Solid Films*, 337(1-2):1–6, jan 1999.

[59] D.Y. Kim, E. Guijt, R.A.C.M.M. van Swaaij, and M. Zeman. Development of a-SiOx:H solar cells with very high Voc and FF product. *Progress in Photovoltaics: Research and Applications*, 23(6):671–684, jun 2015.

[60] Q.H. Fan, G. Hou, X. Liao, X. Xiang, C. Chen, W. Ingler, N. Adiga, S. Zhang, X. Cao, W. Du, and X. Deng. High rate deposition of a-Si and a-SiGe solar cells near depletion condition. *Conference Record of the IEEE Photovoltaic Specialists Conference*, 35(June):1491–1495, 2010.

[61] B. Yan, L. Zhao, B. Zhao, J. Chen, and H. Wang, G.and Diao. High-performance a-SiGe:H thin applications and materials science film prepared by plasma-enhanced chemical vapor deposition with high plasma power for solar-cell application. *Physica Status Solidi*, 2531(12):2527–2531, 2012.

[62] E.C. Molenbroek, A. H. Mahan, E.J. Johnson, and A.C. Gallagher. Film quality in relation to deposition conditions of a-Si:H films deposited by the “hot wire” method using highly diluted silane. *Journal of Applied Physics*, 79(9):7278–7292, may 1996.

[63] H. Tan. *Materials and Light Management for High-Efficiency Thin-Film Silicon Solar Cells.* TU Delft, 2015.

[64] A. Eshaghi and M. Hajkarimi. Optical and electrical properties of aluminum zinc oxide (AZO) nanostructured thin film deposited on polycarbonate substrate. *Optik*, 125(19):5746–5749, oct 2014.

[65] J. Cho, D.P. Pham, J. Jung, C. Shin, J. Park, S. Kim, A.H. Tuan Le, H. Park, S. M. Iftiquar, and J. Yi. Improvement of hydrogenated amorphous silicon germanium thin film solar cells by different p-type contact layer. *Materials Science in Semiconductor Processing*, 41:480–484, 2016.

[66] T. de Vrijer, F.T. Si, H. Tan, and A. H.M.Smets. Chemical stability and performance of doped silicon oxide layers for use in thin-film silicon solar cells. *IEEE Journal of Photovoltaics*, 9(1):3–11, Jan 2019.

[67] T. Matsui, K. Ogata, C.W. Chang, M. Isomura, and M. Kondo. Carrier collection characteristics of microcrystalline silicon-germanium p-i-n junction solar cells. *J. Non-Cryst. Solids*, 354:2468–2471, 05 2008.

[68] H.J. Hsu, C.H Hsu, and C.C. Tsai. The Effect of Bandgap Graded Absorber on the Performance of a-Si 1 − x Ge x : H Single-Junction Cells with □□ c-SiO x : H N -Type Layer. *International Journal of Photoenergy*, 2013, 2013.

[69] F.T. Si, O. Isabella, and M. Zeman. Thin-film amorphous silicon germanium solar cells with p- and n-type hydrogenated silicon oxide layers. *Solar Energy Materials and Solar Cells*, 163(December 2016):9–14, 2017.

[70] R.A.C.M.M. van Swaaij, M. Zeman, S. Arnoult, and J.W. Metselaar. Dependence on grading width of a-SiGe:H solar cells, 2000.

[71] T. Matsui, K. Ogata, M. Isomura, and M. Kondo. Microcrystalline silicon-germanium alloys for solar cell application: Growth and material properties. *Journal of Non-Crystalline Solids*, 352(9-20 SPEC. ISS.):1255–1258, 2006.

[72] K.M. van Veen and R.E.I. Schropp. Beneficial effect of a low deposition temperature of hot-wire deposited intrinsic amorphous silicon for solar cells. *Journal of Applied Physics*, 93:121 – 125, 02 2003.

[73] J. Park, V.A Dao, C. Shin, H. Park, M. Kim, J. Jung, D. Kim, and J. Yi. A buffer-layer/a-siox:h(p) window-layer optimization for thin film amorphous silicon based solar cells. *Thin Solid Films*, 546:331 – 336, 2013. The proceedings of International Union of the Materials Research Society -International Conference in Asia 2012- IUMRS-ICA 2012.

[74] D.P. Pham, S. Kim, J. Park, A. Le, J. Cho, J. Jung, S.M. Iftiquar, and J. Yi. Silicon germanium active layer with graded band gap and µc-si:h buffer layer for high efficiency thin film solar cells. *Materials Science in Semiconductor Processing*, 56, 12 2016.

[75] D. Lundszien, F. Finger, and H. Wagner. Asi:h buffer in a-sige:h solar cells. *Solar Energy Materials and Solar Cells - SOLAR ENERG MATER SOLAR CELLS*, 74:365–372, 10 2002.

[76] B.E. Pieters, M. Zeman, R.A.C.M.M. Van Swaaij, and W.J. Metselaar. Optimization of a-SiGe:H solar cells with graded intrinsic layers using integrated optical and electrical modeling. *Thin Solid Films*, 451-452:294–297, 2004.

[77] F.A. Rubinelli, J.K. Rath, and R.E.I. Schropp. Microcrystalline n-i-p tunnel junction in tandem cells ARTICLES YOU MAY BE INTERESTED IN. *Journal of Applied Physics*, 89:4010, 2001.

[78] M. Tadatsugu. Transparent conducting oxide semiconductors for transparent electrodes. *Semiconductor Science and Technology*, 20(4):S35–S44, apr 2005.

[79] D. Zhang, D. Deligiannis, G. Papakonstantinou, R.A.C.M.M. Van Swaaij, and M. Zeman. Optical enhancement of silicon heterojunction solar cells with hydrogenated amorphous silicon carbide emitter. *IEEE Journal of Photovoltaics*, 4(6):1326–1330, 2014.

A

Appendix A PECVD deposition extra background

Deposition steps PECVD

The deposition by RF PECVD discharge can be divided into four steps [40]:

1. Initially, electron-impact excitation, dissociation and ionization of the precursor gasses generate the primary constituents oft he plasma, in which they react through gas phase reactions.
2. The gas phase reactions are determined by the plasma physics and chemistry. They can be divided into two types of reactions, which conditions define the flux and nature of the reactive species diffusing from the plasma to the substrate: primary reactions, leading to neutral radicals together with ions on the one hand and secondary reactions, leading to higher radicals (species with higher mass than the species of the feed gasses, formed by successive reactions) and nanoclusters on the other hand.
3. Plasma-surface interactions, such as physisorption and chemisorption, diffusion, etching and abstraction by reactive species, define the conditions on the growing surface that result in the film formation. Modification of the growth surface by atomic hydrogen is also part of this process.
4. The final step is the series of reactions taking place in the growing zone. Cross-linking reactions result in the formation of the film and relaxation of the silicon network.

Chemical reactions behind GeH_4

The main chemical reactions taking place in the plasma with Ge_4 are equation A.1 and A.3.

$$\mathbf{e^- + GeH_4 \Rightarrow GeH_3 + H + e^-[80 - 85\%]} \tag{A.1}$$

This product creates a film by:

$$2GeH_3 \Rightarrow (Ge)_f + GeH_4 + H_2 \tag{A.2}$$

The other 15-20% of the chemical reactions, which are taking place is the following:

$$\mathbf{e^- + GeH_4 \Rightarrow GeH_2 + 2H + e^-[15 - 20\%]} \tag{A.3}$$

this product is followed by a reaction with two different products, but the same reactant

$$GeH_2 + GeH_4 \Rightarrow GeH_2H_6 \tag{A.4}$$

$$GeH_2 + GeH_4 \Rightarrow H_3GeGeH + H_2 \tag{A.5}$$

As can be seen by the equations there are 2-body and 3-body reactions. A three-body reaction is a reaction of two species A and B to yield one single product species AB, while 2-body reactions is a reaction of two species which will result in two different products.

Chemical reactions behind SiH_4

The main chemical reactions taking place in the plasma with Si_4 are equation A.6, A.12 and A.14.

$$\mathbf{e^- + SiH_4 \Rightarrow SiH_2 + 2H + e^-[80 - 90\%]} \tag{A.6}$$

This dominant reaction is followed by different possible reactions creating 2 or 3 body reactions. Both the reactions have different products, while having same reactants

$$SiH_2 + SiH_4 \Rightarrow Si_2H_6 \tag{A.7}$$

$$SiH_2 + SiH_4 \Rightarrow H_3SiSiH + H_2 \tag{A.8}$$

The second chemical reactions which takes place from the product of equation A.6 are different. Or the previous two reactions take place, or those three reactions will take place. All of them have the same reactants, but different products.

$$SiH_2 + GeH_4 \Rightarrow SiGeH_6 \tag{A.9}$$

$$SiH_2 + GeH_4 \Rightarrow H_3GeSiH + H_2 \tag{A.10}$$

$$SiH_2 + GeH_4 \Rightarrow H_2GeSiH_2 + H_2 \tag{A.11}$$

As can be seen from equations A.9, A.10 and A.11 two are 2-body reactions and one is a 3-body reaction. The second important main chemical reaction which takes place consist of 0-20%.

$$\mathbf{e^- + SiH_4 \Rightarrow SiH + 2H + H_2 + e^-[0 - 20\%]} \tag{A.12}$$

followed by

$$SiH + GeH_4 \Rightarrow SiGeH_5 \tag{A.13}$$

The third and last chemical reaction related to SiH_4 has the smallest impact, because it covers 10% of the total chemical reactions.

$$\mathbf{e^- + SiH_4 \Rightarrow SiH_3 + H + e^-[< 10\%]} \tag{A.14}$$

creating a film by

$$2SiH_3 \Rightarrow (Si)_f + SiH_4 + H_2 \tag{A.15}$$

The complex H_2GeSiH_2 (A.11) is expected to contribute to growth, while the other products of the 2-body reactions react with SiH_4 or GeH_4 to create higher radicals. Therefore, the growth of a-SiGe:H can be described by considering first the reactions of SiH_4 alone (A.6). When GeH_4 is added, Doyle et al. have observed that Si_2H_6 production (A.7) decreases because the radical SiH_2 preferentially reacts with GeH_4, producing $SiGeH_6$ and H_2GeSiH_2 (reactions A.9 A.11).

The last radical is not very reactive and should reach the substrate, contributing to growth. The efficiency in Si incorporation in the material is thus increased by the addition of GeH_4. On the other hand, most of the H (from all reactions) will react with GeH_4, due to its higher rate constant, explained in coming paragraph, compensating the losses of GeH_3 due to the reaction of GeH_4 with SiH_2. In this way, the efficiency of Ge deposition remains roughly constant [40].

B

Appendix B Material characterization

Figure B.1 displays the three different measured bandgap methods.

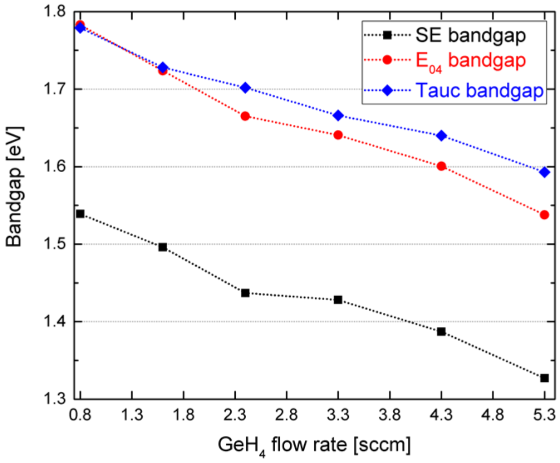

Figure B.1: The effect of variation of GeH_4 flow rate on a-SiGe:H film on three different bandgaps.

Figure B.1 displays the three different measured bandgap methods.

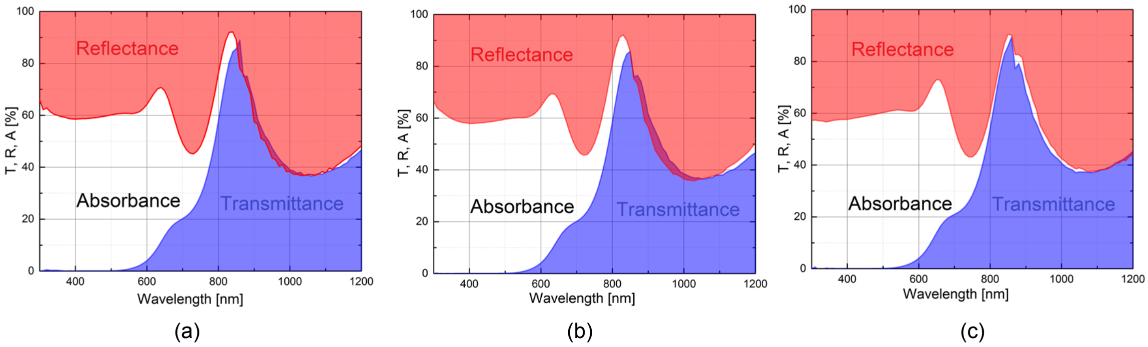

(a) (b) (c)

Figure B.2: Reflectance and transmittance measurements at three different measurement points on one intrinsic layer.

Figure B.2 indicates the transmittance and reflection measurements at three different points in the a-SiGe:H layer. It shows that the layers are not completely uniform and therefore small difference in absorptance can be found in the wavelength ranges from 700 to 900 nm, which is the workable wavelength range. It can be stated that the germanium is deposited by a shower head scattered over the intrinsic layer, which causes a difference in total transmittance, reflectance and absorptance of the layer. However, the differences are in between a range of 5% standard deviation, so therefore the layers are suitable under those deposition conditions.

Figure B.3, B.4 and B.5, B.6, B.7 and B.8 display the different absorption coefficient and activation energy curves for variation of GeH_4 flow rate, SiH_4 flow rate, H_2 flow rate, substrate temperature, deposition power and deposition pressure for a wavelength range from 400 - 1200 nm. The vertical lines display the ranges where Germanium is mostly active.

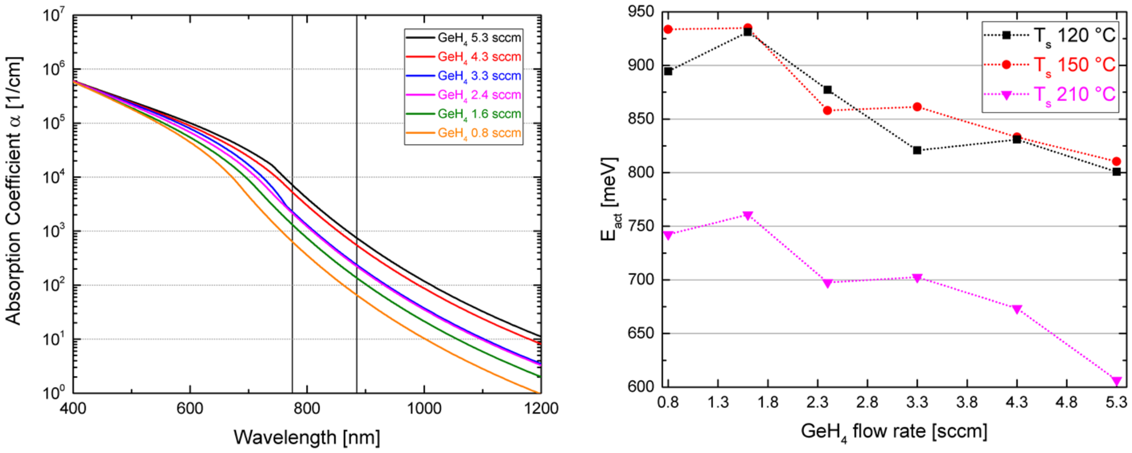

(a) (b)

Figure B.3: The effect of variation of GeH_4 flow rate of a-SiGe:H film on the absorption coefficient **(a)** and the effect of variation of GeH_4 flow rate of a-SiGe:H film on the activation energy **(b)**.

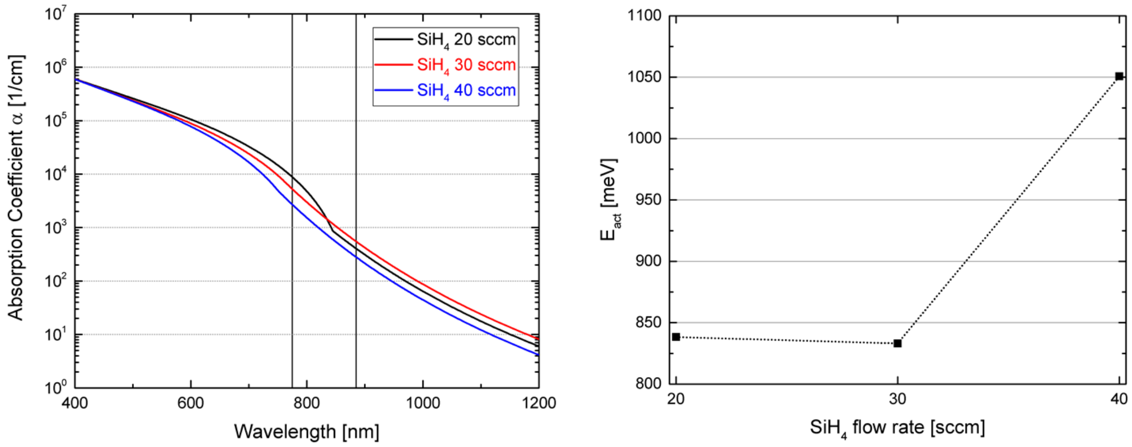

(a) (b)

Figure B.4: The effect of variation of SiH_4 flow rate of a-SiGe:H film on the absorption coefficient **(a)** and the effect of variation of Si_4 flow rate of a-SiGe:H film on the activation energy **(b)**.

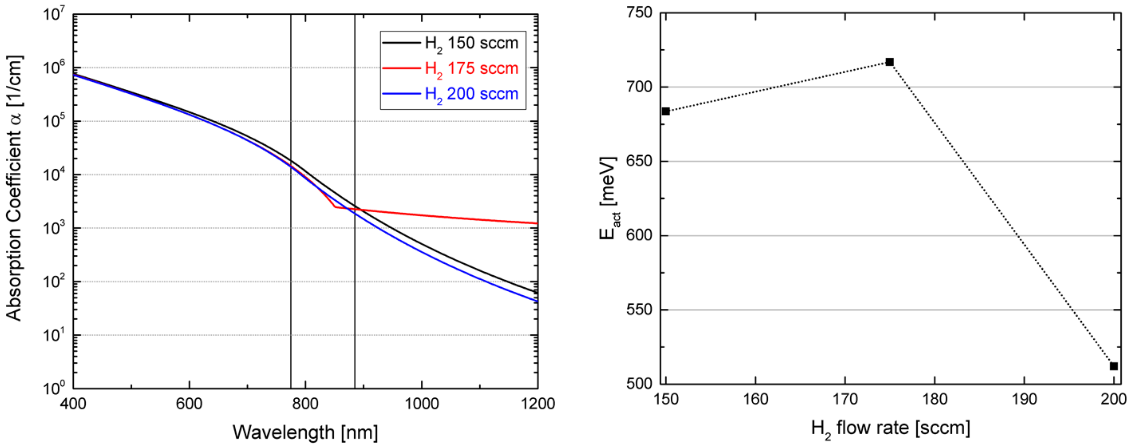

(a) (b)

Figure B.5: The effect of variation of H_2 flow rate of a-SiGe:H film on the absorption coefficient **(a)** and the effect of variation of H_2 of a-SiGe:H film on the activation energy **(b)**.

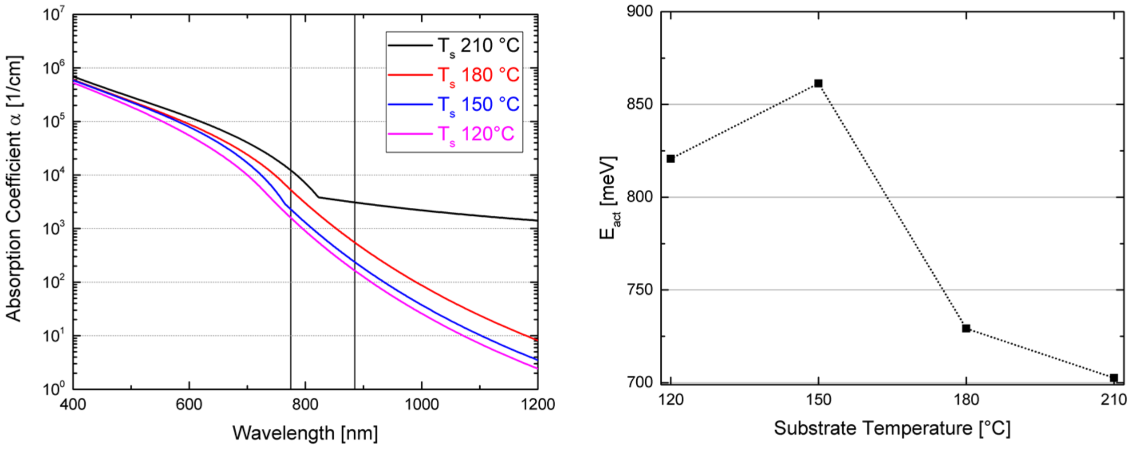

(a) (b)

Figure B.6: The effect of variation of substrate temperature of a-SiGe:H film on the absorption coefficient **(a)** and the effect of variation of substrate temperature of a-SiGe:H film on the activation energy **(b)**.

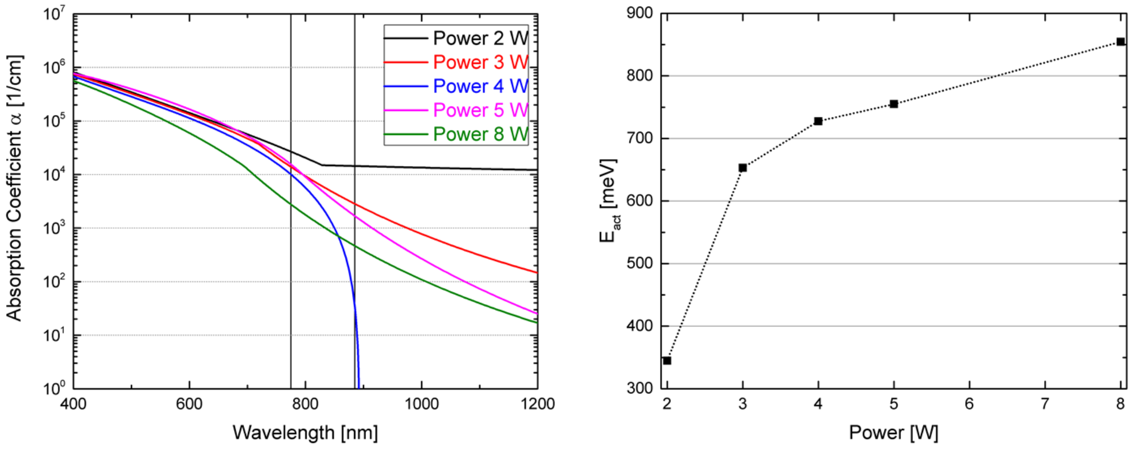

(a) (b)

Figure B.7: The effect of variation of deposition power of a-SiGe:H film on the absorption coefficient **(a)** and the effect of variation of deposition power of a-SiGe:H film on the activation energy **(b)**.

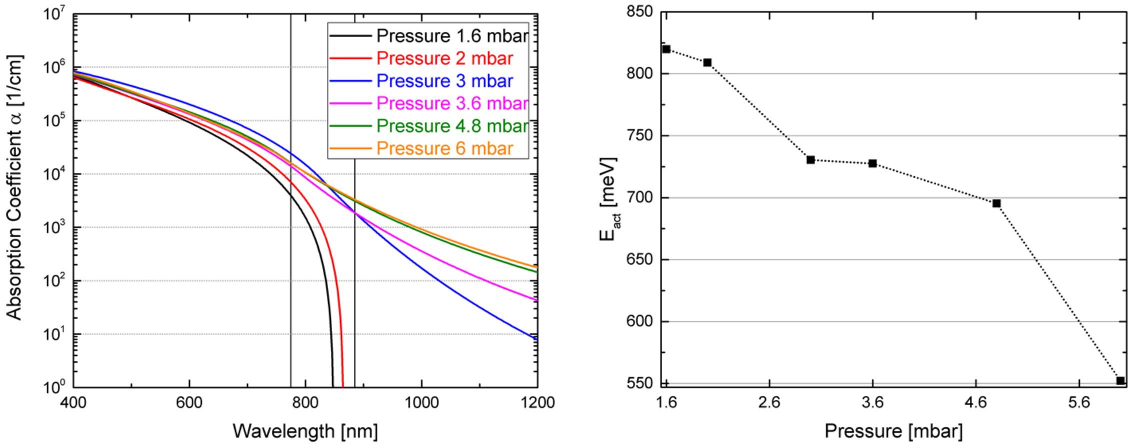

(a) (b)

Figure B.8: The effect of variation of deposition pressure of a-SiGe:H film on the absorption coefficient **(a)** and the effect of variation of deposition pressure of a-SiGe:H film on the activation energy **(b)**.

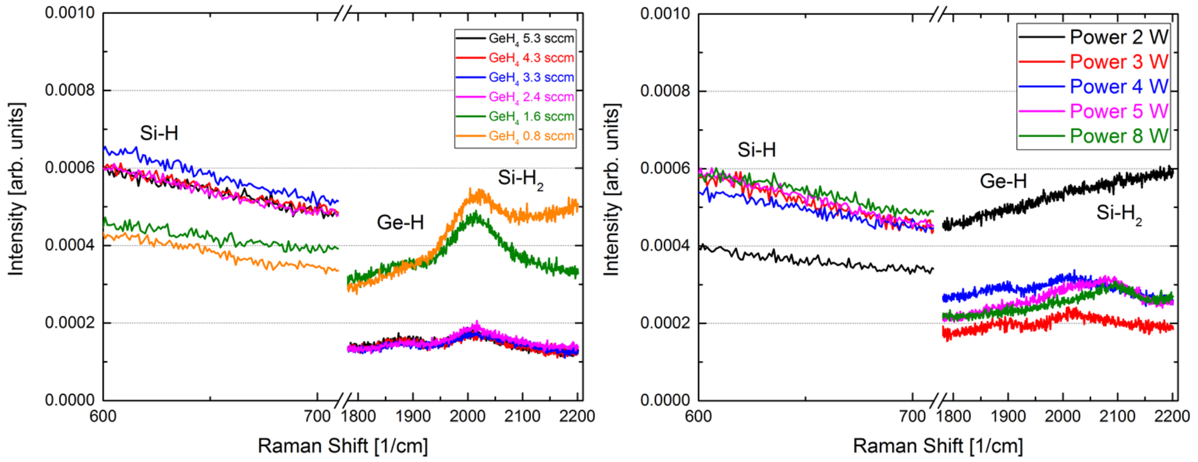

(a)

(b)

Figure B.9: The effect of variation of GeH_4 flow rate of a-SiGe:H film on the stability part of the Raman spectrum **(a)** and the effect of variation of deposition power of a-SiGe:H film on the stability part of the Raman spectrum **(b)**.

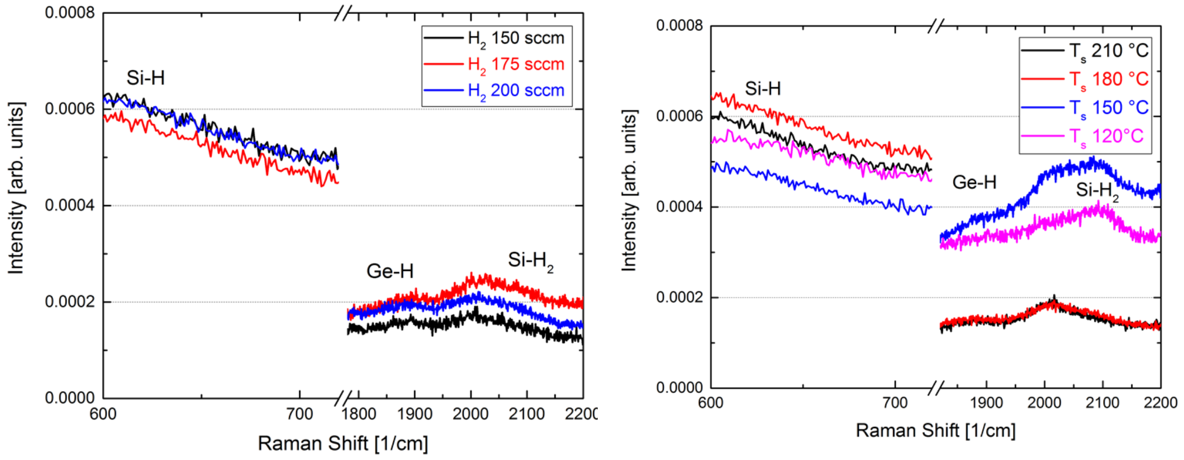

(a)

(b)

Figure B.10: The effect of variation of H_2 flow rate of a-SiGe:H film on the stability part of the Raman spectrum **(a)** and the effect of variation of substrate temperature of a-SiGe:H film on the stability part of the Raman spectrum **(b)**.

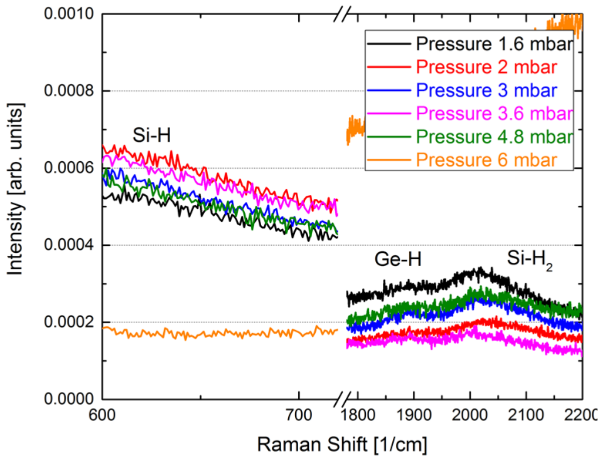

Figure B.11: The effect of variation of deposition pressure of a-SiGe:H film on the stability part of the Raman spectrum

C

Appendix C Single junction solar cell

A difference between front and back TCO is made. Firstly, depositions focusing on the front TCO will be done. As a front TCO both AZO and ITO are proposed.

The TCO is one of the essential components in various state-of-the-art opto-electronic devices. They are used to improve the transport of collected carriers to the external circuit. TCO's are highly electrical conductive materials with comparably low absorption of electromagnetic waves within the active wavelength range of the spectrum. Typically, TCO's use electrode materials that have greater than 80% transmittance of incident light and an electrical conductivity higher than 10^3 S/cm for efficient carrier transport [64]. In general, TCO's for use as thin-film electrodes in solar cells should have a minimum carrier concentration in the order of 10^{20} cm^{-3} for low resistivity and a bandgap greater than 3.2 eV to avoid absorption of light over most of the solar spectra [78].

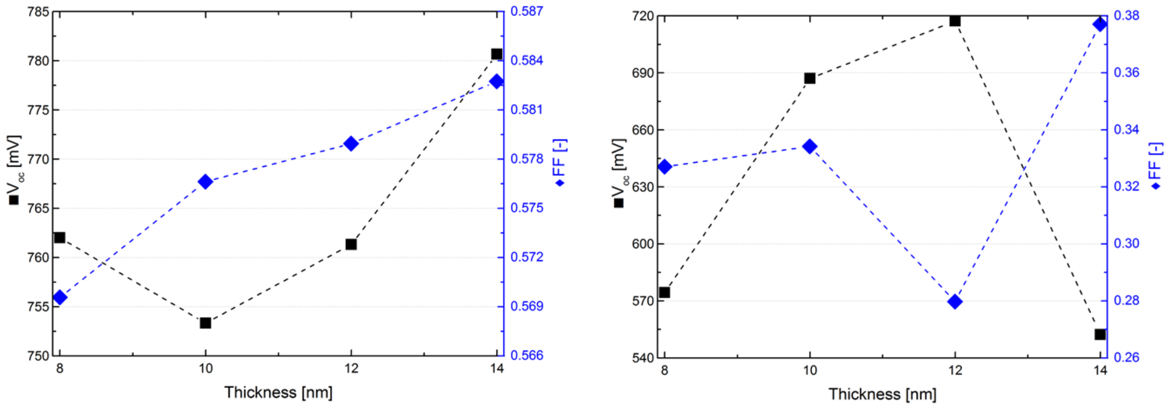

(a) (b)

Figure C.1: The effect of different front TCO's tested by p-SiC layers with ITO **(a)** and AZO **(b)**.

Multiple tests are performed, but only the results from Figure C.1 are displayed in the thesis. Figure C.2 clearly displays that the Corning glass-AZO outperforms the Asahi substrate on both V_{oc} and FF level. However, the J_{sc} of Asahi is higher, due to better light trapping techniques as displayed in Table C.1. The decision is made to further proceed with the Corning glass-AZO combination. This is based on major advantages on V_{oc} and FF level compared to a slightly lower J_{sc}.

It identifies that Corning glass with AZO as a back TCO can be used, because AZO is the most reliable and best performing available TCO and at the back a reliable TCO with high stability is required.

Figure C.3 indicates the earlier mentioned different deposition conditions performed for p-SiC. An optimized carbon content of 45 sccm is chosen, based on previous research conducted by the PVMD group [79].The whole optimization process of p-SiC had several different

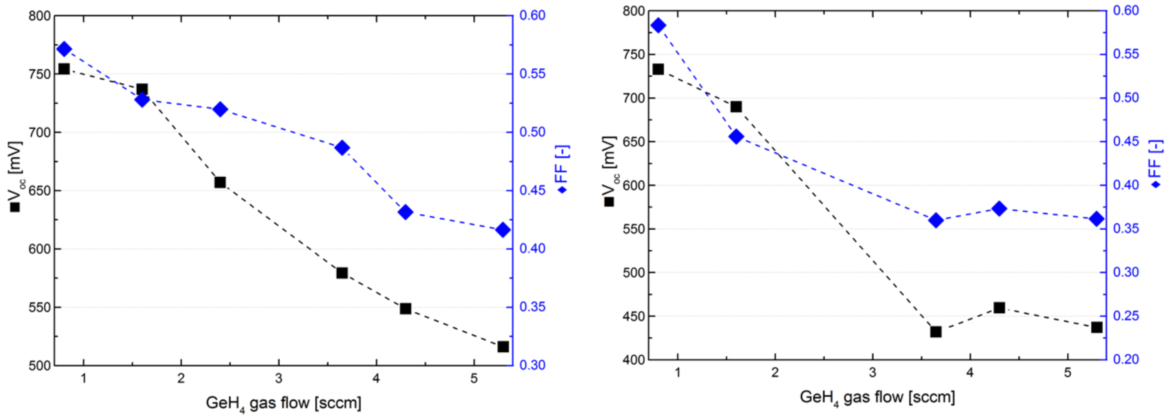

(a)

(b)

Figure C.2: p-SiOx layers with different back TCO's, namely with Corning glass - AZO **(a)** and Asahi glass - thin protective AZO **(b)**.

Table C.1: J_{sc} on different GeH$_4$ flow rate samples on Asahi glass and Corning Glass substrates.

GeH$_4$ flow rate [sccm]	5.3	4.3	3.65	2.4	1.6	0.8
J_{sc}[mA/cm^2] Asahi glass	14.274	15.262	16.547	15.821	15.735	11.544
J_{sc}[mA/cm^2] Corning glass - AZO	13.656	13.423	14.838	11.984	11.563	10.691

steps, namely varying thickness of the p-layer (between 4 and 20 nm), doping concentration (1-5 sccm), pre H$_2$-treatment, post H$_2$ treatment, H$_2$ dilution (0-200 sccm), buffer layer and grading, which was followed by different intrinsic layer thicknesses.

Before going into series of effects of variation of intrinsic layer parameters, optimization of the p-layer based on SiOx:H is done, due to the fact that p-SiOx:H showcased that it outperforms p-SiC. Several different optimization steps are done, based on variation of the layer thickness, the intrinsic i-nc-Si seed layer (without and varied between 1 and 3 nm), H$_2$ dilution, different H$_2$ treatment and ramping schemes of p-SiOx:H, like ramping from p-nc-Si to p-nc-SiOx:H and lastly additional p-nc-Si buffer layer addition.

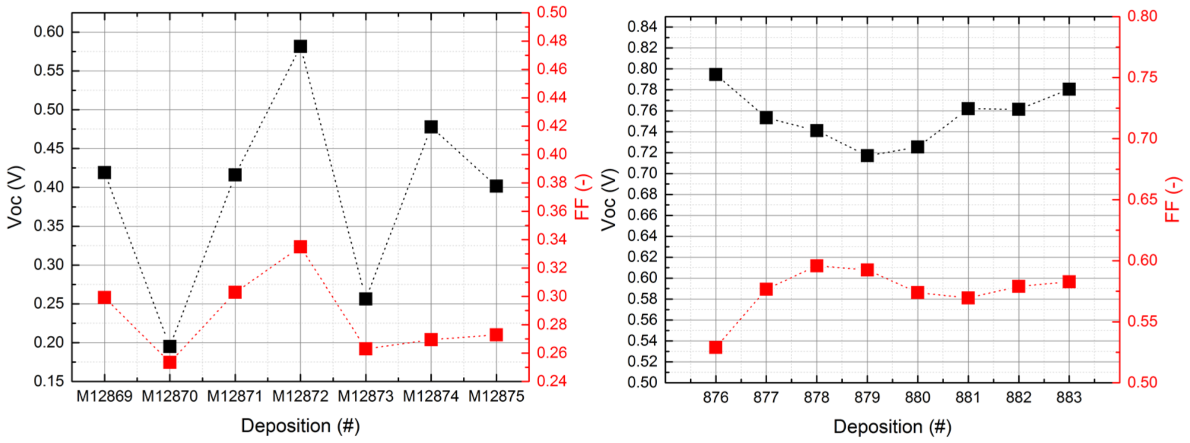

(a)

(b)

Figure C.3: Different deposition conditions first round of p-SiC **(a)** and second round of p-SiC **(b)**.

Due to this effect of AZO on top it is chosen to use ITO as top TCO. Figure C.4 indicates the earlier mentioned favorably of ITO compared to AZO as a front TCO, whereas both FF and

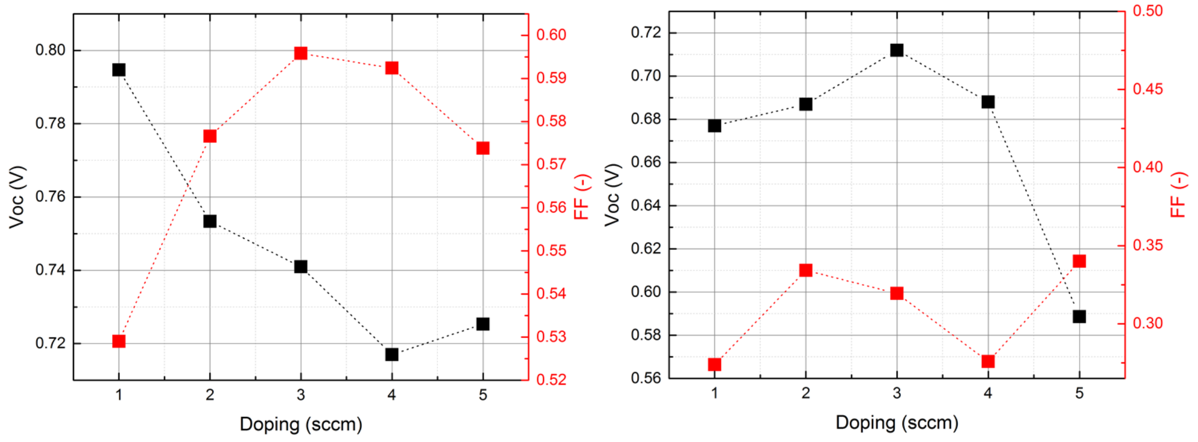

(a) (b)

Figure C.4: p-SiC layers of 10 nm with different Transparant Conductive front Oxides, namely ITO **(a)** and AZO **(b)**.

V_{oc} are way lower than for ITO deposition and even the workability of the cells decreases.

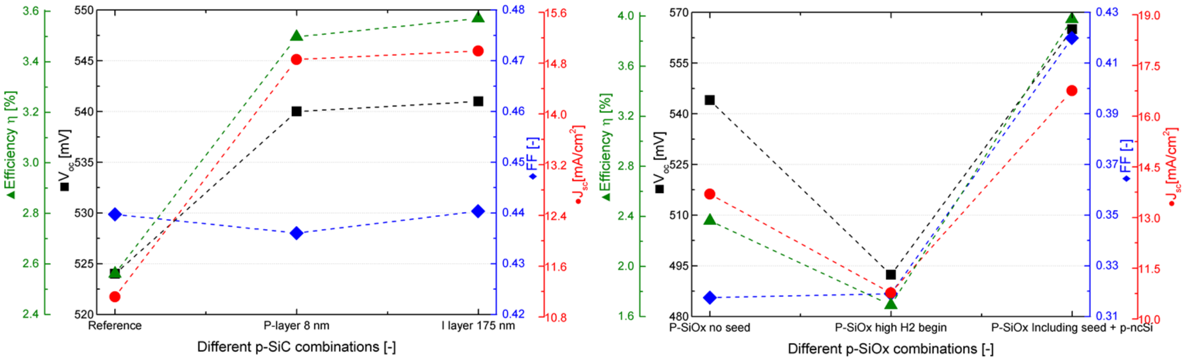

(a) (b)

Figure C.5: The effect of optimized p-SiC on a-SiGe:H solar cell parameters **(a)** and the effect of p-SiOx on solar cell parameters **(b)**.

Different ramping from n-nc-Si to n-SiOx, H_2 dilution, H_2 pre- and post treatment and additional 2 nm n-a-Si buffer layer.

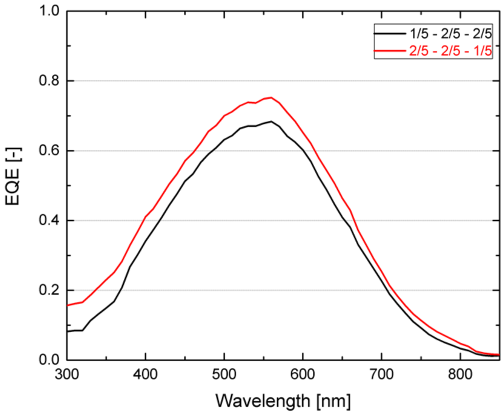

Figure C.6: The E-shape grading EQE graph

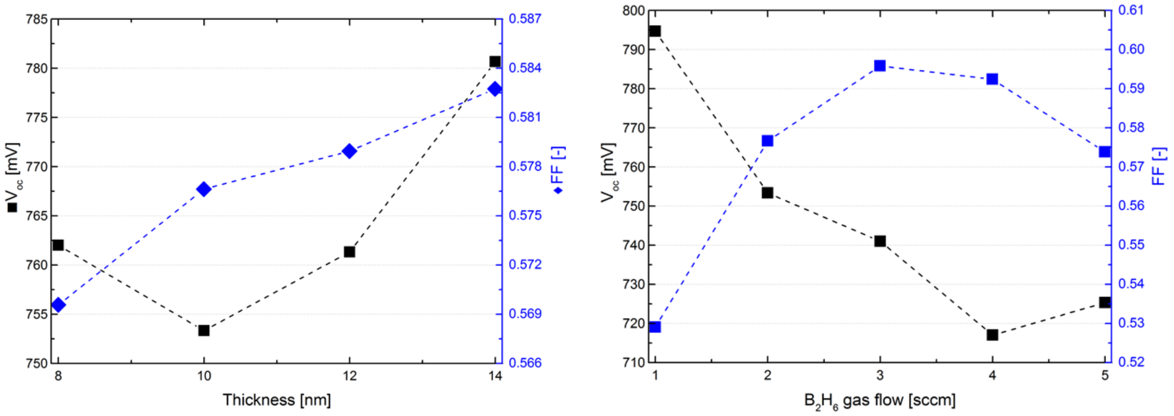

(a) (b)

Figure C.7: Voc and FF of p-SiC layers with variation of thickness **(a)** and variation of doping concentration **(b)**.

Figure C.7 displays the different p-SiC series under variation of doping concentration and thickness change. Firstly different H_2 conditions, big thickness changes and H_2 treatments are performed which indicated a thickness around 10 nm as best performer and therefore steps are reduced and doping levels of the p-layer are changed around a thickness of 10 nm.

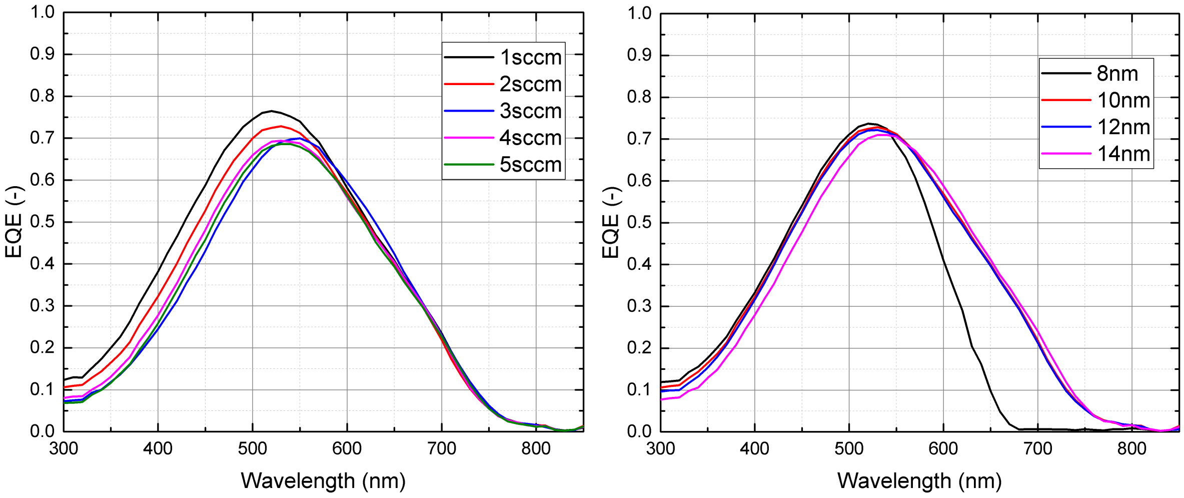

(a) (b)

Figure C.8: EQE of p-SiC layers as a function different doping concentration **(a)** and function of different thickness **(b)**.

Figure C.8 exposes the effects of p-SiC deposition with ITO as front TCO with different thickness and different doping parameters for the p-SiC layer. This figure displays that the smaller the doping gas flow rate the higher the response in shorter wavelength regions. While a thinner layer clearly shows that more recombination can be found in the cell bulk and rear plus more light will be unabsorbed. This will decrease the spectral response and generate a lower final current density.

D

Appendix D LID and refractive index background

Table D.1: The effect of Light Induced Degradation under different GeH_4 flow rate conditions on the V_{oc} in mV.

Time [hours]	**GeH_4 5.3** [sccm]	**GeH_4 4.3** [sccm]	**GeH_4 3.65** [sccm]	**GeH_4 2.4** [sccm]	**GeH_4 1.6** [sccm]	**GeH_4 0.8** [sccm]
0	515.3	543.7	584.2	651.9	741.2	760.5
15	515.0	540.6	580.5	637.0	701.7	709.0
24	514.0	540.4	576.3	631.3	694.6	703.3
48	514.0	535.7	556.0	618.8	681.6	686.7
250	495.3	513.0	522.3	579.2	640.8	648.0
500	479.6	485.4	505.7	561.0	619.7	623.8
1000	468.3	484.7	496.6	551.0	603.6	609.5

Table D.2: The relative effect of Light Induced Degradation under different GeH_4 flow rate conditions on the V_{oc} in %.

Time [hours]	**GeH_4 5.3** [sccm]	**GeH_4 4.3** [sccm]	**GeH_4 3.65** [sccm]	**GeH_4 2.4** [sccm]	**GeH_4 1.6** [sccm]	**GeH_4 0.8** [sccm]
0	0%	0%	0%	0%	0%	0%
15	-0.1%	-0.6%	-0.6%	-2.3%	-5.3%	-6.8%
24	-0.2%	-0.6%	-1.4%	-3.2%	-6.3%	-7.5%
48	-0.2%	-1.5%	-4.8%	-5.1%	-8.0%	-9.7%
250	-3.9%	-5.6%	-10.6%	-11.1%	-13.5%	-14.8%
500	-6.9%	-10.7%	-13.4%	-13.9%	-16.4%	-18.0%
1000	-9.1%	-10.9%	-15.0%	-15.5%	-18.6%	-19.9%

Table D.3: The effect of Light Induced Degradation under different GeH_4 flow rate conditions on the FF.

Time [hours]	**GeH_4 5.3** [sccm]	**GeH_4 4.3** [sccm]	**GeH_4 3.65** [sccm]	**GeH_4 2.4** [sccm]	**GeH_4 1.6** [sccm]	**GeH_4 0.8** [sccm]
0	0.410	0.367	0.432	0.466	0.522	0.548
15	0.343	0.324	0.377	0.398	0.433	0.477
24	0.331	0.318	0.366	0.387	0.419	0.463
48	0.296	0.305	0.336	0.352	0.384	0.431
250	0.256	0.276	0.275	0.291	0.316	0.334
500	0.254	0.269	0.272	0.284	0.305	0.320
1000	0.253	0.269	0.268	0.279	0.298	0.312

Table D.4: The relative effect of Light Induced Degradation under different GeH_4 flow rate conditions on the FF in %.

Time	**GeH_4 5.3**	**GeH_4 4.3**	**GeH_4 3.65**	**GeH_4 2.4**	**GeH_4 1.6**	**GeH_4 0.8**
[hours]	[sccm]	[sccm]	[sccm]	[sccm]	[sccm]	[sccm]
0	0%	0%	0%	0%	0%	0%
15	-16.3%	-11.9%	-12.7%	-14.6%	-17.1%	-12.9%
24	-19.3%	-13.5%	-15.3%	-16.9%	-19.8%	-15.5%
48	-27.6%	-17.1%	-22.2%	-24.6%	-26.5%	-21.4%
250	-37.5%	-25.0%	-36.2%	-37.6%	-39.5%	-39.1%
500	-37.9%	-26.6%	-37.1%	-39.0%	-41.6%	-41.6%
1000	-38.2%	-26.7%	-37.9%	-40.2%	-42.9%	-43.0%

Table D.5: The Refractive index (n) data for a wavelength from 500 - 715 nm of different GeH_4 flow rate.

GeH_4	**1.6**	**2.4**	**3.3**	**4.3**	**5.3**	**GeH_4**	**1.6**	**2.4**	**3.3**	**4.3**	**5.3**
nm	**n**	**n**	**n**	**n**	**n**	**nm**	**n**	**n**	**n**	**n**	**n**
500	4.83	4.80	4.84	4.85	4.85	612	4.55	4.59	4.67	4.73	4.77
504	4.83	4.80	4.84	4.85	4.85	615	4.54	4.58	4.67	4.73	4.77
507	4.82	4.80	4.83	4.85	4.85	618	4.53	4.57	4.66	4.72	4.76
510	4.82	4.80	4.83	4.85	4.85	621	4.52	4.56	4.65	4.71	4.76
513	4.81	4.79	4.83	4.85	4.85	624	4.51	4.55	4.64	4.71	4.75
516	4.80	4.79	4.83	4.85	4.85	627	4.50	4.54	4.63	4.70	4.74
519	4.80	4.78	4.83	4.85	4.85	631	4.49	4.53	4.63	4.69	4.74
521	4.79	4.78	4.83	4.85	4.85	634	4.48	4.53	4.62	4.69	4.73
523	4.79	4.78	4.82	4.85	4.85	637	4.47	4.52	4.61	4.68	4.73
524	4.79	4.78	4.82	4.85	4.85	640	4.46	4.51	4.60	4.67	4.72
526	4.78	4.78	4.82	4.85	4.85	643	4.45	4.50	4.59	4.67	4.72
527	4.78	4.77	4.82	4.85	4.85	646	4.44	4.49	4.59	4.66	4.71
529	4.78	4.77	4.82	4.85	4.85	650	4.43	4.48	4.58	4.65	4.70
531	4.77	4.77	4.82	4.85	4.85	653	4.42	4.47	4.57	4.64	4.70
534	4.77	4.76	4.81	4.84	4.85	656	4.41	4.46	4.56	4.64	4.69
537	4.76	4.76	4.81	4.84	4.85	659	4.40	4.45	4.55	4.63	4.68
540	4.75	4.75	4.81	4.84	4.85	662	4.39	4.44	4.54	4.62	4.68
543	4.74	4.75	4.80	4.84	4.85	665	4.38	4.43	4.54	4.61	4.67
546	4.74	4.74	4.80	4.83	4.85	669	4.37	4.43	4.53	4.61	4.66
550	4.73	4.73	4.79	4.83	4.84	672	4.36	4.42	4.52	4.60	4.66
553	4.72	4.73	4.79	4.83	4.84	675	4.35	4.41	4.51	4.59	4.65
556	4.71	4.72	4.78	4.82	4.84	677	4.34	4.40	4.51	4.59	4.65
559	4.70	4.71	4.78	4.82	4.84	678	4.34	4.40	4.50	4.58	4.64
562	4.69	4.71	4.77	4.82	4.83	680	4.34	4.39	4.50	4.58	4.64
565	4.68	4.70	4.77	4.81	4.83	681	4.33	4.39	4.49	4.58	4.64
569	4.68	4.69	4.76	4.81	4.83	683	4.33	4.38	4.49	4.57	4.63
572	4.67	4.69	4.76	4.80	4.83	684	4.32	4.38	4.48	4.57	4.63
575	4.66	4.68	4.75	4.80	4.82	686	4.32	4.37	4.48	4.56	4.62
578	4.65	4.67	4.74	4.79	4.82	689	4.31	4.37	4.47	4.56	4.62
581	4.64	4.66	4.74	4.79	4.81	692	4.30	4.36	4.46	4.55	4.61
585	4.63	4.66	4.73	4.78	4.81	696	4.29	4.35	4.45	4.54	4.60
588	4.62	4.65	4.72	4.78	4.81	699	4.28	4.34	4.45	4.53	4.60
591	4.61	4.64	4.72	4.77	4.80	702	4.27	4.33	4.44	4.52	4.59
594	4.60	4.63	4.71	4.77	4.80	705	4.26	4.32	4.43	4.52	4.58
597	4.59	4.62	4.70	4.76	4.79	708	4.25	4.31	4.42	4.51	4.57
599	4.59	4.62	4.70	4.76	4.79	711	4.24	4.30	4.41	4.50	4.57
600	4.58	4.62	4.70	4.76	4.79	715	4.23	4.29	4.40	4.49	4.56

E

Appendix E Genpro simulations

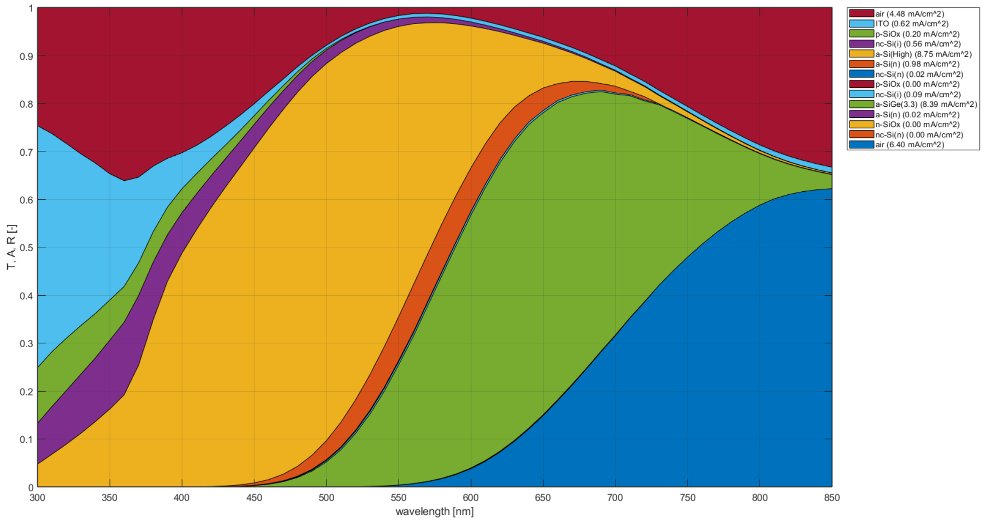

Figure E.1: Simulation results from Genpro for V-shape tandem cells

Figure E.1 shows the Genpro simulations with a thickness of 150 nm a-Si:H for the top cell and a thickness of 200 nm for the a-SiGe:H bottom cell with a V-shape.

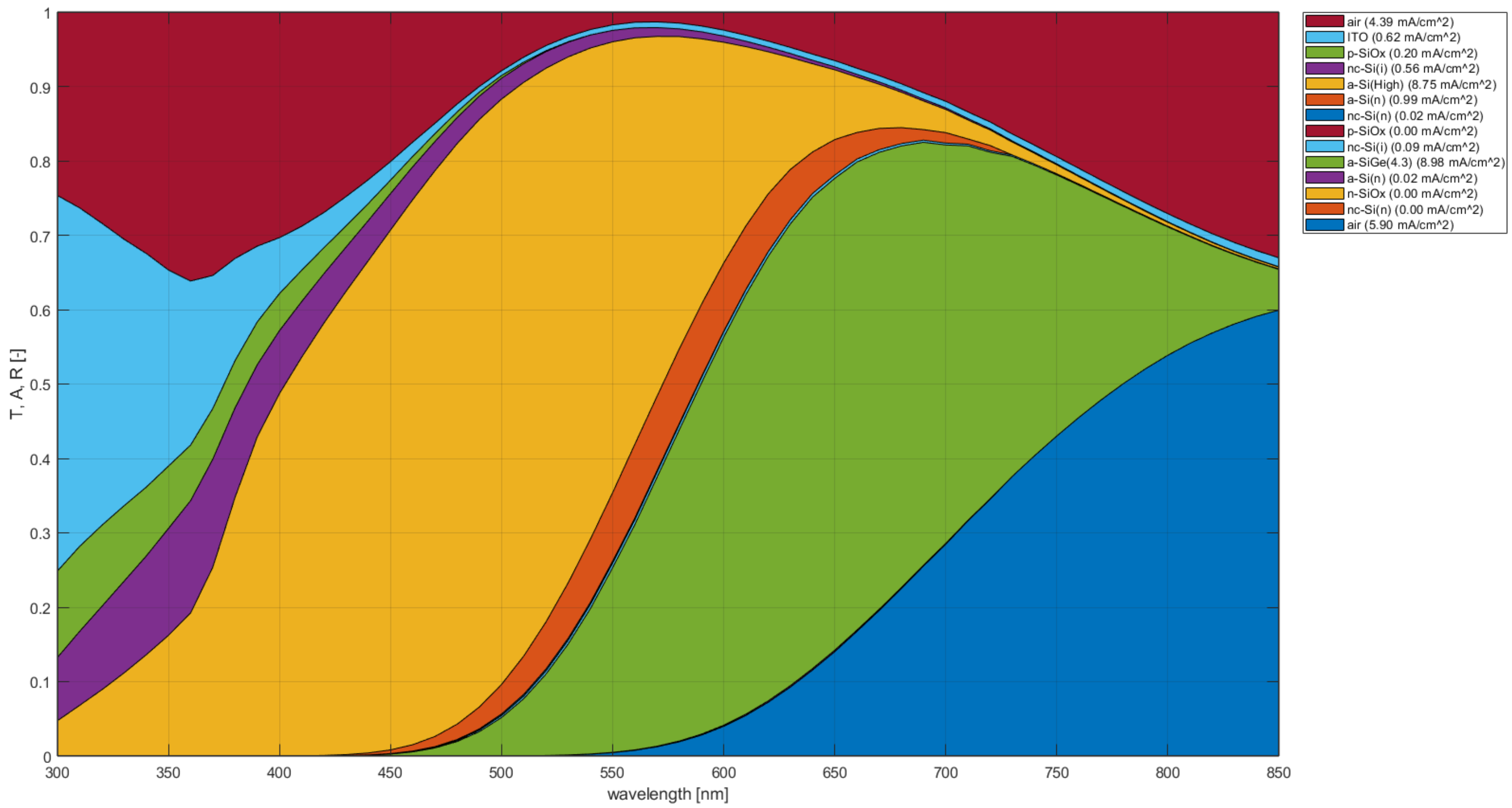

Figure E.2: Simulation results from Genpro for U-shape tandem cells

Figure E.2 shows the Genpro simulations with a thickness of 150 nm a-Si:H for the top cell and a thickness of 170 nm for the a-SiGe:H bottom cell with a U-shape.

F

Appendix F Logbook depositions

F.1. p-SiC logbook

Table F.1: The logbook of a p-SiC series with i-a-Si with SiH_4 of 20 sccm, a CH_4 of 45 sccm, temperature of 300°C with ITO as front TCO on Asahi glass.

pSiC first Round SiH_4=20, CH_4=45,T=300 constant, ITO										Solar Cell Parameters												
										Isc:	Voc:	Impp:	Vmpp:	Jsc :	Rs :	Rsh:	Fill factor:	Eff:	Voc x FF	Voc	Jsc :	Corrected Eff:
SI No.	Dep. No.	AZO/Asahi	Description	Date	B_2H_6 [sccm]	H_2 [sccm]	Pressure [mbar]	Power [W]	Time [s]	[A]	[V]	[A]	[V]	[A/m^2]	[Ωm^2]	[Ωm^2]	[%]	[%]	[-]	[mV]	[mA/cm^2]	[%]
1	M12869	Asahi	20 nm p-SiC	25/04/2019	2	0	0.7	2.5	130	-0.002	0.42	-0.001	0.24	-72.28	32.64	317.22	0.30	0.93%	0.13	419.000		
2	M12870	Asahi	20 nm p-SiC	25/04/2019	4	0	0.7	2.5	130	-0.002	0.20	-0.001	0.09	-70.36	19.84	116.42	0.25	0.35%	0.05	195.000		
3	M12871	Asahi	10nm p-SiC	25/04/2019	2	0	0.7	2.5	70	-0.002	0.42	-0.001	0.24	-75.73	24.37	299.98	0.30	1.05%	0.13	416.000		
4	M12872	Asahi	20nm p-SiC	25/04/2019	2	40	0.7	2.5	180	-0.002	0.58	-0.001	0.33	-95.10	57.26	445.49	0.33	1.86%	0.20	581.667		
5	M12873	Asahi	20nm p-SiC	25/04/2019	2	0	0.7	2.5	130	-0.002	0.26	-0.001	0.13	-95.19	39.33	116.46	0.26	0.65%	0.07	256.333		
6	M12874	Asahi	20nm p-SiC	25/04/2019	2	40	0.7	2.5	180	-0.003	0.48	-0.001	0.25	-105.13	49.77	205.16	0.27	1.36%	0.13	478.000		
7	M12875	Asahi	20nm p-SiC	25/04/2019	2	0	0.7	2.5	130	-0.003	0.40	-0.002	0.20	-108.74	40.09	174.25	0.27	1.20%	0.11	401.500		

Table F.2: The logbook of a p-SiC series with different thickness and doping with i-a-Si with SiH_4 of 20 sccm, a CH_4 of 45 sccm, temperature of 300°C with ITO as front TCO on Asahi glass.

a-Si + pSiC SiH_4=20, CH_4=45,T=300 constant, ITO										Solar Cell Parameters												
										Isc:	Voc:	Impp:	Vmpp:	Jsc :	Rs :	Rsh:	Fill factor:	Eff:	Voc x FF	Voc	Jsc :	Corrected Eff:
SI No.	Dep. No.	AZO/Asahi	Description	Date	B_2H_6 [sccm]	H_2 [sccm]	Pressure [mbar]	Power [W]	Time [s]	[A]	[V]	[A]	[V]	[A/m^2]	[Ωm^2]	[Ωm^2]	[%]	[%]	[-]	[mV]	[mA/cm^2]	[%]
1	M12876	ITO	10nm p-SiC	27/04/2019	1	0	0.7	2.5	70	-0.003	0.79	-0.002	0.57	-11.34	52.40	1499.51	0.53	0.48%	0.42	794.667	11.73481	4.93%
2	M12877	ITO	10nm p-SiC	27/04/2019	2	0	0.7	2.5	70	-0.002	0.75	-0.002	0.60	-87.57	26.59	2055.47	0.58	3.80%	0.43	753.333	11.09151	4.82%
3	M12878	ITO	10nm p-SiC	27/04/2019	3	0	0.7	2.5	70	-0.002	0.74	-0.001	0.60	-78.33	17.80	2260.90	0.60	3.46%	0.44	741.000	10.66632	4.71%
4	M12879	ITO	10nm p-SiC	27/04/2019	4	0	0.7	2.5	70	-0.002	0.72	-0.001	0.56	-78.71	14.60	2094.92	0.59	3.34%	0.42	717.000	10.66642	4.53%
5	M12880	ITO	10nm p-SiC	27/04/2019	5	0	0.7	2.5	70	-0.002	0.73	-0.002	0.56	-89.60	20.98	1787.18	0.57	3.73%	0.42	725.333	10.47572	4.36%
6	M12881	ITO	8nm p-SiC	27/04/2019	2	0	0.7	2.5	56	-0.002	0.76	-0.002	0.60	-96.50	24.86	1784.69	0.57	4.19%	0.43	762.000	8.517754	3.70%
7	M12882	ITO	12nm p-SiC	27/04/2019	2	0	0.7	2.5	84	-0.002	0.76	-0.002	0.60	-92.58	24.76	1972.37	0.58	4.08%	0.44	761.333	10.95579	4.83%
8	M12883	ITO	14nm p-SiC	27/04/2019	2	0	0.7	2.5	98	-0.002	0.78	-0.002	0.61	-96.26	19.30	1818.49	0.58	4.38%	0.45	780.667	10.91267	4.96%

Table F.3: The logbook of a p-SiC series with different thickness and doping with i-a-Si with SiH_4 of 20 sccm, a CH_4 of 45 sccm, temperature of 300°C with AZO as front TCO on Asahi glass.

Different na-Si + pSiC SiH_4=20, CH_4=45,T=300 constant, AZO										Solar Cell Parameters												
										Isc:	Voc:	Impp:	Vmpp:	Jsc :	Rs :	Rsh:	Fill factor:	Eff:	Voc x FF	Voc	Jsc :	Corrected Eff:
SI No.	Dep. No.	AZO/Asahi	Description	Date	B_2H_6 [sccm]	H_2 [sccm]	Pressure [mbar]	Power [W]	Time [s]	[A]	[V]	[A]	[V]	[A/m^2]	[Ωm^2]	[Ωm^2]	[%]	[%]	[-]	[mV]	[mA/cm^2]	[%]
1	M12892	AZO	10nm p-SiC	27/04/2019	1	0	0.7	2.5	70	-0.003	0.68	-0.002	0.28	-105.75	485.51	574.26	0.27	1.96%	0.19	677.000		
2	M12893	AZO	10nm p-SiC	27/04/2019	2	0	0.7	2.5	70	-0.004	0.69	-0.002	0.35	-137.46	115.11	545.40	0.33	3.13%	0.23	687.000		
3	M12894	AZO	10nm p-SiC	27/04/2019	3	0	0.7	2.5	70	-0.002	0.71	-0.001	0.33	-76.93	197.92	1050.40	0.32	1.74%	0.23	712.000		
4	M12895	AZO	10nm p-SiC	27/04/2019	4	0	0.7	2.5	70	-0.002	0.69	-0.001	0.31	-65.93	198.94	869.38	0.28	1.25%	0.19	688.000		
5	M12896	AZO	10nm p-SiC	27/04/2019	5	0	0.7	2.5	70		0.59						0.34		0.20	588.667		
6	M12897	AZO	8nm p-SiC	27/04/2019	2	0	0.7	2.5	56	-0.002	0.57	-0.001	0.28	-75.91	405.69	765.79	0.33	1.42%	0.19	574.333		
7	M12898	AZO	12nm p-SiC	27/04/2019	2	0	0.7	2.5	84	-0.002	0.72	-0.001	0.28	-79.51	188.42	931.89	0.28	1.60%	0.20	717.333		
8	M12899	AZO	14nm p-SiC	27/04/2019	2	0	0.7	2.5	98	-0.002	0.55	-0.001	0.31	-79.91	117.53	748.17	0.38	1.66%	0.21	552.333		

Table F.4: The logbook of a p-SiC series with different H_2 treatment with i-a-Si with SiH_4 of 20 sccm, a CH_4 of 45 sccm, temperature of 300°C with ITO as front TCO on Asahi glass.

a-Si + pSiC SiH_4=20, CH_4=45,T=300 constant, ITO										Solar Cell Parameters												
										Isc:	Voc:	Impp:	Vmpp:	Jsc :	Rs :	Rsh:	Fill factor:	Eff:	Voc x FF	Voc	Jsc :	Corrected Eff:
SI No.	Dep. No.	AZO/Asahi	Description	Date	B_2H_6 [sccm]	H_2 [sccm]	Pressure [mbar]	Power [W]	Time [s]	[A]	[V]	[A]	[V]	[A/m^2]	[Ωm^2]	[Ωm^2]	[%]	[%]	[-]	[mV]	[mA/cm^2]	[%]
1	M12950	ITO	12nm p-SiC H_2-0	07/05/2019	2.5	0	0.7	2.5	75	-0.003	0.74	-0.002	0.52	-119.64	33.58	847.51	0.46	4.13%	0.34	742.667	10.68737	3.69%
2	M12951	ITO	12nm p-SiC H_2-15	07/05/2019	2.5	15	0.7	2.5	83	-0.003	0.75	-0.002	0.53	-111.16	21.94	690.71	0.42	3.52%	0.32	747.667	10.565	3.35%
3	M12952	ITO	12nm p-SiC H_2-30	07/05/2019	2.5	30	0.7	2.5	92	-0.003	0.76	-0.002	0.60	-105.49	14.98	1622.89	0.58	4.65%	0.44	757.333	9.867465	4.35%
4	M12953	ITO	12nm p-SiC H_2-45	07/05/2019	2.5	45	0.7	2.5	103	-0.002	0.77	-0.002	0.60	-93.33	19.58	1791.32	0.57	4.07%	0.44	766.667	10.63097	4.64%
5	M12954	ITO	12nm p-SiC H_2-60	07/05/2019	2.5	60	0.7	2.5	118	-0.003	0.77	-0.002	0.59	-112.16	28.78	1531.93	0.55	4.79%	0.43	769.667	10.14514	4.33%

Table F.5: The logbook of a p-SiC series with first i-a-SiGe:H intrinsic layer consisting of different buffers with SiH_4 of 20 sccm, a CH_4 of 45 sccm, temperature of 300°C with ITO as front TCO on both Corning glass - AZO and Asahi glass combination.

a-SiGe:H — SiH_4=20, B_2H_6=2, T=250										Solar Cell Parameters												
										Isc:	Voc:	Impp:	Vmpp:	Jsc :	Rs :	Rsh:	Fill factor:	Eff:	Voc x FF	Voc	Jsc :	Corrected Eff:
SI No.	Dep. No.	AZO/Asahi	Description	Date	GeH_4 [sccm]	H_2 [sccm]	Pressure [mbar]	Power [W]	Time [s]	[A]	[V]	[A]	[V]	[A/m^2]	[Ωm^2]	[Ωm^2]	[%]	[%]	[-]	[mV]	[mA/cm^2]	[%]
1	M12955	Asahi	a-SiGe4.3	08/05/2019	4.3	200	3.6	4	700	-0.002	0.48	-0.001	0.29	-63.56	22.04	595.97	0.36	1.08%	0.17	477.500		
2	M12956	Asahi	a-SiGe4.3 i/p buffer (chamber 3)	08/05/2019	4.3	200	3.6	4	700	SHUNTED	SHUNTED	SHUNTED	SHUNTED	SHUNTED	SHUNTED	SHUNTED	SHUNTED	SHUNTED	SHUNTED	SHUNTED	SHUNTED	SHUNTED
3	M12957	Asahi	a-SiGe4.3 i/p buffer (chamber 5)	08/05/2019	4.3	200	3.6	4	700	SHUNTED	SHUNTED	SHUNTED	SHUNTED	SHUNTED	SHUNTED	SHUNTED	SHUNTED	SHUNTED	SHUNTED	SHUNTED	SHUNTED	SHUNTED
4	M12958	Asahi	a-SiGe4.3 n-i + i-p buffer (chamber 5)	08/05/2019	4.3	200	3.6	4	700	SHUNTED	SHUNTED	SHUNTED	SHUNTED	SHUNTED	SHUNTED	SHUNTED	SHUNTED	SHUNTED	SHUNTED	SHUNTED	SHUNTED	SHUNTED
5	M12959	Asahi	p-layer change 19nm +(i/p buffer)	08/05/2019	4.3	200	3.6	4	800	SHUNTED	SHUNTED	SHUNTED	SHUNTED	SHUNTED	SHUNTED	SHUNTED	SHUNTED	SHUNTED	SHUNTED	SHUNTED	SHUNTED	SHUNTED
6	M12964	AZO	a-SiGe4.3	08/05/2019	4.3	200	3.6	4	700	SHUNTED	SHUNTED	SHUNTED	SHUNTED	SHUNTED	SHUNTED	SHUNTED	SHUNTED	SHUNTED	SHUNTED	SHUNTED	SHUNTED	SHUNTED
7	M12965	AZO	a-SiGe4.3 i/p buffer (chamber 3)	08/05/2019	4.3	200	3.6	4	700	SHUNTED	SHUNTED	SHUNTED	SHUNTED	SHUNTED	SHUNTED	SHUNTED	SHUNTED	SHUNTED	SHUNTED	SHUNTED	SHUNTED	SHUNTED
8	M12972	AZO	a-SiGe4.3 i/p buffer (chamber 5)	08/05/2019	4.3	200	3.6	4	700	-0.003	0.44	-0.002	0.26	-117.34	21.50	270.44	0.34	1.75%	0.15	444.000		
9	M12973	AZO	a-SiGe4.3 n-i + i-p buffer (chamber 5)	08/05/2019	4.3	200	3.6	4	700	SHUNTED	SHUNTED	SHUNTED	SHUNTED	SHUNTED	SHUNTED	SHUNTED	SHUNTED	SHUNTED	SHUNTED	SHUNTED	SHUNTED	SHUNTED
10	M12974	AZO	p-layer change 19nm +(i/p buffer)	08/05/2019	4.3	200	3.6	4	800	SHUNTED	SHUNTED	SHUNTED	SHUNTED	SHUNTED	SHUNTED	SHUNTED	SHUNTED	SHUNTED	SHUNTED	SHUNTED	SHUNTED	SHUNTED

Table F.6: The logbook of a p-SiC series with i-a-SiGe:H intrinsic layer consisting of new grading schemes, variation of p and n layers, with SiH_4 of 20 sccm, a CH_4 of 45 sccm, temperature of 300°C with ITO as front TCO on both Corning glass - AZO and Asahi glass combination.

a-SiGe:H grading Fai Ton Style										Solar Cell Parameters												
										Isc:	Voc:	Impp:	Vmpp:	Jsc :	Rs :	Rsh:	Fill factor:	Eff:	Voc x FF	Voc	Jsc :	Corrected Eff:
Sl No.	Dep. No.	AZO/Asahi	Description	Date	GeH_4 [sccm]	n/i [s]	i-i[s]	i-p[s]	I thickness [nm]	[A]	[V]	[A]	[V]	[A/m^2]	[Ωm^2]	[Ωm^2]	[%]	[%]	[-]	[mV]	[mA/cm^2]	[%]
1	M12995	Asahi	Reversed Grading Scheme (new standard)	14/05/2019	4.3	179	271	253	150	-0.003	0.52	-0.002	0.33	-133.70	14.02	485.53	0.42	2.90%	0.22	518.333		
2	M12996	AZO	Reversed Grading Scheme (new standard)	14/05/2019	4.3	179	271	253	150	-0.003	0.51	-0.002	0.32	-99.71	21.13	521.65	0.39	1.96%	0.20	507.667		
3	M12997	Asahi	Ge2.4	14/05/2019	2.4	179	271	253	150	-0.003	0.66	-0.002	0.48	-127.05	18.27	1317.18	0.54	4.55%	0.36	661.000		
4	M12998	Asahi	40s extra in last (i-p) GeH_4 step	14/05/2019	4.3	179	271	293	159	-0.003	0.52	-0.002	0.33	-121.79	16.82	579.63	0.43	2.68%	0.22	515.333		
5	M12999	Asahi	extra 40s line added a-Si	14/05/2019	4.3	179	271	253	150+i-a-Si	-0.003	0.51	-0.002	0.33	-110.58	15.80	716.81	0.45	2.52%	0.23	509.333		
6	M13000	Asahi	200nm thick layer	14/05/2019	4.3	238	360	336	200	-0.003	0.47	-0.001	0.28	-96.58	18.02	395.90	0.35	1.62%	0.17	471.333		
7	M13001	Asahi	new N layer	14/05/2019	4.3	179	271	253	150	-0.002	0.46	-0.001	0.26	-102.76	30.46	298.95	0.32	1.53%	0.15	456.333		
8	M13002	Asahi	19nm thick p-SiC layer	14/05/2019	4.3	179	271	253	150	-0.003	0.51	-0.002	0.34	-105.33	17.16	658.10	0.43	2.32%	0.22	513.667		

Table F.7: The logbook of a p-SiC series with i-a-SiGe:H intrinsic layer consisting of i, p and n layer thickness changes with SiH_4 of 20 sccm, a CH_4 of 45 sccm, temperature of 300°C with ITO as front TCO on Corning glass - AZO combination.

a-SiGe:H - AZO (Reference GeH_4 3.4-300C-12nm p $30H_2$)										Solar Cell Parameters												
										Isc:	Voc:	Impp:	Vmpp:	Jsc :	Rs :	Rsh:	Fill factor:	Eff:	Voc x FF	Voc	Jsc :	Corrected Eff:
Sl No.	Dep. No.	AZO/Asahi	Description	Date	GeH_4 [sccm]	a-Si:H [nm]	I layer [nm]	p layer [nm]	n [nm]	[A]	[V]	[A]	[V]	[A/m^2]	[Ωm^2]	[Ωm^2]	[%]	[%]	[-]	[mV]	[mA/cm^2]	[%]
1	M13003	AZO	Reference Ge3.4-300C-12nm p $30H_2$	15/18-5-2019	3.4	0	150	12	35	-0.002	0.53	-0.001	0.39	-75.21	11.03	2063.35	0.56	2.23%	0.296	525.000	7.520613	2.23%
2	M13004	AZO	P-layer 4nm	15/18-5-2019	3.4	0	150	4	35	-0.003	0.57	-0.002	0.39	-123.04	12.28	1304.14	0.51	3.56%	0.289	569.667	12.30399	3.56%
3	M13005	AZO	P-layer 8nm	15/18-5-2019	3.4	0	150	8	35	-0.003	0.55	-0.002	0.38	-117.78	12.04	1141.95	0.50	3.22%	0.273	545.333	11.7778	3.22%
4	M13006	AZO	i-layer 175nm	15/18-5-2019	3.4	0	175	12	35	-0.003	0.56	-0.002	0.39	-107.71	15.04	1409.83	0.52	3.13%	0.291	559.667	10.77136	3.13%
5	M13007	AZO	i-layer 125nm	15/18-5-2019	3.4	0	125	12	35	-0.002	0.50	-0.001	0.35	-84.50	10.59	1010.91	0.47	2.01%	0.236	502.000	8.449733	1.98%
6	M13008	AZO	N-layer 50nm+5nm a-Si:H	15/18-5-2019	3.4	5	150	12	50	-0.003	0.56	-0.002	0.37	-128.19	19.68	991.95	0.48	3.41%	0.267	562.000	12.81907	3.43%
7	M13009	AZO	n-layer 20nm+5 a-Si:H	15/18-5-2019	3.4	5	150	12	20	SHUNTED	SHUNTED	SHUNTED	SHUNTED	SHUNTED	SHUNTED	SHUNTED	SHUNTED	SHUNTED	SHUNTED	SHUNTED		

Table F.8: The logbook of a p-SiC series with i-a-SiGe:H intrinsic layer consisting of i, p and n layer thickness changes with SiH_4 of 20 sccm, a CH_4 of 45 sccm, temperature of 300°C with ITO as front TCO on Asahi glass.

a-SiGe:H - Asahi										Solar Cell Parameters												
										Isc:	Voc:	Impp:	Vmpp:	Jsc :	Rs :	Rsh:	Fill factor:	Eff:	Voc x FF	Voc	Jsc :	Corrected Eff:
Sl No.	Dep. No.	AZO/Asahi	Description	Date	GeH_4 [sccm]	a-Si:H [nm]	I layer [nm]	p layer [nm]	n [nm]	[A]	[V]	[A]	[V]	[A/m^2]	[Ωm^2]	[Ωm^2]	[%]	[%]	[-]	[mV]	[mA/cm^2]	[%]
1	M13022	Asahi	Reference Ge3.4-300C-12nm p $30H_2$	15/18-5-2019	3.4	0	150	12	35	-0.003	0.52	-0.002	0.35	-111.16	16.96	675.20	0.44	2.60%	0.231	524.000	11.11632	2.56%
2	M13023	Asahi	P-layer 4nm	15/18-5-2019	3.4	0	150	4	35	SHUNTED	SHUNTED	SHUNTED	SHUNTED	SHUNTED	SHUNTED	SHUNTED	SHUNTED	SHUNTED	SHUNTED	SHUNTED	SHUNTED	SHUNTED
3	M13024	Asahi	P-layer 8nm	15/18-5-2019	3.4	0	150	8	35	-0.004	0.54	-0.002	0.37	-148.58	16.07	419.33	0.44	3.50%	0.236	540.000	14.85819	3.50%
4	M13025	Asahi	i-layer 175nm	15/18-5-2019	3.4	0	175	12	35	-0.004	0.54	-0.003	0.35	-149.93	14.80	551.45	0.44	3.58%	0.239	541.000	14.99253	3.57%
5	M13026	Asahi	i-layer 125nm	15/18-5-2019	3.4	0	125	12	35	SHUNTED	SHUNTED	SHUNTED	SHUNTED	SHUNTED	SHUNTED	SHUNTED	SHUNTED	SHUNTED	SHUNTED	SHUNTED	SHUNTED	SHUNTED
6	M13027	Asahi	N-layer 50nm+5nm a-Si:H	15/18-5-2019	3.4	5	150	12	50	SHUNTED	SHUNTED	SHUNTED	SHUNTED	SHUNTED	SHUNTED	SHUNTED	SHUNTED	SHUNTED	SHUNTED	SHUNTED	#VALUE!	SHUNTED
7	M13028	Asahi	n-layer 20nm+5 a-Si:H	15/18-5-2019	3.4	5	150	12	20	-0.003	0.41	-0.002	0.22	-117.62	14.12	181.31	0.30	1.43%	0.122	405.000	11.76192	1.43%

F.2. p-SiOx logbook

Table F.9: The logbook of a p-SiOx series with i-a-SiGe:H intrinsic layer consisting of combinations of p-nc-SiOx, p-nc-Si and seed layer of i-nc-Si on Corning glass - AZO and Asahi glass combination.

a-SiGe:H - AZO First SiOx n-ncSi+n-aSi										Solar Cell Parameters												
										Isc:	Voc:	Impp:	Vmpp:	Jsc :	Rs :	Rsh:	Fill factor:	Eff:	Voc x FF	Voc	Jsc :	Corrected Eff:
SI No.	Dep. No.	Asahi/AZO	Description	Date	i-nc-Si [s]	p-nc-Si [s]	p-ncSiOx [s]	p-ncSiOx [s]	H_2 [sccm]	[A]	[V]	[A]	[V]	[A/m^2]	[Ωm^2]	[Ωm^2]	[%]	[%]	[-]	[mV]	[mA/cm^2]	[%]
1	M13010	AZO	P-SiOx No seed	18/04/2019	-	54	200	100	170	-0.003	0.55	-0.002	0.32	-123.36	12.13	933.51	0.41	0.027	0.22	546.333	12.33583	2.74%
2	M13029	Asahi	P-SiOx No seed	18/04/2019	-	54	200	100	170	-0.004	0.54	-0.003	0.27	-167.67	14.87	310.57	0.32	0.029	0.17	544.000	16.76732	2.90%
3	M13030	Asahi	P-SiOx high H_2 begin	18/04/2019	-	54	150	150	200	-0.005	0.49	-0.003	0.26	-207.18	19.26	180.72	0.32	0.032	0.16	492.333	20.71843	3.25%
4	M13031	Asahi	P-SiOx No seed + No p-nc-Si	18/04/2019	-	-	200	150	170	-0.004	0.48	-0.003	0.26	-183.30	25.39	211.90	0.32	0.028	0.15	477.667	18.33001	2.76%
5	M13032	Asahi	P-SiOx Including seed + p-ncSi	18/04/2019	150	54	150	150	170	-0.005	0.57	-0.003	0.35	-195.52	13.65	516.98	0.42	0.047	0.24	565.000	19.55221	4.64%

Table F.10: The logbook of a p-SiOx series with i-a-SiGe:H intrinsic layer consisting of combinations of different n- and p-layer of p-nc-SiOx, p-nc-Si, n-nc-SiOx, n-nc-Si and seed layer of i-nc-Si on Corning glass - AZO combination.

a-SiGe:H - AZO -different n and p										Solar Cell Parameters												
										Isc:	Voc:	Impp:	Vmpp:	Jsc :	Rs :	Rsh:	Fill factor:	Eff:	Voc x FF	Voc	Jsc :	Corrected Eff:
SI No.	Dep. No.	Asahi/AZO	Description	Date	i-nc-Si [s]	Si-SiOx ramp	n-a-Si [nm]	p-ncSiOx[s]	H_2 i/p [s]	[A]	[V]	[A]	[V]	[A/m^2]	[Ωm^2]	[Ωm^2]	[%]	[%]	[-]	[mV]	[mA/cm^2]	[%]
1	M13054	AZO	n-ncSi-SiOx Normal	24/05/2019	150	Yes	0	150-150	0	-0.003	0.50	-0.002	0.29	-108.89	37.32	359.42	0.35	0.019	0.176	502.000	10.88871	1.91%
2	M13055	AZO	n-ncSi-Ox extra 2nm a-Si	24/05/2019	150	Yes	2	150-150	0	-0.003	0.54	-0.002	0.31	-115.26	36.22	489.92	0.37	0.023	0.200	540.333	11.52579	2.30%
3	M13056	AZO	1 thick layer (step) nc-Si to nc-SiOx	24/05/2019	150	No	0	150-150	0	-0.003	0.59	-0.003	0.38	-140.03	21.30	1039.26	0.46	0.038	0.274	594.333	14.00269	3.84%
4	M13057	AZO	p-SiOx half time	24/05/2019	150	Yes	0	75-75	0	-0.003	0.58	-0.002	0.36	-136.70	20.68	1025.10	0.46	0.036	0.263	576.667	13.6696	3.59%
5	M13058	AZO	Thicker Seed	24/05/2019	200	Yes	0	150-150	0	-0.003	0.55	-0.002	0.32	-118.22	18.24	669.93	0.40	0.026	0.218	547.000	11.82196	2.58%
6	M13059	AZO	thin Seed	24/05/2019	100	Yes	0	150-150	0	-0.004	0.56	-0.002	0.35	-140.65	22.71	822.94	0.45	0.035	0.248	555.500	14.06526	3.48%
7	M13060	AZO	Reference p-SiOx (No ramping)	24/05/2019	150	No	0	150-150	0	SHUNTED	SHUNTED	SHUNTED	SHUNTED	SHUNTED	SHUNTED	SHUNTED	SHUNTED	SHUNTED	SHUNTED	SHUNTED	SHUNTED	SHUNTED
8	M13061	AZO	p-SiOx H_2 after i-seed	24/05/2019	150	Yes	0	150-150	120	-0.003	0.569	-0.00217	0.36	-128.412	17.45575	684.5798	0.428199	0.0313	0.243645	569.000	12.8412	3.13%

Table F.11: The logbook of a p-SiOx series with i-a-SiGe:H intrinsic layer consisting of combinations of different n- and p-layer of p-nc-SiOx, p-nc-Si, n-nc-SiOx, n-nc-Si and seed layer of i-nc-Si on Asahi glass.

a-SiGe:H - Asahi -different n and p										Solar Cell Parameters												
										Isc:	Voc:	Impp:	Vmpp:	Jsc :	Rs :	Rsh:	Fill factor:	Eff:	Voc x FF	Voc	Jsc :	Corrected Eff:
SI No.	Dep. No.	Asahi/AZO	Description	Date	i-nc-Si [s]	Si-SiOx ramp	n-a-Si [nm]	p-ncSiOx[s]	H_2 i/p [s]	[A]	[V]	[A]	[V]	[A/m^2]	[Ωm^2]	[Ωm^2]	[%]	[%]	[-]	[mV]	[mA/cm^2]	[%]
1	M13072	Asahi	n-ncSi-SiOx Normal	24/05/2019	150	Yes	0	150-150	0	-0.003	0.48	-0.002	0.27	-126.93	23.07	244.04	0.32	0.020	0.155	482.500	12.6927	1.97%
2	M13073	Asahi	n-ncSi-Ox extra 2nm a-Si	24/05/2019	150	Yes	2	150-150	0	-0.003	0.24	-0.001	0.12	-87.18	59.36	113.40	0.25	0.005	0.060	244.000	8.71842	0.53%
3	M13074	Asahi	1 thick layer (step) nc-Si to nc-SiOx	24/05/2019	150	No	0	150-150	0	-0.004	0.56	-0.003	0.36	-172.89	12.96	581.29	0.45	0.043	0.251	563.000	17.28892	4.34%
4	M13075	Asahi	p-SiOx half time	24/05/2019	150	Yes	0	75-75	0	-0.004	0.52	-0.002	0.32	-144.02	11.42	439.65	0.42	0.031	0.215	515.667	14.402	3.09%
5	M13076	Asahi	Thicker Seed	24/05/2019	200	Yes	0	150-150	0	-0.004	0.33	-0.002	0.18	-137.54	14.39	116.17	0.28	0.013	0.094	333.000	13.75388	1.29%
6	M13077	Asahi	thin Seed	24/05/2019	100	Yes	0	150-150	0	-0.004	0.55	-0.002	0.32	-148.12	17.84	481.08	0.39	0.032	0.214	551.333	14.81239	3.16%
7	M13078	Asahi	Reference p-SiOx (No ramping)	24/05/2019	150	No	0	150-150	0	SHUNTED	SHUNTED	SHUNTED	SHUNTED	SHUNTED	SHUNTED	SHUNTED	SHUNTED	SHUNTED	SHUNTED	SHUNTED	SHUNTED	#VALUE!
8	M13079	Asahi	p-SiOx H_2 after i-seed	24/05/2019	150	Yes	0	150-150	120	-0.003	0.56	-0.002	0.35	-118.91	15.09	518.65	0.39	0.026	0.221	562.000	11.89063	2.63%

F.3. Different n-layers logbook

Table F.12: The logbook of a n-layer series with graded GeH_4 with a U shaped intrinsic layer with n-nc-Si, n-a-Si and n-nc-SiOx combinations and different seed thicknesses on Corning Glass - AZO combination.

a-SiGe:H - AZO -different n										Solar Cell Parameters												
										Isc:	Voc:	Impp:	Vmpp:	Jsc :	Rs :	Rsh:	Fill factor:	Eff:	Voc x FF	Voc	Jsc :	Corrected Eff:
SI No.	Dep. No.	Description	Asahi/AZO	Date	n-a-Si [nm]	n-nc-Si [nm]	n-nc-SiOx [nm]	Seed [nm]	Ramping	[A]	[V]	[A]	[V]	[A/m^2]	[Ωm^2]	[Ωm^2]	[%]	[%]	[-]	[mV]	[mA/cm^2]	[%]
1	M13066	thick layer M13056 (2nm seed)	AZO	29/05/2019	5	0	35	2	Yes	-0.003	0.50	-0.002	0.32	-117.33	17.41	427.42	0.39	0.023	0.196	500.000	11.73	2.30%
2	M13105	1 step n layer - H_2 pre treatment (NEW)	AZO	29/05/2019	5	0	25	0	Yes	-0.003	0.58	-0.002	0.38	-120.24	18.05	1248.09	0.49	0.034	0.282	579.333	12.02	3.39%
3	M13071	1 step n layer (25 instead of 35nm)	AZO	29/05/2019	5	0	35	0	Yes	-0.003	0.48	-0.002	0.28	-125.47	20.71	346.10	0.35	0.021	0.170	482.000	12.55	2.14%
4	M13069	1 step n layer (seed 1 nm)	AZO	29/05/2019	5	0	25	1	Yes	-0.003	0.57	-0.002	0.37	-126.40	16.55	838.80	0.46	0.033	0.259	566.667	12.64	3.27%
5	M13068	M13032 redo (No ramping) (2nm seed)	AZO	29/05/2019	25	6	0	2	No	-0.003	0.53	-0.002	0.32	-133.39	28.31	312.17	0.35	0.025	0.185	534.000	13.34	2.46%
6	M13070	n-nc-Si and n-a-Si (including ramping) (2nm seed)	AZO	29/05/2019	25	6	0	2	Yes	-0.003	0.55	-0.001	0.32	-84.28	45.62	442.83	0.33	0.016	0.182	553.500	8.43	1.54%
7	M13067	n-nc-Si and n-a-Si (1nm seed)	AZO	29/05/2019	25	6	0	1	Yes	SHUNTED	SHUNTED	SHUNTED	SHUNTED	SHUNTED	SHUNTED	SHUNTED	SHUNTED	SHUNTED	SHUNTED	SHUNTED	SHUNTED	SHUNTED

Table F.13: The logbook of a n-layer series with graded GeH_4 with a U shaped intrinsic layer with n-nc-Si, n-a-Si and n-nc-SiOx combinations and different seed thicknesses on Asahi glass.

a-SiGe:H - Asahi -different n										Solar Cell Parameters												
										Isc:	Voc:	Impp:	Vmpp:	Jsc :	Rs :	Rsh:	Fill factor:	Eff:	Voc x FF	Voc	Jsc :	Corrected Eff:
SI No.	Dep. No.	Description	Asahi/AZO	Date	n-a-Si [nm]	n-nc-Si [nm]	n-nc-SiOx [nm]	Seed [nm]	Ramping	[A]	[V]	[A]	[V]	[A/m^2]	[Ωm^2]	[Ωm^2]	[%]	[%]	[-]	[mV]	[mA/cm^2]	[%]
1	M13098	thick layer M13056 (2nm seed)	Asahi	29/05/2019	5	0	35	2	Yes	-0.003	0.20	-0.002	0.10	-135.33	19.75	61.71	0.25	0.007	0.052	204.000	13.53	0.70%
2	M13099	1 step n layer - H_2 pre treatment (NIEUW)	Asahi	29/05/2019	5	0	25	0	Yes	-0.004	0.43	-0.002	0.26	-165.47	16.50	225.55	0.36	0.026	0.156	432.000	16.55	2.57%
3	M13100	1 step n layer (25 instead of 35nm)	Asahi	29/05/2019	5	0	35	0	Yes	SHUNTED	SHUNTED	SHUNTED	SHUNTED	SHUNTED	SHUNTED	SHUNTED	SHUNTED	SHUNTED	SHUNTED	SHUNTED	SHUNTED	SHUNTED
4	M13101	1 step n layer (seed 1 nm)	Asahi	29/05/2019	5	0	25	1	Yes	SHUNTED	SHUNTED	SHUNTED	SHUNTED	SHUNTED	SHUNTED	SHUNTED	SHUNTED	SHUNTED	SHUNTED	SHUNTED	SHUNTED	SHUNTED
5	M13102	M13032 redo (No ramping) (2nm seed)	Asahi	29/05/2019	25	6	0	2	No	-0.004	0.58	-0.003	0.38	-145.91	9.40	1120.01	0.51	0.042	0.291	575.000	14.59	4.24%
6	M13103	n-nc-Si and n-a-Si (including ramping) (2nm seed)	Asahi	29/05/2019	25	6	0	2	Yes	-0.004	0.56	-0.003	0.36	-144.34	9.40	825.83	0.46	0.038	0.261	563.000	14.43	3.77%
7	M13104	n-nc-Si and n-a-Si (1nm seed)	Asahi	29/05/2019	25	6	0	1	Yes	-0.003	0.48	-0.002	0.30	-133.41	13.80	294.17	0.37	0.024	0.177	480.000	13.34	2.36%

Table F.14: The logbook of a n-layer series with graded GeH_4 with a U shaped intrinsic layer with n-nc-Si, double n-a-Si and n-nc-SiOx combinations and different seed thicknesses on Corning Glass - AZO combination.

Different n layers										Solar Cell Parameters												
										Isc:	Voc:	Impp:	Vmpp:	Jsc :	Rs :	Rsh:	Fill factor:	Eff:	Voc x FF	Voc	Jsc :	Corrected Eff:
SI No.	Dep. No.	Description	Asahi/AZO	Date	n-a-Si [nm]	nSiOx [nm]	n-nc-Si [nm]	n-a-Si [nm]	Graded?	[A]	[V]	[A]	[V]	[A/m^2]	[Ωm^2]	[Ωm^2]	[%]	[%]	[-]	[mV]	[mA/cm^2]	[%]
1	M14000	n-aSi(4/5)/nSiOx(20)/n-ncSi(4/5) -TCO (graded)	AZO	17/06/2019	5	20	5	-	Yes	-0.003	0.571	-0.002	0.340	-112.917	17.642	456.256	0.365	2.36%	0.209	571.000	x	2.36%
2	M14001	n-aSi(4/5)/nSiOx(20)/n-ncSi(4/5)/ n-aSi(4/5)-TCO (Non graded)	AZO	17/06/2019	5	20	5	5	No	-0.003	0.564	-0.002	0.350	-122.350	28.632	504.987	0.404	2.78%	0.227	563.500	x	2.78%
3	M14002	n-aSi(22)/nSiOx(8) -TCO (Non-graded)	AZO	17/06/2019	22	8	-	-	No	-0.003	0.397	-0.001	0.200	-101.756	71.927	190.252	0.273	1.10%	0.108	397.000	x	1.10%

Table F.15: The logbook of a H_2 treatment series with graded GeH_4 with a U shaped intrinsic layer before and after the n-a-Si on Corning Glass - AZO combination.

Different H_2 treatment										Solar Cell Parameters												
										Isc:	Voc:	Impp:	Vmpp:	Jsc :	Rs :	Rsh:	Fill factor:	Eff:	Voc x FF	Voc	Jsc :	Corrected Eff:
SI No.	Dep. No.	Description	Asahi/AZO	Date	n-nc-Si [nm]	nSiOx low [nm]	nSiOx High [nm]	n-a-Si [nm]	H_2 before a-Si	[A]	[V]	[A]	[V]	[A/m^2]	[Ωm^2]	[Ωm^2]	[%]	[%]	[-]	[mV]	[mA/cm^2]	[%]
1	M14054	H_2 treatment after n-Asi	AZO	25/06/2019	6	8	20	5	No	-0.003	0.738	-0.002	0.484	-122.042	10.953	3321.106	0.527	4.74%	0.389	738.000	x	4.74%
2	M14055	H_2 treatment before n-Asi	AZO	25/06/2019	6	8	20	5	Yes	-0.003	0.735	-0.002	0.480	-114.773	16.314	2884.338	0.499	4.21%	0.367	735.000	x	4.21%

F.4. Pressure series logbook

Table F.16: The logbook of a pressure series on graded GeH_4 with a U shaped intrinsic layer on Corning Glass - AZO combination.

Pressure change - AZO										Solar Cell Parameters													
										Isc:	Voc:	Impp:	Vmpp:	Jsc :	Rs :	Rsh:	Fill factor:	Eff:	Voc x FF	Voc	Jsc :	Corrected Eff:
SI No.	Dep. No.	AZO/Asahi	Description	Date	SiH_4 [sccm]	GeH_4 [sccm]	H_2 [sccm]	Power [W]	Pressure [mbar]	[A]	[V]	[A]	[V]	[A/m^2]	[Ωm^2]	[Ωm^2]	[%]	[%]	[-]	[mV]	[mA/cm^2]	[%]
1	M13111	AZO	Pressure 2.4 mbar	31/05/2019	30	3.65	200	3	2.4	-0.003	0.580	-0.002	0.390	-124.289	11.379	1060.513	0.478	3.45%	0.278	580.000	14.503	4.02%
2	M13112	AZO	Pressure 3 mbar	31/05/2019	30	3.65	200	3	3	-0.003	0.601	-0.002	0.367	-134.115	16.822	596.084	0.402	3.24%	0.241	601.333	15.280	3.69%
3	M13105	AZO	Pressure 3.6 mbar	29/05/2019	30	3.65	200	3	3.6	-0.003	0.579	-0.002	0.380	-120.242	18.052	1248.090	0.487	3.40%	0.282	579.333	14.839	4.19%
4	M13113	AZO	Pressure 4.2 mbar	31/05/2019	30	3.65	200	3	4.2	-0.004	0.535	-0.002	0.330	-143.741	15.789	456.033	0.388	2.97%	0.209	534.500	14.540	3.01%
5	M13114	AZO	Pressure 4.8 mbar	31/05/2019	30	3.65	200	3	4.8	-0.004	0.573	-0.002	0.360	-133.508	18.810	725.428	0.432	3.31%	0.247	572.500	14.098	3.48%

Table F.17: The logbook of a pressure series on graded GeH_4 with a U shaped intrinsic layer on Asahi glass.

Pressure change - Asahi										Solar Cell Parameters												
										Isc:	Voc:	Impp:	Vmpp:	Jsc :	Rs :	Rsh:	Fill factor:	Eff:	Voc x FF	Voc	Jsc :	Corrected Eff:
SI No.	Dep. No.	AZO/Asahi	Description	Date	SiH_4 [sccm]	GeH_4 [sccm]	H_2 [sccm]	Power [W]	Pressure [mbar]	[A]	[V]	[A]	[V]	[A/m^2]	[Ωm^2]	[Ωm^2]	[%]	[%]	[-]	[mV]	[mA/cm^2]	[%]
1	M13125	Asahi	Pressure 2.4 mbar	31/05/2019	30	3.65	200	3	2.4	-0.004	0.551	-0.003	0.347	-154.858	17.112	396.488	0.408	3.48%	0.225	550.667	x	3.48%
2	M13126	Asahi	Pressure 3 mbar	31/05/2019	30	3.65	200	3	3	-0.003	0.582	-0.002	0.353	-133.958	17.274	571.797	0.395	3.08%	0.230	581.667	x	3.08%
3	M13099	Asahi	Pressure 3.6 mbar	29/05/2019	30	3.65	200	3	3.6	-0.004	0.432	-0.002	0.260	-165.473	16.499	225.545	0.360	2.57%	0.156	432.000	x	2.57%
4	M13127	Asahi	Pressure 4.2 mbar	31/05/2019	30	3.65	200	3	4.2	-0.003	0.380	-0.002	0.207	-124.929	20.182	149.820	0.285	1.35%	0.108	380.000	x	1.35%
5	M13128	Asahi	Pressure 4.8 mbar	31/05/2019	30	3.65	200	3	4.8	-0.003	0.565	-0.002	0.360	-134.910	17.756	764.564	0.438	3.34%	0.248	565.000	x	3.34%

F.5. Power series logbook

Table F.18: The logbook of a power series on graded GeH_4 with a U shaped intrinsic layer on Corning Glass - AZO combination.

Power change - AZO										Solar Cell Parameters												
										Isc:	Voc:	Impp:	Vmpp:	Jsc :	Rs :	Rsh:	Fill factor:	Eff:	Voc x FF	Voc	Jsc :	Corrected Eff:
SI No.	Dep. No.	AZO/Asahi	Description	Date	SiH_4 [sccm]	GeH_4 [sccm]	H_2 [sccm]	Pressure [mbar]	Power [W]	[A]	[V]	[A]	[V]	[A/m^2]	[Ωm^2]	[Ωm^2]	[%]	[%]	[-]	[mV]	[mA/cm^2]	[%]
1	M13105	AZO	Power 3W	29/05/2019	30	3.65	200	3.6	3	-0.003	0.579	-0.002	0.380	-120.242	18.052	1248.090	0.487	3.40%	0.282	579.333	14.839	4.19%
2	M13107	AZO	Power 4W	31/05/2019	30	3.65	200	3.6	4	-0.003	0.551	-0.002	0.360	-129.288	22.872	876.762	0.458	3.26%	0.252	551.000	13.066	3.30%
3	M13108	AZO	Power 5W	31/05/2019	30	3.65	200	3.6	5	-0.003	0.545	-0.002	0.360	-109.722	12.068	1072.588	0.476	2.84%	0.259	545.000	12.456	3.23%
4	M13110	AZO	Power 6W	31/05/2019	30	3.65	200	3.6	6	-0.002	0.504	-0.001	0.300	-80.483	19.890	425.346	0.336	1.37%	0.169	503.500	X	X
5	M13109	AZO	Power 7W	31/05/2019	30	3.65	200	3.6	7	-0.003	0.658	-0.002	0.407	-127.780	13.184	704.800	0.405	3.40%	0.267	658.000	15.216	4.06%

Table F.19: The logbook of a power series on graded GeH_4 with a U shaped intrinsic layer on Asahi glass.

Power change - Asahi										Solar Cell Parameters												
										Isc:	Voc:	Impp:	Vmpp:	Jsc :	Rs :	Rsh:	Fill factor:	Eff:	Voc x FF	Voc	Jsc :	Corrected Eff:
SI No.	Dep. No.	AZO/Asahi	Description	Date	SiH_4 [sccm]	GeH_4 [sccm]	H_2 [sccm]	Pressure [mbar]	Power [W]	[A]	[V]	[A]	[V]	[A/m^2]	[Ωm^2]	[Ωm^2]	[%]	[%]	[-]	[mV]	[mA/cm^2]	[%]
1	M13099	Asahi	Power 3W	29/05/2019	30	3.65	200	3.6	3	-0.004	0.432	-0.002	0.260	-165.473	16.499	225.545	0.360	2.57%	0.156	432.000	x	2.57%
2	M13121	Asahi	Power 4W	31/05/2019	30	3.65	200	3.6	4	-0.004	0.561	-0.003	0.350	-162.607	18.680	525.845	0.427	3.89%	0.239	560.500	x	3.89%
3	M13122	Asahi	Power 5W	31/05/2019	30	3.65	200	3.6	5	-0.003	0.551	-0.002	0.360	-111.450	17.208	848.598	0.448	2.75%	0.247	550.750	x	2.75%
4	M13124	Asahi	Power 6W	31/05/2019	30	3.65	200	3.6	6	-0.003	0.317	-0.001	0.170	-86.551	35.485	177.411	0.274	0.80%	0.087	316.500	x	0.80%
5	M13123	Asahi	Power 7W	31/05/2019	30	3.65	200	3.6	7	-0.003	0.632	-0.002	0.370	-116.842	36.163	434.746	0.341	2.53%	0.215	632.000	x	2.53%

F.6. GeH_4 flow rate logbook

Table F.20: The logbook of a graded GeH_4 flow rate series with a U shaped intrinsic layer on Corning Glass - AZO combination.

Germanium change - AZO										Solar Cell Parameters												
SI No.	Dep. No.	AZO/Asahi	Description	Date	SiH_4 [sccm]	GeH_4 [sccm]	H_2 [sccm]	Power [W]	Pressure [mbar]	Isc:	Voc:	Impp:	Vmpp:	Jsc :	Rs :	Rsh:	Fill factor:	Eff:	Voc x FF	Voc	Jsc :	Corrected Eff:
										[A]	[V]	[A]	[V]	[A/m^2]	[Ωm^2]	[Ωm^2]	[%]	[%]	[-]	[mV]	[mA/cm^2]	[%]
1	M13062	AZO	M13099 (1-n layer -H_2) - GeH_4 5.3	30/05/2019	30	5.3	200	3	3.6	-0.004	0.516	-0.002	0.320	-145.875	25.052	557.394	0.416	3.14%	0.215	516.000	14.839	3.19%
2	M13063	AZO	M13099 (1-n layer -H_2) - GeH_4 4.3	30/05/2019	30	4.3	200	3	3.6	-0.003	0.549	-0.002	0.347	-138.578	31.929	735.297	0.432	3.29%	0.237	548.667	13.656	3.23%
3	M13105	AZO	GeH_4 H_4 3.65	29/05/2019	30	3.65	200	3	3.6	-0.003	0.579	-0.002	0.380	-120.242	18.052	1248.090	0.487	3.40%	0.282	579.333	13.424	3.79%
4	M13064	AZO	M13099 (1-n layer -H_2) - GeH_4 2.4	30/05/2019	30	2.4	200	3	3.6	-0.003	0.657	-0.002	0.453	-128.241	22.019	1744.511	0.520	4.38%	0.341	657.000	11.985	4.09%
5	M13065	AZO	M13099 (1-n layer -H_2) - GeH_4 1.6	30/05/2019	30	1.6	200	3	3.6	-0.003	0.737	-0.002	0.515	-120.581	27.691	2319.374	0.528	4.69%	0.389	736.750	11.563	4.50%
6	M13106	AZO	M13099 (1-n layer -H_2) - GeH_4 0.8	30/05/2019	30	0.8	200	3	3.6	-0.003	0.754	-0.002	0.550	-101.784	26.063	3221.005	0.572	4.39%	0.431	754.250	10.691	4.61%

Table F.21: The logbook of a graded GeH_4 flow rate series with a U shaped intrinsic layer on Asahi glass.

Germanium change - Asahi										Solar Cell Parameters												
SI No.	Dep. No.	AZO/Asahi	Description	Date	SiH_4 [sccm]	GeH_4 [sccm]	H_2 [sccm]	Power [W]	Pressure [mbar]	Isc:	Voc:	Impp:	Vmpp:	Jsc :	Rs :	Rsh:	Fill factor:	Eff:	Voc x FF	Voc	Jsc :	Corrected Eff:
										[A]	[V]	[A]	[V]	[A/m^2]	[Ωm^2]	[Ωm^2]	[%]	[%]	[-]	[mV]	[mA/cm^2]	[%]
1	M13116	Asahi	M13099 (1-n layer -H_2) - GeH_4 5.3	30/05/2019	30	5.3	200	3	3.6	-0.004	0.437	-0.002	0.250	-147.184	22.802	265.214	0.362	2.34%	0.158	437.000	14.27471	2.26%
2	M13117	Asahi	M13099 (1-n layer -H_2) - GeH_4 4.3	30/05/2019	30	4.3	200	3	3.6	-0.003	0.460	-0.002	0.280	-129.696	16.405	292.961	0.373	2.23%	0.172	459.500	15.2624	2.62%
3	M13099	Asahi	GeH_4 H_4 3.65	29/05/2019	30	3.65	200	3	3.6	-0.004	0.432	-0.002	0.260	-165.473	16.499	225.545	0.360	2.57%	0.156	432.000	16.54732	2.57%
4	M13118	Asahi	M13099 (1-n layer -H_2) - GeH_4 2.4	30/05/2019	30	2.4	200	3	3.6	SHUNTED	SHUNTED	SHUNTED	SHUNTED	SHUNTED	SHUNTED	SHUNTED	SHUNTED	SHUNTED	SHUNTED	SHUNTED	X	SHUNTED
5	M13119	Asahi	M13099 (1-n layer -H_2) - GeH_4 1.6	30/05/2019	30	1.6	200	3	3.6	-0.004	0.690	-0.002	0.470	-147.908	16.631	726.712	0.456	4.70%	0.316	690.000	15.7357	4.95%
6	M13120	Asahi	M13099 (1-n layer -H_2) - GeH_4 0.8	30/05/2019	30	0.8	200	3	3.6	-0.002	0.733	-0.002	0.540	-96.345	15.850	1912.880	0.583	4.12%	0.428	733.333	11.54405	4.94%

Table F.22: The logbook of a graded GeH_4 flow rate series with a V shaped intrinsic layer (with n/i width of 120 nm and i/p width of 30 nm) consisting of n/i buffers consisting of 3.2 nm i-a-Si and 5 nm i-a-SiGe:H and 5 nm i/p a-SiGe:H on Corning Glass - AZO combination.

Ge - buffer (n/i a-Si + n/i a-SiGe:H + i/p a-SiGe)								Solar Cell Parameters												
SI No.	Dep. No.	Description	Date	SiH_4 [sccm]	GeH_4 [sccm]	H_2 [sccm]	Thickness [nm]	Isc:	Voc:	Impp:	Vmpp:	Jsc :	Rs :	Rsh:	Fill factor:	Eff:	Voc x FF	Voc	Jsc :	Corrected Eff:
								[A]	[V]	[A]	[V]	[A/m^2]	[Ωm^2]	[Ωm^2]	[%]	[%]	[-]	[mV]	[mA/cm^2]	[%]
1	M14206	GeH_4 up to 5.3	23/07/2019	30	5.3	200	150	-0.004	0.574	-0.003	0.320	-143.864	23.447	693.626	0.393	3.25%	0.226	574.000	15.4391	3.48%
2	M14207	GeH_4 up to 4.3	24/07/2019	30	4.3	200	150	-0.003	0.613	-0.002	0.360	-130.394	25.900	914.328	0.408	3.26%	0.250	613.000	15.2918	3.82%
3	M14208	GeH_4 up to 3.3	24/07/2019	30	3.3	200	150	0.004	0.667	-0.002	0.450	-128.769	17.662	1753.703	0.515	4.44%	0.344	667.000	13.6124	4.68%
4	M14202	GeH_4 2.4 with i-n buffers	21/07/2019	30	2.4	200	150	-0.003	0.737	-0.003	0.540	-119.845	13.586	4690.128	0.616	5.45%	0.454	737.333	12.195	5.54%
5	M14209	GeH_4 up to 1.6	24/07/2019	30	1.6	200	150	-0.003	0.758	-0.002	0.553	-110.308	13.018	2784.411	0.582	4.87%	0.441	758.000	12.4294	5.48%

Table F.23: The logbook of a graded GeH_4 flow rate series with a V shaped intrinsic layer (with n/i width of 120 nm and i/p width of 30 nm) consisting of n/i buffers consisting of 3.2 nm i-a-Si and 5 nm i-a-SiGe:H on Corning Glass - AZO combination.

Ge - buffer (n/i a-Si + n/i a-SiGe)								Solar Cell Parameters												
								Isc:	Voc:	Impp:	Vmpp:	Jsc :	Rs :	Rsh:	Fill factor:	Eff:	Voc x FF	Voc	Jsc :	Corrected Eff:
Sl No.	Dep. No.	Description	Date	SiH_4 [sccm]	GeH_4 [sccm]	H_2 [sccm]	Thickness [nm]	[A]	[V]	[A]	[V]	[A/m^2]	[Ωm^2]	[Ωm^2]	[%]	[%]	[-]	[mV]	[mA/cm^2]	[%]
1	M14280	GeH_4 up to 5.3	04/08/2019	30	5.3	200	150	-0.004	0.531	-0.002	0.340	-145.548	26.952	398.985	0.416	3.22%	0.221	531.000	14.04	3.10%
2	M14281	GeH_4 up to 4.3	04/08/2019	30	4.3	200	150	-0.003	0.547	-0.002	0.340	-127.759	27.118	479.785	0.402	2.81%	0.220	546.500	12.77	2.81%
3	M14282	GeH_4 up to 3.3	05/08/2019	30	3.3	200	150	-0.003	0.628	-0.002	0.430	-124.611	22.106	533.209	0.439	3.45%	0.276	628.000	12.57	3.47%
4	M14274	GeH_4 2.4 with i-n buffers	04/08/2019	30	2.4	200	150	-0.003	0.737	-0.003	0.560	-118.620	9.535	5093.658	0.648	5.67%	0.478	736.667	12.46	5.95%
5	M14283	GeH_4 up to 1.6	05/08/2019	30	1.6	200	150	-0.003	0.710	-0.002	0.500	-115.488	14.453	437.407	0.395	3.24%	0.280	710.000	11.55	3.24%

Table F.24: The logbook of a graded GeH_4 flow rate series with a V shaped intrinsic layer (with n/i width of 120 nm and i/p width of 30 nm) consisting of n/i buffers consisting of 3.2 nm i-a-Si and 5 nm i-a-SiGe:H on Corning Glass - AZO combination.

Ge - buffer (n/i a-Si + n/i a-SiGe)								Solar Cell Parameters												
								Isc:	Voc:	Impp:	Vmpp:	Jsc :	Rs :	Rsh:	Fill factor:	Eff:	Voc x FF	Voc	Jsc :	Corrected Eff:
Sl No.	Dep. No.	Description	Date	SiH_4 [sccm]	GeH_4 [sccm]	H_2 [sccm]	Thickness [nm]	[A]	[V]	[A]	[V]	[A/m^2]	[Ωm^2]	[Ωm^2]	[%]	[%]	[-]	[mV]	[mA/cm^2]	[%]
1	M14312	GeH_4 5.3	09/08/2019	30	5.3	200	150	-0.004	0.566	-0.003	0.380	-146.053	20.837	1125.600	0.496	4.10%	0.281	566.333	15.39	4.32%
2	M14313	GeH_4 4.3 - total 150nm	09/08/2019	30	4.3	200	150	-0.003	0.610	-0.002	0.427	-121.463	17.534	544.982	0.435	3.24%	0.266	609.667	13.66	3.62%
3	M14314	GeH_4 3.3	09/08/2019	30	3.3	200	150	-0.003	0.678	-0.002	0.500	-117.098	13.603	5192.551	0.620	4.92%	0.420	677.667	13.33	5.60%
4	M14309	GeH_4 2.4-120 [in] nm	09/08/2019	30	2.4	200	150	-0.003	0.734	-0.003	0.547	-123.741	11.010	4779.497	0.636	5.78%	0.467	734.333	13.23	6.18%
5	M14315	GeH_4 1.6	09/08/2019	30	1.6	200	150	-0.003	0.763	-0.002	0.553	-109.525	21.151	5365.209	0.594	4.96%	0.454	763.333	13.05	5.92%

F.7. Grading shapes logbook

Table F.25: The logbook of V, E and U shaped intrinsic layers with a graded GeH$_4$ flow rate from 2 to 2.4 sccm, and a constant intrinsic layer thickness of 150 nm.

(1) Grading V-Series (GeH$_4$ 2-2.4 and i=150nm)								Solar Cell Parameters													
								Isc:	Voc:	Impp:	Vmpp:	Jsc :	Rs :	Rsh:	Fill factor:	Eff:	Voc x FF	Voc	Jsc :	Corrected Eff:
SI No.	Dep. No.	Description	Date	n/i [nm]	i-i [nm]	i/p [nm]	Thickness [nm]	[A]	[V]	[A]	[V]	[A/m^2]	[Ωm^2]	[Ωm^2]	[%]	[%]	[-]	[mV]	[mA/cm^2]	[%]
1	M13064	M13099	30/05/2019	-	-	-	150	-0.003	0.657	-0.002	0.453	-128.241	22.019	1744.511	0.520	4.38%	0.341	657.000	11.985	4.38%
2	M13153	V-shape 1 (1/3 - 2/3)	07/06/2019	50	0	100	150	-0.003	0.726	-0.002	0.440	-124.791	27.864	1181.516	0.408	3.69%	0.296	725.600	x	3.69%
3	M13154	V-shape 2 (1/2 -1/2)	07/06/2019	75	0	75	150	-0.003	0.682	-0.002	0.410	-126.064	45.434	998.706	0.409	3.51%	0.279	682.250	x	3.51%
4	M13155	V-shape 3 (2/3 - 1/3)	07/06/2019	100	0	50	150	SHUNTED	SHUNTED	SHUNTED	SHUNTED	SHUNTED	SHUNTED	SHUNTED	SHUNTED	SHUNTED	SHUNTED	SHUNTED	SHUNTED	SHUNTED
5	M13156	U-shape 1 (1/5 - 2/5 - 2/5)	07/06/2019	30	60	60	150	-0.003	0.692	-0.002	0.420	-132.813	40.623	858.169	0.410	3.76%	0.283	691.750	x	3.76%
6	M13157	U-shape 2 (1/5 - 3/5 - 1/5)	07/06/2019	30	90	30	150	-0.003	0.643	-0.002	0.387	-97.278	57.286	935.384	0.396	2.48%	0.255	643.333	x	2.48%
7	M13158	U-shape 3 (2/5 - 2/5 - 1/5)	07/06/2019	60	60	30	150	-0.003	0.622	-0.002	0.340	-116.221	82.526	431.553	0.331	2.38%	0.205	622.000	x	2.38%
8	M13159	E-shape 1 (1/5 - 2/5 - 2/5)	07/06/2019	30	60	60	150	-0.002	0.718	-0.001	0.370	-97.075	141.171	415.383	0.282	1.97%	0.202	718.000	x	1.97%
9	M13160	E-shape 2 (1/5 - 3/5 - 1/5)	07/06/2019	30	90	30	150	SHUNTED	SHUNTED	SHUNTED	SHUNTED	SHUNTED	SHUNTED	SHUNTED	SHUNTED	SHUNTED	SHUNTED	SHUNTED	SHUNTED	SHUNTED
10	M13161	E-shape 3 (2/5 - 2/5 - 1/5)	07/06/2019	60	60	30	150	-0.003	0.692	-0.002	0.428	-110.344	41.801	1089.184	0.425	3.25%	0.294	692.400	x	3.25%

Table F.26: The logbook of V-, E- and U-shaped intrinsic layers with a graded GeH$_4$ flow rate from 0 to 2.4 sccm, and a constant intrinsic layer thickness of 150 nm.

(2) Grading V-Series (GeH$_4$ 0-2.4 and i=150nm)								Solar Cell Parameters													
								Isc:	Voc:	Impp:	Vmpp:	Jsc :	Rs :	Rsh:	Fill factor:	Eff:	Voc x FF	Voc	Jsc :	Corrected Eff:
SI No.	Dep. No.	Description	Date	n/i [nm]	i-i [nm]	i/p [nm]	Thickness [nm]	[A]	[V]	[A]	[V]	[A/m^2]	[Ωm^2]	[Ωm^2]	[%]	[%]	[-]	[mV]	[mA/cm^2]	[%]
1	M14064	V-shape 1 (1/3 - 2/3)	28/06/2019	50	0	100	150	-0.003	0.747	-0.002	0.480	-127.317	13.873	2759.441	0.501	4.76%	0.374	747.000	12.614	4.72%
2	M14065	V-shape 2 (1/2 -1/2)	29/06/2019	75	0	75	150	-0.002	0.730	-0.002	0.500	-85.663	12.479	5352.840	0.557	3.48%	0.407	729.667	12.246	4.98%
3	M14066	V-shape 3 (2/3 - 1/3)	29/06/2019	100	0	50	150	-0.003	0.733	-0.002	0.520	-117.919	13.946	4133.824	0.584	5.05%	0.428	733.333	11.750	5.03%
4	M14067	U-shape 1 (1/5 - 2/5 - 2/5)	29/06/2019	30	60	60	150	-0.003	0.704	-0.002	0.460	-105.382	12.190	2507.354	0.498	3.69%	0.351	704.333	12.392	4.34%
5	M14068	U-shape 2 (1/5 - 3/5 - 1/5)	29/06/2019	30	90	30	150	-0.003	0.691	-0.003	0.467	-136.332	12.640	2241.410	0.537	5.06%	0.371	691.333	13.663	5.07%
6	M14069	U-shape 3 (2/5 - 2/5 - 1/5)	29/06/2019	60	60	30	150	-0.004	0.711	-0.003	0.493	-143.252	13.811	2919.346	0.564	5.74%	0.401	710.667	12.394	4.96%
7	M14070	E-shape 1 (1/5 - 2/5 - 2/5)	29/06/2019	30	60	60	150	-0.003	0.721	-0.002	0.480	-121.927	12.954	2559.024	0.529	4.65%	0.381	721.000	11.090	4.23%
8	M14071	E-shape 2 (1/5 - 3/5 - 1/5)	30/06/2019	30	90	30	150	SHUNTED	SHUNTED	SHUNTED	SHUNTED	SHUNTED	SHUNTED	SHUNTED	SHUNTED	SHUNTED	SHUNTED	SHUNTED	SHUNTED	SHUNTED
9	M14072	E-shape 3 (2/5 - 2/5 - 1/5)	30/06/2019	60	60	30	150	-0.004	0.728	-0.003	0.500	-140.257	14.912	3123.647	0.558	5.71%	0.407	728.000	12.453	5.06%

F.8. Graded intrinsic layer thickness logbook

Table F.27: The logbook of an intrinsic layer thickness change series with a U shaped intrinsic layer (with a small n/i width) with a GeH_4 flow rate from 2 to 2.4 sccm.

Grading U1-Series (Thickness change) (GeH_4 2-2.4)								Solar Cell Parameters												
								Isc:	Voc:	Impp:	Vmpp:	Jsc :	Rs :	Rsh:	Fill factor:	Eff:	Voc x FF	Voc	Jsc :	Corrected Eff:
Sl No.	Dep. No.	Description	Date	n/i [nm]	i-i [nm]	i/p [nm]	Thickness [nm]	[A]	[V]	[A]	[V]	[A/m^2]	[Ωm^2]	[Ωm^2]	[%]	[%]	[-]	[mV]	[mA/cm^2]	[%]
1	M14041	i=125nm	24/06/2019	25	50	50	125	-0.003	0.661	-0.002	0.367	-108.011	60.978	925.575	0.368	2.62%	0.243	660.667	x	2.62%
2	M13156	i=150nm	28/06/2019	30	60	60	150	-0.003	0.659	-0.002	0.367	-122.524	52.959	635.580	0.346	2.81%	0.228	659.000	x	2.81%
3	M14042	i=175nm	24/06/2019	35	70	70	175	-0.003	0.695	-0.002	0.420	-119.125	41.242	1316.395	0.422	3.49%	0.293	695.000	x	3.49%
4	M14043	i=200nm	24/06/2019	40	80	80	200	-0.003	0.697	-0.002	0.407	-118.231	50.993	1145.271	0.397	3.28%	0.276	696.667	x	3.28%

Table F.28: The logbook of an intrinsic layer thickness change series with a U shaped intrinsic layer (with a wide n/i width) with a GeH_4 flow rate from 0.2 to 2.4 sccm.

Grading U3-Series (Thickness change) (GeH_4 0.2-2.4)								Solar Cell Parameters												
								Isc:	Voc:	Impp:	Vmpp:	Jsc :	Rs :	Rsh:	Fill factor:	Eff:	Voc x FF	Voc	Jsc :	Corrected Eff:
Sl No.	Dep. No.	Description	Date	n/i [nm]	i-i [nm]	i/p [nm]	Thickness [nm]	[A]	[V]	[A]	[V]	[A/m^2]	[Ωm^2]	[Ωm^2]	[%]	[%]	[-]	[mV]	[mA/cm^2]	[%]
1	M14063	i=125nm	28/06/2019	50	50	25	125	-0.003	0.696	-0.002	0.513	-118.072	10.249	4287.497	0.609	5.00%	0.424	696.333	12.343	5.24%
2	M14069	i=150nm	29/06/2019	60	60	30	150	-0.004	0.711	-0.003	0.493	-143.252	13.811	2919.346	0.564	5.74%	0.401	710.667	12.394	4.96%
3	M14073	i=175nm	30/06/2019	70	70	35	175	-0.003	0.683	-0.002	0.467	-128.606	16.284	1939.309	0.528	4.64%	0.361	683.000	12.997	4.69%
4	M14074	i=200nm	30/06/2019	80	80	40	200	-0.004	0.690	-0.003	0.440	-139.462	14.559	1369.679	0.486	4.68%	0.335	690.000	13.621	4.57%

Table F.29: The logbook of an intrinsic layer thickness change series with a V shaped intrinsic layer (with a wide n/i width) with a GeH_4 flow rate from 0.2 to 2.4 sccm and n/i buffers consisting of 3.2 nm i-a-Si and i-a-SiGe:H.

Grading V3 [120-30nm] with n/i and n/i a-SiGe:H buffer								Solar Cell Parameters												
								Isc:	Voc:	Impp:	Vmpp:	Jsc :	Rs :	Rsh:	Fill factor:	Eff:	Voc x FF	Voc	Jsc :	Corrected Eff:
Sl No.	Dep. No.	Description	Date	n/i [nm]	i-i [nm]	i/p [nm]	Thickness [nm]	[A]	[V]	[A]	[V]	[A/m^2]	[Ωm^2]	[Ωm^2]	[%]	[%]	[-]	[mV]	[mA/cm^2]	[%]
1	M14277	i=125nm (GeH_4-2.4)	04/08/2019	100	0	25	125	-0.003	0.690	-0.002	0.500	-102.202	9.761	714.388	0.455	3.21%	0.314	690.000	11.455	3.60%
2	M14274	i=150nm (GeH_4-2.4)	04/08/2019	120	0	30	150	-0.003	0.737	-0.003	0.560	-118.620	9.535	5093.658	0.648	5.67%	0.478	736.667	12.462	5.95%
3	M14278	i=175nm (GeH_4-2.4)	04/08/2019	140	0	35	175	-0.003	0.719	-0.003	0.520	-138.000	12.141	2564.103	0.576	5.71%	0.414	719.000	12.9983	5.38%
4	M14279	i=200nm (GeH_4-2.4)	04/08/2019	160	0	40	200	-0.003	0.706	-0.002	0.520	-114.999	11.129	3883.495	0.604	4.90%	0.426	706.000	13.641	5.81%

Table F.30: The logbook of an extra intrinsic layer thickness change series with a V shaped intrinsic layer (with a wide n/i width) with a GeH_4 flow rate from 0.2 to 2.4 sccm and n/i buffers consisting of 3.2 nm i-a-Si and i-a-SiGe:H.

Grading V3 [120-30nm] with n/i and n/i a-SiGe:H buffer								Solar Cell Parameters												
								Isc:	Voc:	Impp:	Vmpp:	Jsc :	Rs :	Rsh:	Fill factor:	Eff:	Voc x FF	Voc	Jsc :	Corrected Eff:
Sl No.	Dep. No.	Description	Date	n/i [nm]	i-i [nm]	i/p [nm]	Thickness [nm]	[A]	[V]	[A]	[V]	[A/m^2]	[Ωm^2]	[Ωm^2]	[%]	[%]	[-]	[mV]	[mA/cm^2]	[%]
1	M14317	i=135nm (GeH_4-4.3)	09/08/2019	108	0	27	135	-0.003	0.605	-0.002	0.427	-121.345	14.720	2482.230	0.558	4.11%	0.338	605.000	13.941	4.70%
2	M14313	i=150nm (GeH_4-4.3)	09/08/2019	120	0	30	150	-0.003	0.610	-0.002	0.427	-121.463	17.534	544.982	0.435	3.24%	0.266	609.667	13.660	3.62%
3	M14316	i=165nm (GeH_4-4.3)	09/08/2019	132	0	33	165	SHUNTED	SHUNTED	SHUNTED	SHUNTED	SHUNTED	SHUNTED	SHUNTED	SHUNTED	SHUNTED	SHUNTED	SHUNTED	SHUNTED	SHUNTED

F.9. Buffers logbook

Table F.31: The logbook of a buffer series with a V shaped intrinsic layer (with n/i width of 120 nm and i/p width of 30 nm) with a GeH_4 flow rate from 0.2 to 2.4 sccm consisting of different n/i and i/p buffers with i-SiOx, i-a-SiGe:H and i-aSi.

Buffer Series a-SiGe:H (GeH_4 0-2.4 and V3= 120nm [in] - 30nm [ip]								Solar Cell Parameters												
								Isc:	Voc:	Impp:	Vmpp:	Jsc :	Rs :	Rsh:	Fill factor:	Eff:	Voc x FF	Voc	Jsc :	Corrected Eff:
Sl No.	Dep. No.	Description	Date	n/i buffer [nm]	i/p buffer [nm]	Thickness buffers [nm]	Total Thickness buffers [nm]	[A]	[V]	[A]	[V]	[A/m^2]	[Ωm^2]	[Ωm^2]	[%]	[%]	[-]	[mV]	[mA/cm^2]	[%]
1	M14167	reference new thickness	15/07/2019	-	-			-0.003	0.711	-0.002	0.523	-100.930	11.580	4825.267	0.613	4.40%	0.436	711.3333	12.000	5.23%
2	M14163	n/i buffer a-Si	15/07/2019	i-a-Si		5	5	-0.003	0.72	-0.003	0.52	-126.93	13.76	3301.59	0.59	0.054	0.424	716.8	12.8055	5.43%
3	M14164	i/p buffer a-Si	15/07/2019		i-a-Si	5	5	-0.003	0.74	-0.002	0.50	-121.02	17.33	3945.91	0.56	0.050	0.410	735.6	12.2782	5.04%
4	M14165	n/i buffer i-SiOx	15/07/2019	i-SiOx		5	5	-0.003	0.65	-0.002	0.34	-108.97	66.03	1965.04	0.38	0.027	0.246	654.2	11.23805	2.77%
5	M14166	i/p buffer i-SiOx	15/07/2019		i-SiOx	5	5	-0.003	0.66	-0.002	0.42	-117.74	18.75	1443.47	0.48	0.037	0.312	655	9.26055	2.88%
6	M14169	n/i buffer a-SiGe:H	15/07/2019	i-a-SiGe:H		5	5	-0.002	0.72	-0.002	0.54	-87.60	11.19	6449.71	0.63	0.040	0.457	721.2	12.70625	5.81%
7	M14170	i/p buffer a-SiGe:H	15/07/2019		i-a-SiGe:H	5	5	-0.002	0.73	-0.002	0.54	-96.78	11.45	5611.82	0.62	0.044	0.456	730	11.00593	5.01%

Table F.32: The logbook of a buffer series with a V shaped intrinsic layer (with n/i width of 120 nm and i/p width of 30 nm) with a GeH_4 flow rate from 0.2 to 2.4 sccm consisting of different combinations of n/i and i/p buffers with i-a-SiGe:H and i-aSi.

Buffer Series a-SiGe:H (GeH_4 0-2.4 and i=150nm)								Solar Cell Parameters												
								Isc:	Voc:	Impp:	Vmpp:	Jsc :	Rs :	Rsh:	Fill factor:	Eff:	Voc x FF	Voc	Jsc :	Corrected Eff:
Sl No.	Dep. No.	Description	Date	n/i a-SiGe:H [nm]	n/i a-Si [nm]	i/p a-SiGe:H [nm]	Total Thickness buffers [nm]	[A]	[V]	[A]	[V]	[A/m^2]	[Ωm^2]	[Ωm^2]	[%]	[%]	[-]	[mV]	[mA/cm^2]	[%]
1	M14195	Reference 40nm with i/p 5nm a-SiGe	20/07/2019	-	-	5	5	-0.003	0.719	-0.002	0.520	-113.054	12.738	3172.119	0.586	4.77%	0.421	718.500	12.656	5.33%
2	M14196	i/p a-SiGe:H 2nm	20/07/2019	-	-	2	2	-0.003	0.722	-0.003	0.527	-126.656	14.264	3349.665	0.602	5.50%	0.435	722.000	12.413	5.39%
3	M14197	i/p a-SiGe:H 8nm	21/07/2019	-	-	8	8	-0.003	0.729	-0.002	0.507	-112.692	15.821	3705.293	0.563	4.62%	0.410	729.000	12.810	5.26%
4	M14198	i/p a-SiGe:H 11nm	21/07/2019	-	-	11	11	-0.003	0.724	-0.002	0.493	-119.273	14.832	2845.774	0.546	4.71%	0.395	724.333	13.097	5.18%
5	M14199	n/i a-SiGe:H 2nm + (i-p 5nm a-SiGe)	21/07/2019	2	-	5	7	-0.003	0.715	-0.002	0.500	-119.810	16.588	3186.634	0.571	4.90%	0.408	714.667	12.378	5.05%
6	M14200	n/i a-SiGe:H 5nm + (i-p 5nm a-SiGe)	21/07/2019	5	-	5	10	-0.003	0.716	-0.002	0.520	-105.688	17.132	6844.662	0.603	4.56%	0.432	716.333	12.052	5.21%
7	M14201	n/i a-SiGe:H 8nm + (i-p 5nm a-SiGe)	21/07/2019	8	-	5	13	-0.003	0.726	-0.002	0.527	-111.189	12.197	6171.589	0.610	4.92%	0.443	726.333	13.739	6.09%
8	M14202	(n/i a-Si (3nm) + i-n a-SiGe:H+ i/p a-SiGe:H 5nm)	21/07/2019	5	3.2	5	13.2	-0.003	0.737	-0.003	0.540	-119.845	13.586	4690.128	0.616	5.45%	0.454	737.333	12.195	5.54%
9	M14210	n/i a-SiGe:H 2nm	02/08/2019	2	-	-	2	-0.003	0.717	-0.003	0.520	-130.196	18.737	2760.677	0.578	5.39%	0.414	717.333	12.2093	5.06%
10	M14268	n/i a-SiGe:H 8nm	02/08/2019	8	-	-	8	-0.003	0.731	-0.003	0.540	-121.956	11.736	4512.800	0.625	5.57%	0.457	731.333	12.5766	5.75%
11	M14269	n/i a-Si (3nm) + i-n a-SiGe:H (5nm)	02/08/2019	5	3.2	-	8.2	-0.003	0.739	-0.003	0.560	-121.068	10.515	5044.954	0.648	5.80%	0.479	739.000	12.02542	5.75%

Table F.33: The logbook of a p and n layer thickness series with a V shaped intrinsic layer (with n/i width of 120 nm and i/p width of 30 nm) with a GeH_4 flow rate from 0.2 to 2.4 sccm consisting of i/p i-a-SiGe:H buffer.

Different p and n stacks with 5-nm i/p a-SiGe:H								Solar Cell Parameters												
								Isc:	Voc:	Impp:	Vmpp:	Jsc :	Rs :	Rsh:	Fill factor:	Eff:	Voc x FF	Voc	Jsc :	Corrected Eff:
SI No.	Dep. No.	Description	Date	n/i a-SiGe:H [nm]	n/i a-Si [nm]	i/p a-SiGe:H [nm]	Thickness n or p [nm]	[A]	[V]	[A]	[V]	[A/m^2]	[Ωm^2]	[Ωm^2]	[%]	[%]	[-]	[mV]	[mA/cm^2]	[%]
1	M14167	reference new thickness	15/07/2019	-	-		40	-0.003	0.711	-0.002	0.523	-100.930	11.580	4825.267	0.613	4.40%	0.436	711.333	12.000	5.23%
2	M14168	reference old thickness	15/07/2019	-	-		80	-0.002	0.711	-0.002	0.540	-83.881	12.138	5768.111	0.641	3.83%	0.456	711.400	11.698	5.34%
3	M14195	Reference 40nm with i/p 5nm a-SiGe	20/07/2019	-	-	5	40	-0.003	0.719	-0.002	0.520	-113.054	12.738	3172.119	0.586	4.77%	0.421	718.500	12.656	5.33%
4	M14203	reference with middle n layer and i/p 5nm a-SiGe	21/07/2019	-	-	5	60	-0.003	0.698	-0.002	0.453	-120.819	25.376	1716.406	0.481	4.05%	0.336	698.333	11.666	3.92%
5	M14204	p-stack Ashish with i/p 5nm a-SiGe	21/07/2019	-	-	5	18 (instead of 21)	-0.003	0.728	-0.002	0.533	-111.105	11.823	4471.891	0.613	4.95%	0.446	728.333	11.294	5.04%
6	M14205	Optimized H_2 conditions and p-nc-Si Ashish	22/07/2019	-	-	5	18 (instead of 21)	-0.003	0.529	-0.002	0.290	-117.571	21.169	237.720	0.300	1.86%	0.159	528.500	12.071	1.91%

F.10. Grading width logbook

Table F.34: The logbook of an intrinsic layer thickness grading width series with a V shaped intrinsic layer (with a wide n/i width) with a GeH_4 flow rate from 0.2 to 2.4 sccm with 10nm grading width steps.

Grading V3-Serie smaller steps [10nm]								Solar Cell Parameters												
								Isc:	Voc:	Impp:	Vmpp:	Jsc :	Rs :	Rsh:	Fill factor:	Eff:	Voc x FF	Voc	Jsc :	Corrected Eff:
SI No.	Dep. No.	Description	Date	n/i [nm]	i-i [nm]	i/p [nm]	Thickness [nm]	[A]	[V]	[A]	[V]	[A/m^2]	[Ωm^2]	[Ωm^2]	[%]	[%]	[-]	[mV]	[mA/cm^2]	[%]
1	M14114	V3 - 100nm [n-i] and 50nm [i/p]	06/07/2019	100	-	50	150	SHUNTED	SHUNTED	SHUNTED	SHUNTED	SHUNTED	SHUNTED	SHUNTED	SHUNTED	SHUNTED	SHUNTED	SHUNTED	SHUNTED	SHUNTED
2	M14115	V3 - 110nm [n-i] and 40nm [i/p]	06/07/2019	110	-	40	150	SHUNTED	SHUNTED	SHUNTED	SHUNTED	SHUNTED	SHUNTED	SHUNTED	SHUNTED	SHUNTED	SHUNTED	SHUNTED	SHUNTED	SHUNTED
3	M14116	V3 - 120nm [n-i] and 30nm [i-p]	06/07/2019	120	-	30	150	-0.002	0.718	-0.002	0.520	-75.800	13.935	6565.988	0.603	3.28%	0.433	718.000	x	3.28%
4	M14117	V3 - 130nm [n-i] and 20nm [i-p]	06/07/2019	130	-	20	150	SHUNTED	SHUNTED	SHUNTED	SHUNTED	SHUNTED	SHUNTED	SHUNTED	SHUNTED	SHUNTED	SHUNTED	SHUNTED	SHUNTED	SHUNTED
5	M14118	V3 - 90nm [n-i] and 60nm [i-p]	06/07/2019	90	-	60	150	SHUNTED	SHUNTED	SHUNTED	SHUNTED	SHUNTED	SHUNTED	SHUNTED	SHUNTED	SHUNTED	SHUNTED	SHUNTED	SHUNTED	SHUNTED
6	M14119	V3 - 80nm [n-i] and 70nm [i-p]	06/07/2019	80	-	70	150	-0.002	0.718	-0.002	0.480	-76.941	12.692	5654.362	0.548	3.03%	0.393	717.800	x	3.03%

Table F.35: The logbook of an intrinsic layer thickness grading width series with a V shaped intrinsic layer (with a wide n/i width) with a GeH_4 flow rate from 0.2 to 2.4 sccm with 20 nm grading width steps.

Grading V3-Serie bigger steps [20nm]								Solar Cell Parameters												
								Isc:	Voc:	Impp:	Vmpp:	Jsc :	Rs :	Rsh:	Fill factor:	Eff:	Voc x FF	Voc	Jsc :	Corrected Eff:
Sl No.	Dep. No.	Description	Date	n/i [nm]	i-i [nm]	i/p [nm]	Thickness [nm]	[A]	[V]	[A]	[V]	$[A/m^2]$	$[\Omega m^2]$	$[\Omega m^2]$	[%]	[%]	[-]	[mV]	$[mA/cm^2]$	[%]
1	M14129	V3 - 80nm [n-i] and 70nm [i-p]	08/07/2019	80	-	70	150	-0.003	0.725	-0.002	0.493	-114.591	14.127	3024.514	0.540	4.46%	0.391	725.000	12.173	4.76%
2	M14130	V3 - 100nm [n-i] and 50nm [i-p]	09/07/2019	100	-	50	150	-0.003	0.714	-0.002	0.500	-125.784	18.745	2080.363	0.546	4.91%	0.390	714.333	11.630	4.53%
3	M14131	V3 - 120nm [n-i] and 30nm [i-p]	09/07/2019	120	-	30	150	-0.003	0.716	-0.002	0.533	-107.913	14.246	4422.516	0.619	4.79%	0.443	716.333	10.854	4.81%
4	M14132	V3 - 140nm [n-i] and 10nm [i-p]	09/07/2019	140	-	10	150	-0.003	0.711	-0.002	0.540	-118.737	13.499	4027.410	0.629	5.31%	0.447	711.000	11.759	5.26%

Table F.36: The logbook of an intrinsic layer thickness grading width series with a V shaped intrinsic layer (with a wide n/i width) with a GeH_4 flow rate from 0.2 to 2.4 sccm and n/i buffers consisting of 3.2 nm i-a-Si and i-a-SiGe:H with 10nm grading width steps.

Grading V3 - n/i and i-a-SiGe:H buffer steps of 10nm								Solar Cell Parameters												
								Isc:	Voc:	Impp:	Vmpp:	Jsc :	Rs :	Rsh:	Fill factor:	Eff:	Voc x FF	Voc	Jsc :	Corrected Eff:
Sl No.	Dep. No.	Description	Date	n/i [nm]	i-i [nm]	i/p [nm]	Thickness [nm]	[A]	[V]	[A]	[V]	$[A/m^2]$	$[\Omega m^2]$	$[\Omega m^2]$	[%]	[%]	[-]	[mV]	$[mA/cm^2]$	[%]
1	M14270	V3 - 80nm [n-i] and 70nm [i-p]	03/08/2019	80	-	70	150	-0.002	0.725	-0.002	0.531	-100.038	9.257	5295.908	0.608	4.41%	0.441	725.333	12.483	5.50%
2	M14271	V3 - 90nm [n-i] and 60nm [i-p]	03/08/2019	90	-	60	150	-0.003	0.730	-0.002	0.509	-117.877	12.116	3869.367	0.569	4.90%	0.415	730.000	13.061	5.42%
3	M14272	V3 - 100nm [n-i] and 50nm [i-p]	03/08/2019	100	-	50	150	-0.003	0.726	-0.003	0.509	-123.430	13.610	3701.548	0.570	5.11%	0.414	726.333	12.675	5.25%
4	M14273	V3 - 110nm [n-i] and 40nm [i-p]	03/08/2019	110	-	40	150	-0.003	0.725	-0.003	0.516	-129.968	10.676	3674.471	0.592	5.58%	0.429	725.333	12.920	5.54%
5	M14274	V3 - 120nm [n-i] and 30nm [i-p]	03/08/2019	120	-	30	150	-0.003	0.737	-0.003	0.560	-118.620	9.535	5093.658	0.648	5.67%	0.478	736.667	12.462	5.95%
6	M14275	V3 - 130nm [n-i] and 20nm [i-p]	03/08/2019	130	-	20	150	-0.003	0.722	-0.002	0.550	-105.520	8.284	5414.287	0.641	4.88%	0.463	721.500	12.932	5.98%
7	M14276	V3 - 140nm [n-i] and 10nm [i-p]	03/08/2019	140	-	10	150	-0.003	0.729	-0.003	0.560	-127.876	9.058	5103.172	0.654	6.10%	0.477	728.667	12.884	6.14%

Table F.37: The logbook of an intrinsic layer thickness grading width series with a V shaped intrinsic layer (with a wide n/i width) with a GeH_4 flow rate from 0.2 to 2.4 sccm and n/i buffers consisting of 3.2 nm i-a-Si and i-a-SiGe:H with 15 nm grading width steps.

Grading V3 - n/i and i-a-SiGe:H buffer [10nm]								Solar Cell Parameters												
								Isc:	Voc:	Impp:	Vmpp:	Jsc :	Rs :	Rsh:	Fill factor:	Eff:	Voc x FF	Voc	Jsc :	Corrected Eff:
Sl No.	Dep. No.	Description	Date	n/i [nm]	i-i [nm]	i/p [nm]	Thickness [nm]	[A]	[V]	[A]	[V]	$[A/m^2]$	$[\Omega m^2]$	$[\Omega m^2]$	[%]	[%]	[-]	[mV]	$[mA/cm^2]$	[%]
1	M14309	V3 - 120nm [n-i] and 30nm [i-p]	09/08/2019	120	-	30	150	-0.003	0.734	-0.003	0.547	-123.741	11.010	4779.497	0.636	5.78%	0.467	734.333	13.23	6.18%
2	M14310	V3 - 135nm [n-i] and 15nm [i-p]	09/08/2019	135	-	15	150	-0.002	0.728	-0.002	0.567	-102.617	10.047	5582.246	0.666	4.97%	0.485	727.667	12.443	6.03%
3	M14311	V3 - 150nm [n-i] and 0nm [i-p]	09/08/2019	150	-	0	150	-0.002	0.677	-0.002	0.540	-84.206	9.160	4397.537	0.654	3.73%	0.443	677.000	12.441	5.51%

F.11. Tandems a-Si and a-SiGe:H logbook

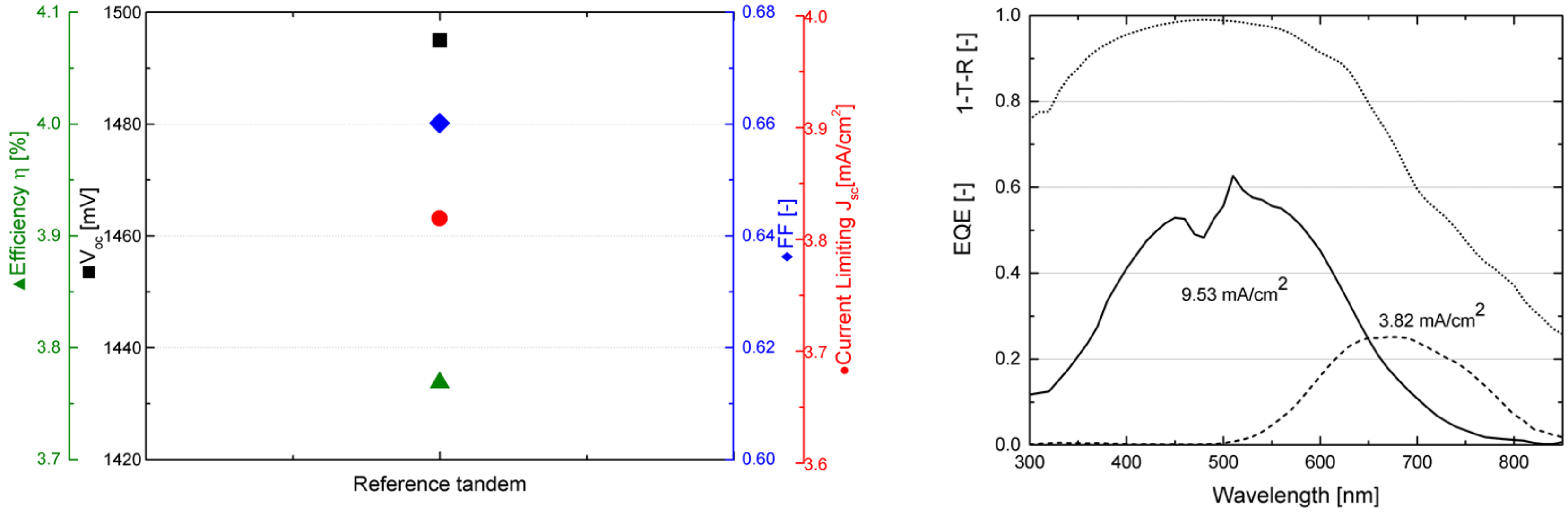

(a)

(b)

Figure F.1: The reference a-SiGe:H best performing bottom cell of 170 nm with a V-shape and the standard 250 nm a-Si top cell on solar cell parameters of tandem solar cells **(a)** and the effect on EQE **(b)**.

Table F.38: The logbook of a tandem series consisting a single junction i-a-SiGe:H cell with a V shaped intrinsic layer (with n/i width of 120 nm and i/p width of 30 nm) consisting of n/i buffers consisting of 3.2 nm i-a-Si and 5 nm i-a-SiGe:H and a single junction i-a-Si cell on Corning Glass - AZO combination.

Tandems-AZO							Solar Cell Parameters													
							Isc:	Voc:	Impp:	Vmpp:	Jsc :	Rs :	Rsh:	Fill factor:	Eff:	Voc x FF	Voc	Jsc Top	Jsc Bottom	Efficiency
SI No.	Dep. No.	Description	Date	GeH_4 [sccm]	n/i a-SiGe[nm]	a-Si High Eg	[A]	[V]	[A]	[V]	[A/m^2]	[Ωm^2]	[Ωm^2]	[-]	[%]	[-]	[mV]	[mA/cm^2]	[mA/cm^2]	[%]
1	M14333	Tandem normal buffer case	10/08/2019	2.4	5	-	-0.001	1.490	-0.001	1.240	-35.771	13.829	9294.025	0.622	3.31%	0.926	1490.000	11.1127	2.457735	2.28%
2	M14334	Tandem without buffers	10/08/2019	2.4	0	-	-0.001	1.497	-0.001	1.240	-37.403	12.088	8412.985	0.605	3.39%	0.906	1497.333	11.50735	2.378365	2.15%
3	M14335	Tandem with 11nm i-na-SiGe:H buffer (104s)	10/08/2019	2.4	11	-	-0.001	1.521	-0.001	1.280	-43.771	14.413	7523.785	0.621	4.14%	0.945	1521.000	10.9339	2.89468	2.73%
4	M14336	Tandem with high germanium (4.3) and buffer	10/08/2019	4.3	5	-	-0.001	1.468	-0.001	1.213	-44.456	12.828	7758.331	0.623	4.07%	0.915	1467.667	8.49836	2.500317	2.29%
5	M14341	Tandem with high germanium (5.3) and buffer	11/08/2019	5.3	5	-	-0.001	1.354	-0.001	1.08	-53.553	12.67	8568.45	0.632	4.58%	0.855	1354.000	11.50109	4.466261	3.82%
6	M14342	Tandem Ge normal + high bandgap aSi	12/08/2019	2.4	5	Yes	-0.001	1.540	-0.001	1.28	-43.208	12.41	12718.19	0.680	4.52%	1.047	1540.333	8.57469	3.96851	4.16%

Table F.39: The logbook of a tandem series consisting a single junction i-a-SiGe:H cell with a V shaped intrinsic layer (with n/i width of 120 nm and i/p width of 30 nm) consisting of n/i buffers consisting of 3.2 nm i-a-Si and 5 nm i-a-SiGe:H and a single junction i-a-Si cell on Asahi glass.

Tandems-Asahi							Solar Cell Parameters													
							Isc:	Voc:	Impp:	Vmpp:	Jsc :	Rs :	Rsh:	Fill factor:	Eff:	Voc x FF	Voc	Jsc Top	Jsc Bottom	Efficiency
SI No.	Dep. No.	Description	Date	GeH_4 [sccm]	n/i a-SiGe[nm]	a-Si High Eg	[A]	[V]	[A]	[V]	[A/m^2]	[Ωm^2]	[Ωm^2]	[-]	[%]	[-]	[mV]	[mA/cm^2]	[mA/cm^2]	[%]
1	M14337	Tandem normal buffer case	10/08/2019	2.4	5	-	-0.001	1.495	-0.001	1.200	-54.054	21.001	13066.076	0.660	5.33%	0.987	1495.000	9.525903	3.818813	3.77%
2	M14338	Tandem without buffers	10/08/2019	2.4	0	-	-0.001	1.487	-0.001	1.213	-52.944	26.277	13187.063	0.662	5.22%	0.985	1487.333	10.9819	4.68868	4.62%
3	M14339	Tandem with 11nm i-na-SiGe:H buffer (104s)	10/08/2019	2.4	11	-	-0.001	1.507	-0.001	1.240	-56.404	18.496	13729.697	0.676	5.74%	1.019	1507.333	11.29475	4.688655	4.78%
4	M14340	Tandem with high germanium (4.3) and buffer	10/08/2019	4.3	5	-	-0.001	1.459	-0.001	1.200	-53.654	19.345	15702.266	0.690	5.40%	1.007	1459.333	11.88495	4.76827	4.80%
5	M14343	Tandem with high germanium (5.3) and buffer	11/08/2019	5.3	5	-	-0.002	1.365	-0.002	1.08	-79.622	16.50	11075.27	0.648	0.070	0.885	1365.333	11.48765	6.277525	5.55%
6	M14344	Tandem Ge normal + high bandgap aSi	12/08/2019	2.4	5	Yes	-0.002	1.534	-0.001	1.27	-60.336	14.89	16538.65	0.687	0.064	1.054	1533.667	8.37391	5.815055	6.13%

Table F.40: The logbook of a tandem series consisting a single junction i-a-SiGe:H cell with changing U and V shaped intrinsic layer consisting of n/i buffers consisting of 3.2 nm i-a-Si and 5 nm i-a-SiGe:H and a single junction i-a-Si cell with variation of thickness of both i-a-Si and i-a-SiGe:H on Asahi glass.

Tandems 2-Asahi							Solar Cell Parameters													
							Isc:	Voc:	Impp:	Vmpp:	Jsc :	Rs :	Rsh:	Fill factor:	Eff:	Voc x FF	Voc	Jsc Top	Jsc Bottom	Efficiency
Sl No.	Dep. No.	Description	Date	a-Si [nm]	a-SiGe:H [nm]	I-layer Shape	[A]	[V]	[A]	[V]	[A/m^2]	[Ωm^2]	[Ωm^2]	[-]	[%]	[-]	[mV]	[mA/cm^2]	[mA/cm^2]	[%]
1	M14374	Tandem 1: a-Si 250 and Ge 4.3-170-V shape	16/08/2019	250	170	V-shape	-0.002	1.450	-0.001	1.173	-68.301	15.059	10777.462	0.653	6.46%	0.947	1449.667	9.758225	7.4019	7.01%
2	M14375	Tandem 2: a-Si 250 and Ge 5.3-170-V shape	17/08/2019	250	170	V-shape	-0.002	1.397	-0.001	1.160	-70.352	12.374	18673.383	0.675	6.63%	0.942	1397.000	9.35403	7.4931	7.06%
3	M14376	Tandem 3: a-Si 250 and Ge 5.3-170-V shape+ in buffer 11nm	17/08/2019	250	170	V-shape	-0.002	1.403	-0.001	1.120	-71.741	15.496	10468.698	0.651	6.55%	0.914	1403.333	9.70924	8.1421	7.44%
4	M14377	Tandem 4: a-Si 200 and Ge 5.3-170-V shape	17/08/2019	200	170	V-shape	-0.002	1.395	-0.001	1.160	-60.089	15.544	14536.233	0.687	5.75%	0.958	1395.000	7.932775	7.9668	7.60%
5	M14378	Tandem 5: a-Si 150 and Ge 5.3-170-V shape	17/08/2019	150	170	V-shape	-0.001	1.385	-0.001	1.160	-54.146	16.354	16148.185	0.721	5.41%	0.999	1384.667	5.818886	10.22038	5.81%
6	M14379	Tandem 6: a-Si 150 and Ge 5.3-200-V shape	18/08/2019	150	200	V-shape	-0.002	1.401	-0.001	1.173	-61.663	14.712	13123.672	0.701	6.05%	0.982	1401.000	7.592505	8.38744	7.46%
7	M14380	Tandem 7: a-Si 150 and Ge 5.3-170-U shape	18/08/2019	150	170	U-shape	-0.001	1.345	-0.001	1.120	-55.647	16.996	14584.187	0.697	5.22%	0.938	1345.333	7.131685	8.89696	6.69%
8	M14381	Tandem 8: a-Si 200 and Ge 5.3-170-U shape	18/08/2019	200	170	U-shape	-0.002	1.322	-0.001	1.067	-70.169	18.788	11287.273	0.671	6.22%	0.887	1322.333	7.49441	8.991615	6.64%
9	M14382	Tandem 9: a-Si 250 and Ge 5.3-170-U shape	19/08/2019	250	170	U-shape	-0.002	1.325	-0.001	1.080	-65.051	15.150	10732.130	0.667	5.74%	0.883	1324.667	8.20573	8.825595	7.25%

Table F.41: The logbook of a tandem series consisting a single junction i-a-SiGe:H cell with changing U and V shaped intrinsic layer consisting of n/i buffers consisting of 3.2 nm i-a-Si and 5 nm i-a-SiGe:H and a single junction i-a-Si cell with variation of thickness of both i-a-Si and i-a-SiGe:H on Corning glass - AZO combination.

Tandems 2-AZO							Solar Cell Parameters													
							Isc:	Voc:	Impp:	Vmpp:	Jsc :	Rs :	Rsh:	Fill factor:	Eff:	Voc x FF	Voc	Jsc Top	Jsc Bottom	Efficiency
Sl No.	Dep. No.	Description	Date	a-Si [nm]	a-SiGe:H [nm]	I-layer Shape	[A]	[V]	[A]	[V]	[A/m^2]	[Ωm^2]	[Ωm^2]	[-]	[%]	[-]	[mV]	[mA/cm^2]	[mA/cm^2]	[%]
1	M14383	Tandem 2: a-Si 250 and Ge 5.3-170-V shape	17/08/2019	250	170	V-shape	-0.001	1.385	-0.001	1.120	-51.293	10.253	11266.199	0.660	4.69%	0.914	1384.667			
2	M14384	Tandem 4: a-Si 200 and Ge 5.3-170-V shape	17/08/2019	200	170	V-shape	-0.001	1.387	-0.001	1.120	-57.411	14.964	13538.233	0.674	5.37%	0.935	1387.000			
3	M14385	Tandem 5: a-Si 150 and Ge 5.3-170-V shape	17/08/2019	150	170	V-shape	-0.001	1.389	-0.001	1.200	-39.720	11.643	19129.746	0.731	4.03%	1.015	1388.667			
4	M14386	Tandem 6: a-Si 150 and Ge 5.3-200-V shape	17/08/2019	150	170	V-shape	-0.001	1.390	-0.001	1.140	-53.357	11.714	14386.708	0.681	5.04%	0.946	1390.000			
5	M14387	Tandem 7: a-Si 150 and Ge 5.3-170-U shape	18/08/2019	150	170	U-shape	-0.002	1.310	-0.001	1.000	-58.032	17.128	9243.563	0.612	4.65%	0.802	1309.500			
6	M14388	Tandem 8: a-Si 200 and Ge 5.3-170-U shape	18/08/2019	200	200	U-shape	-0.002	1.301	-0.001	0.960	-70.734	18.330	8854.336	0.611	5.63%	0.795	1301.000			
7	M14389	Tandem 9: a-Si 250 and Ge 5.3-170-U shape	19/08/2019	250	170	U-shape	-0.002	1.321	-0.002	1.000	-78.732	16.511	8716.678	0.617	6.42%	0.815	1321.000			